DEPARTMENT OF PHYSICS
UNIVERSITY OF JYVÄSKYLÄ
RESEARCH REPORT No. 10/2018

JET SHAPE MODIFICATION IN Pb–Pb COLLISIONS AT $\sqrt{s_{\mathrm{NN}}}$ = 2.76 TEV USING TWO-PARTICLE CORRELATIONS

BY

MÁRTON VARGYAS

Academic Dissertation
for the Degree of
Doctor of Philosophy

To be presented, by permission of the
Faculty of Mathematics and Science
of the University of Jyväskylä,
for public examination in Auditorium FYS1
of the University of Jyväskylä
on 30th of November, 2018
at 12 o'clock noon

Jyväskylä, Finland
November 2018

PERSONAL CONTRIBUTION

Vargyas, Márton
Jet shape modification in Pb–Pb collisions at $\sqrt{s_{\mathrm{NN}}}$ = 2.76 TeV using two-particle correlations

Jyväskylä: University of Jyväskylä, 2018, 126 p.
Department of Physics Research Report No. 10/2018

ISSN 0075-465X; 10/2018
ISBN 978-951-39-7609-5 (print)
ISBN 978-951-39-7610-1 (electronic)

Keywords: jet, jet shape, jet shape modification, jet fragmentation, ALICE, two-particle correlations, correlations, pp, Pb–Pb, Time Projection Chamber, TPC, Gas Electron Multiplier, GEM

THESIS POINTS

The main contributions of the author are listed below:

1) Quality Assurance (QA) of the Gas Electron Multiplier foils that will be built into the ALICE experiment's Time Projection Chamber detector. Graphical software developed to aid the QA project of these foils. The software is processing and displaying the results of both the long term high-voltage measurement and the optical scanning.
2) The correlation study between the Gas Electron Multiplier foils' hole parameters and their gain.
    a) Data processing of the gain measurement
    b) Implementing the correlation framework
3) Analysis of ALICE data: Jet shape modification in pseudorapidity in Pb–Pb collisions at $\sqrt{s_{\mathrm{NN}}}$ = 2.76 TeV
    a) Developed software to extract I_{AA} from ALICE data
    b) Developed analysis software
    c) Systematic error study
    d) Discussion of the results and model comparisons.

Author

Márton Vargyas
Department of Physics
University of Jyväskylä
Finland

Supervisors

Prof. Jan Rak
Department of Physics
University of Jyväskylä
Finland

Dr. Sami Räsänen
Department of Physics
University of Jyväskylä
Finland

Reviewers

Prof. Anne M. Sickles
Department of Physics
University of Illinois
USA

Dr. Martin Spousta
Institute of Particle and Nuclear Physics
Charles University
Czech Republic

Opponent

Prof. Roy Lacey
Department of Chemistry
Stony Brook University
USA

ACKNOWLEDGEMENTS

First I thank my supervisors, Jan Rak, for supporting me during the period of the doctoral program, and Sami Räsänen, for his frequent guidance. Both the results and the text of this thesis benefited greatly from Sami's contributions. He was also overseeing the practical issues, the time and effort spent on these should not be underrated.

I am thankful to the whole Jyväskylä group, yet I would like to highlight a few people. Beomsu Chang, for his coding tips and the inspiring discussions, Jussi Viinikainen, who was always available for the specific questions, and DongJo Kim, whose experience greatly contributed to the analysis.

I also thank Filip Křížek and Mónika Varga-Kőfaragó for their analysis advices and keen eyes on details.

I am grateful to the TPC Upgrade team, especially to Jens Erik Brücken and Timo Eero Hildén. I note that the GEM-related work of this thesis stands on their shoulders. I also thank Dezső Varga, Gergely Gábor Barnaföldi and the REGARD group. It was a pleasure to work with them all.

I thank Hyeonjoong Kim for his help with the Monte Carlo comparisons.

I thank the reviewers, Anne Sickles and Martin Spousta, who improved the quality of the text, and the opponent, Roy Lacey, for accepting this role.

And I am grateful to my family, for valuing and supporting higher education, and to my wife, who kept our children alive while this manuscript was being prepared.

The work of this thesis was funded from several sources. I acknowledge the support of the Väisalä Foundation, the Helsinki Institute of Physics and the University of Jyväskylä.

ACRONYMS

CERN	European Organization for Nuclear Research
PS	Proton Synchrotron
SPS	Super Proton Synchrotron
LEP	Large Electron-Positron Collider
LHC	Large Hadron Collider
ALICE	A Large Ion Collider Experiment
BNL	Brookhaven National Laboratory
RHIC	Relativistic Heavy Ion Collider
TPC	Time Projection Chamber
ITS	Inner Tracking System
GEM	Gas Electron Multiplier
MWPC	Multi-Wire Proportional Chamber
GUI	Graphical User Interface
PDF	Parton Distribution Function
MC	Monte Carlo
QA	Quality Assurance

CONTENTS

OVERVIEW

This thesis focuses on two separate topics. The first topic concerns the upgrade of the Time Projection Chamber (TPC) detector of the ALICE experiment. The upgrade will take place during the second Long Shutdown (2019-2020). The part of the upgrade I participated in was the replacement of the detector's current readout electronics with Gas Electron Multiplier (GEM) foils. This change would allow for the continuous readout of the data, resulting in a hundredfold increase in the amount of data the ALICE experiment can process, as the TPC is the central tracking detector. I was involved in the Quality Assurance (QA) of these GEM foils. The advanced QA procedure consists of three measurements, a long-term high-voltage measurement, a direct gain measurement and an optical scan. I have developed a graphical software to aid the QA of the optical and the high-voltage part, and that program is used in both advanced QA centers. I also developed software for the gain measurement of the foils, and carried out a correlation study between the GEM foil's optical parameters and its gain [1].

The second topic is the analysis of the ALICE data, the measurement of the jet shape modification as a function of pseudorapidity in $\sqrt{s_{\mathrm{NN}}}$ = 2.76 TeV Pb–Pb and pp collisions. In Pb–Pb collisions, the quark gluon plasma (QGP) is created, while in pp collisions, it provides only weak hints for its existence at very high multiplicity events (see e.g. Ref. [2]). Comparing results from these two collisions thus sheds light on the behavior of the new phase of the strongly interacting matter. I have carried out a two-particle correlation analysis, developed the analysis software, and performed the systematic error analysis. The results are also compared to AMPT simulations, as well as a custom Monte Carlo simulation.

The structure of the thesis is therefore dissected into three distinct parts. In Part I a broad introduction preludes the two main topics, chapter 1 provides the physics background for the ALICE data analysis of Part III, while chapter 2 details the experimental layout that is necessary to appreciate the detector upgrade presented in Part II. Part II starts with the description of the TPC detector in chapter 3, and continues with the introduction of the GEM foils in chapter 4. The QA procedures of the GEMs are presented in chapter 5, which then streams into the correlation study between the GEM's hole diameters and gain in chapter 6. It also covers the establishment of the QA criteria for the foils. Part III starts with a literature overview of the analysis topic in chapter 7, then describes the cuts applied to the data in chapter 8. It then discusses the method of the analysis in chapter 9. Corrections (chapter 10) and the evaluation of the systematic uncertainties (chapter 11) follow, before presenting the results of the jet shape analysis and conclude in chapter 12. The thesis closes with a complete summary.

Part I

Introduction

In this part a general introduction to the two main topics of this thesis is given. In chapter 1 the fundamental theories are introduced upon which the jet shape analysis of Part III stands. The basic concepts of the Quantum Chronodynamics (QCD) (section 1.1), the quark-gluon plasma (QGP) (section 1.3), and jet physics (section 1.4) are described here in more detail to provide the necessary introduction to the complex field of heavy-ion physics. In the last section (section 1.5), the Monte Carlo event generators are reviewed.

In chapter 2, the detailed experimental overview is given that is necessary to appreciate the work carried out for Part II. A broad knowledge of the experiment is also essential for Part III as well, e.g. to understand the tracking which is essential for any analysis. The part starts with reviewing CERN's main activities (section 2.1) and its biggest collider ring, the Large Hadron Collider (LHC) (section 2.2). A short summary of the four experiments of the LHC is given before zooming into CERN's dedicated heavy-ion experiment, ALICE (section 2.3). In this chapter, the main detectors and their operating principles of the ALICE experiment are presented. In the last section (section 2.4) the planned upgrade of the ALICE experiment is discussed.

1 HEAVY-ION PHYSICS

The topic of heavy-ion physics focuses on the strong interaction under extreme energy densities. At this high energy density, not only the inner structure of the proton can be seen [3], but the strongly interacting matter built-up from the quarks and the gluons, undergoes a phase transition. From lattice QCD calculations the QCD phase transition temperature $T_c \approx 160$ MeV was obtained [4, 5, 6], which corresponds to a $\epsilon_c \approx 0.5\,\mathrm{GeV/fm^3}$ energy density.

In any experiment, the initial energy density cannot be measured directly. The most widely used model to estimate it is Björken's calculation [7]

$$\epsilon_{\mathrm{Bjorken}} = \frac{\mathrm{d}E}{\mathrm{d}V} \approx \frac{\mathrm{d}E^{\mathrm{measured}}}{R_A^2 \pi \tau_0 \mathrm{d}y}, \tag{1}$$

where R_A is the radius of the nucleus, and τ_0 is the proper time elapsed since the collision. Current state of the art technology allows us to reach an energy density of tens of $\mathrm{GeV/fm^3}$, for the ALICE experiment, it is estimated to be $\epsilon = 12.3 \pm 1.0\ \mathrm{GeV/fm^3}$ [8], well beyond the critical energy density. Conditions like this existed a few microseconds after the Big Bang and can be re-created in collider experiments and studied in a controlled environment.

It was very interesting to see that the hottest matter ever created did not behave as a gas, but rather as a liquid [9], called the quark-gluon plasma (QGP). Heavy-ion physics is dedicated to the study of this newly created matter. Before going into its details, we must turn our attention to the basics, the fundamental description of the quarks, gluons, and the strong interaction they participate in. There is a long history that led to the development of Quantum Chromodynamics (QCD) as well as the field of heavy-ion physics. The subsequent sections only provide a broad overview of the topics, for a more complete summary one should turn to e.g. Refs. [10, 11].

1.1 QCD and asymptotic freedom

Quantum Chromodynamics (QCD) is a field theory describing the strong interaction experienced by the quarks, and the carriers of the interaction, the gluons. It is a rather clear generalization of the Quantum Electrodynamics (QED). The modern derivation is carried out by exploiting the theory's gauge invariance [12]. According to the gauge principle, one can obtain the interaction terms, in this case the gluon fields, from the Lagrangian of the free quarks by localizing the global symmetry group. By requiring the new Lagrangian to be covariant with respect to the new, extended group of local transformations, additional fields have to be introduced. These naturally introduced fields are the interaction terms [13].

Following the discussion presented in Ref. [12], the Lagrangian of the single free quark (of a given flavor) is

$$\mathcal{L}_{0,f} = \sum_{i=1}^{N_{\text{colors}}} \overline{q_{i,f}}(i\partial\!\!\!/ - m_f)q_{i,f}. \tag{2}$$

The global symmetry, that will be localized, is the rotation in color space for color a

$$U = \exp\left(-i\sum_{a=1}^{8}\epsilon_a\frac{\lambda_a}{2}\right), \tag{3}$$

where the generators of the symmetry group are the Gell-Mann matrices λ

$$[\lambda_a, \lambda_b] = 2if_{abc}\lambda_c. \tag{4}$$

The further derivation is not detailed here, it can be shown, that the QCD Lagrangian for N_f flavors is

$$\mathcal{L}_{\text{QCD}} = -\frac{1}{2}tr(G_{\mu\nu}G^{\mu\nu}) + \sum_{f=1}^{N_f}\overline{q_f}(iD\!\!\!/ - m_f)q_f, \tag{5}$$

where $G_{\mu\nu}$ is the gluon field strength tensor, coming from the commutator of the covariant derivatives

$$[D_\mu, D_\nu] =: ig_sG_{\mu\nu}. \tag{6}$$

Note that $G^{\mu\nu} = G_a^{\mu\nu}\frac{\lambda_a}{2}$. The g_s measures the strength of the interaction between the quarks and the gluons. The coupling constant of the strong interaction is connected to this via $\alpha_s := g_s^2/4\pi$.

An interesting consequence of the theory is the so-called asymptotic freedom, the coupling constant's weakening as the energy gets larger. This allows for a perturbative treatment at the high-energy regime, making possible to calculate observables from the first principles. To understand this unique phenomenon, let us follow the line of thinking of Gross [14], and go via the magnetic screening

properties of the vacuum. Using natural units ($c = 1$) the dielectric constant ϵ and the magnetic permeability μ are related by

$$\epsilon\mu = 1. \tag{7}$$

He argues that from Lenz law it follows that in case of classical matter, $\mu < 1$. From Equation 7 that implies that ϵ must be greater than 1, which is equivalent of an electric screening, a property observed e.g. in the QED vacuum. In QCD, however, the gluons are spin one particles acting as color-magnetic dipoles, and they would align themselves parallel to the applied external field. As a result of that, they would increase the strength of such field, so $\mu > 1$. This results in an effect of antiscreening from gluons, $\epsilon < 1$. On contrary to QED, the color-charge gets amplified at large distances and vanishes at infinitesimal distances. And as the antiscreening from the gluons overcome the screening caused by quarks, this paramagnetic property of the Yang-Mills vacuum explains the asymptotic freedom of the QCD. It also accounts for the (color) confinement of the quarks, i.e. that quarks are confined inside mesons and hadrons. Their separation is not possible, as after a certain distance it will be energetically more favorable to create a quark-antiquark pair from the vacuum, and those newly created particles will bond to the original quark-antiquark pair, setting a confinement scale.

The asymptotic freedom is usually expressed as the strong interaction's coupling constant's (α_s) energy (Q) dependence, the perturbative calculation in leading order (LO) leads to

$$\alpha_s := \frac{g_s^2}{4\pi} \sim \frac{1}{\ln(Q^2/\Lambda_{\mathrm{QCD}}^2)}. \tag{8}$$

The Λ_{QCD} parameter sets the reference scale of QCD above which the coupling is small enough for a perturbative treatment. But even in perturbative calculations, some integrals result in infinities, e.g. the self-energy of the electron. The technique to handle these infinities is called the renormalization. There are many techniques for that, therefore the value of Λ_{QCD} depends on the renormalization scheme. With the broadly used modified minimal subtraction ($\overline{\mathrm{MS}}$) method and for 5 quark flavors it is $\Lambda_{\mathrm{QCD}} = (210 \pm 14)$ MeV [15]. The phenomenon of Equation 8 was measured in various processes, a summary of the measurements as well as the theoretical predictions are plotted together in Figure 1.

Now we arrived to the point where we have a fundamental description of the strong interaction, yet it is difficult to calculate observable phenomena at lower energies (below Λ_{QCD}), and that is partially because of the aforementioned self-interaction of the gluons, and partially because the coupling g_s is strong, and perturbative methods work only in the high-energy limit. In the low end of the energy spectrum, where most nuclear processes take place, effective models have to be used, i.e. one has to give up the fundamental relations and work out a phenomenological model.

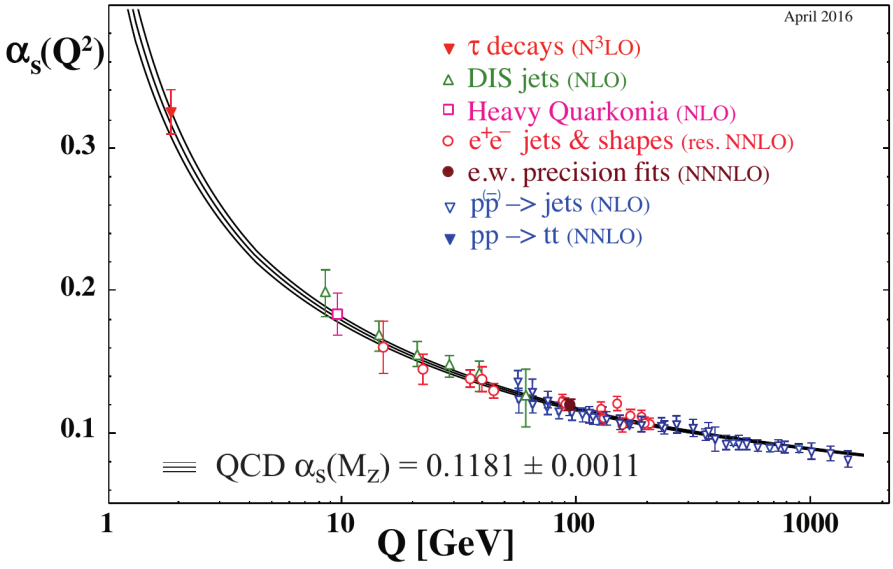

FIGURE 1 Summary of measurements of the running coupling constant of the strong interaction, α_s, as a function of the energy scale Q. Figure from [15].

1.2 The experimental coordinate system

Before describing these measurements, let us briefly mention the coordinate system and the quantities in question. Although ultimately we measure the momentum (p) and the energy (E) of the particles, it is more convenient to formulate observables which fit the detector layout. The momentum p is often decomposed into its longitudinal component (p_z), which goes in the beam direction, and its transverse component (p_T), which is the plane perpendicular to the beam. The azimuthal angle in this transverse plane is denoted by φ, and for the longitudinal direction we use rapidity. It is better than the polar angle θ of the spherical coordinate system, because rapidity is Lorentz-additive. The definition of the rapidity (y) comes directly from E and p_z, yet for unidentified particles, the quantity pseudorapidity (η) can be used, as it does not require knowledge on the mass, only the momentum

$$y = \frac{1}{2}\ln\left(\frac{E + p_z c}{E - p_z c}\right), \qquad \eta = \frac{1}{2}\ln\left(\frac{p + p_z}{p - p_z}\right). \tag{9}$$

One can then decompose the Lorentz-invariant spectrum into

$$E\frac{\mathrm{d}^3N}{\mathrm{d}^3p} = \frac{\mathrm{d}^3N}{p_T \mathrm{d}p_T \mathrm{d}\eta \mathrm{d}\varphi}. \tag{10}$$

The only remaining freedom in this collider's coordinate system is the reference azimuthal angle. Two choices are common, one can either measure it upwards from the horizon assigned by the plane of the collider ring, or one can use the

natural coordinate system of the colliding nuclei, as depicted in Figure 2. In this system, the φ is measured from the axis (x) connecting the nuclei's centers at their closest approach. The x-z plane is also called the Reaction Plane, marked with a green grid in Figure 2. This coordinate system has to be rotated at each event, according to the randomly colliding nuclei.

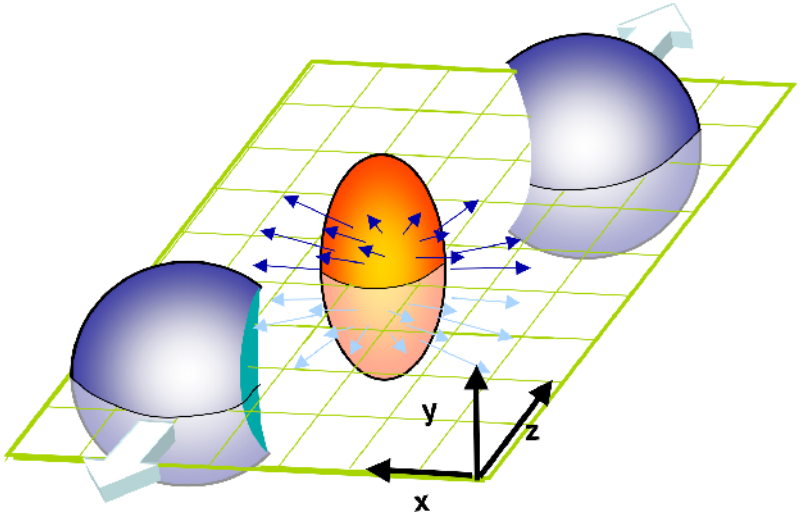

FIGURE 2 Sketch of deformed fireball and elliptic flow generated in non-central heavy-ion collisions [16].

1.3 The Quark-gluon plasma

Figure 3 shows the schematic phase diagram of QCD. In the bottom left corner, there is the vacuum and the nuclear matter, two states that were known for a long time. In the rest of the figure, other, relatively new phases of the strongly interacting matter are shown. At very high chemical potential μ, for example, that is at extremely high baryon density, a superfluid or a color superconducting phase is expected. QCD can thus can provide insights and predictions about astrophysical objects as well, not only for collider physics. The focus of this thesis, however, lies in the exploration of QCD via colliders, we focus on higher temperatures and relatively small baryon densities. The higher temperature or energy density allows for smaller coupling between the quarks and the gluons, which can then move relatively freely as an effect of asymptotic freedom. This results in a new phase of the strongly interacting matter, called the quark-gluon plasma (QGP). A few years after its theoretical foundations [17, 18, 19, 20], Björken showed that high-energy partons traversing it would lose energy [21]. This predicted signature allowed for the experimental search, which started soon after that paper. A variety of observations were carried out by the Brookhaven National Labora-

tory's (BNL) Alternating Gradient Synchrotron (AGS) [22] and by CERN's Super Proton Synchrotron (SPS) [23, 24, 25, 26], showing signs of a new state of matter, which led to a press release by CERN [27, 28]. And after the announcements of BNL's Relativistic Heavy Ion Collider (RHIC), there were hardly any double left about the discovery of the QGP. Four of its major experiments, BRAHMS [29], PHOBOS [30], PHENIX [31] and STAR [32] reported on phenomena in Au+Au collisions that indicated the presence of a new state of matter. Almost all experiments repeated their measurements in d+Au collisions [33, 34, 35, 36], and ruled out initial state and cold nuclear effects. Later, a similar suppression of high transverse momentum particles was observed at CERN LHC (see Ref. [37], and the references therein).

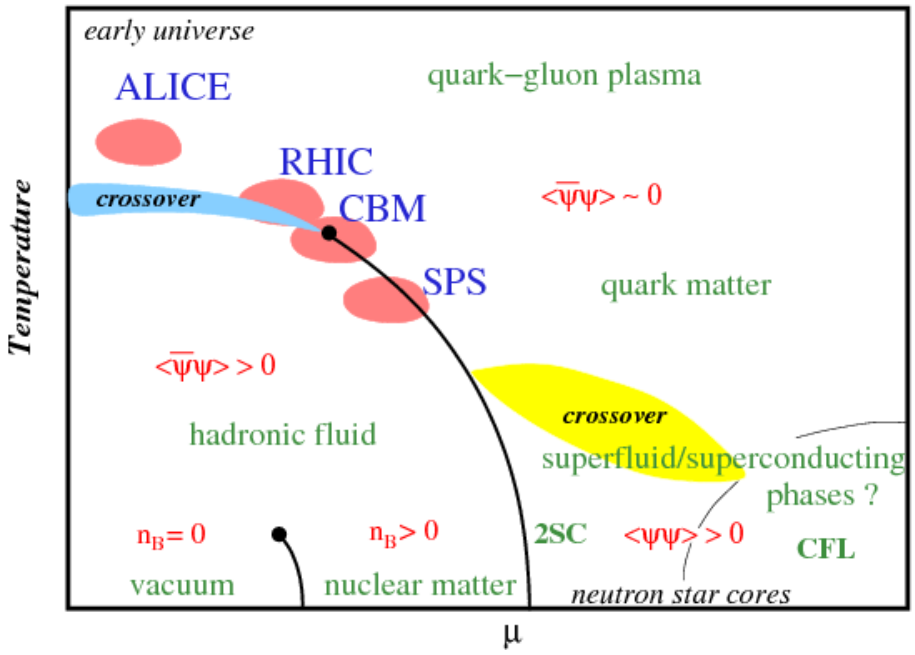

FIGURE 3 Schematic view of the QCD phase diagram. Figure from [38].

To explore the shape of the expanding medium, it proved useful to decompose the azimuthal angle (φ) part of Equation 10 into its Fourier-coefficients [39, 40]. Here φ was measured with respect to the corresponding n^{th} event plane of each event (Ψ_n)

$$E\frac{\mathrm{d}^3N}{\mathrm{d}^3p} = \frac{1}{2\pi}\frac{\mathrm{d}^2}{p_{\mathrm{T}}\mathrm{d}p_{\mathrm{T}}\mathrm{d}\eta}\left(1+2\sum_{n=1}^{\infty} v_n\cos[n(\varphi-\Psi_n)]\right). \tag{11}$$

The second coefficient is the most dominant one, as the strength of the parameters v_n decrease with increasing index n, and since v_1 is suppressed due to momentum conservation [41, 42]. This v_2 term encodes the momentum-space asymmetry it is also called the elliptic flow. The measurement of v_2 was among the first indicators of the QGP [31]. If v_2 is larger than 0, that means the initial ellipticity of

the two overlapping nuclei was conserved and has been turned into ellipticity in momentum-space during the expansion of the medium. This is a characteristic feature of a liquid, in gases this initial asymmetry would vanish during its expansion. Later it was found that in this newly created medium, the QGP, the v_2 scales with the number of constituent quarks. This was related to its partonic degrees of freedom [9]. In Figure 4 this scaling is shown for various identified particles, both hadrons and mesons from two different experiments, PHENIX and STAR. The agreement of the different type of particles is remarkable. In higher LHC energies, however, we observe larger flow [43], and the constituent quark scaling seems to break. It is supposedly because of a denser plasma created in these higher energy collisions, hydrodynamical models with viscous corrections describe the increase [44, 45, 46, 47]. The flow of the QGP is a broadly researched topic, current focus is the study of the higher flow harmonics [48], and the correlation between the flow harmonics [49].

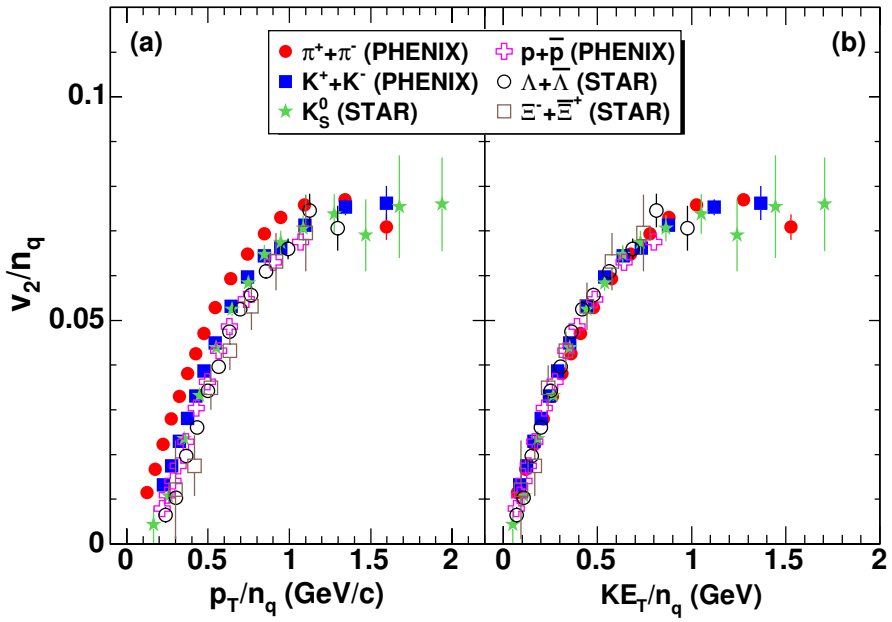

FIGURE 4 Scaling of the flow coefficient v_2 with the number of constituent quarks (n_q). The left panel shows it as a function of the n_q scaled transverse momentum, while the right shows it as a function of the n_q-scaled average kinetic transverse energy KE_T. Figure from [9].

Another key measurement in the discovery of the QGP was the suppression of π^0 production in Au+Au collision as compared to that of pp collisions [31]. Comparing heavy-ion results to pp results is a common technique, because QGP was not observed in proton-proton collisions, so the QGP can be made responsible for the suppression. The quantity called the nuclear modification factor

(Equation 12) is a fine example of this logic

$$R_{\mathrm{AA}}(p_{\mathrm{T}}) = \frac{1}{N_{\mathrm{bc}}} \frac{1/N_{\mathrm{event}}^{\mathrm{AA}} \times \mathrm{d}N_{\mathrm{AA}}/\mathrm{d}p_{\mathrm{T}}}{1/N_{\mathrm{event}}^{\mathrm{pp}} \times \mathrm{d}N_{\mathrm{pp}}/\mathrm{d}p_{\mathrm{T}}}. \tag{12}$$

It is the ratio of the charged particle's p_{T}-spectra from heavy-ion collisions (AA) and proton-proton collisions (pp), normalized by the corresponding number of events. The pp part is scaled up with the number of binary collisions (N_{bc}) of the heavy-ion collisions. This way it measures how the Pb–Pb collisions differ from equal amount of pp collisions. A recent measurement of R_{AA} is shown in Figure 5. A significant suppression can be seen across various experiments and collision energies.

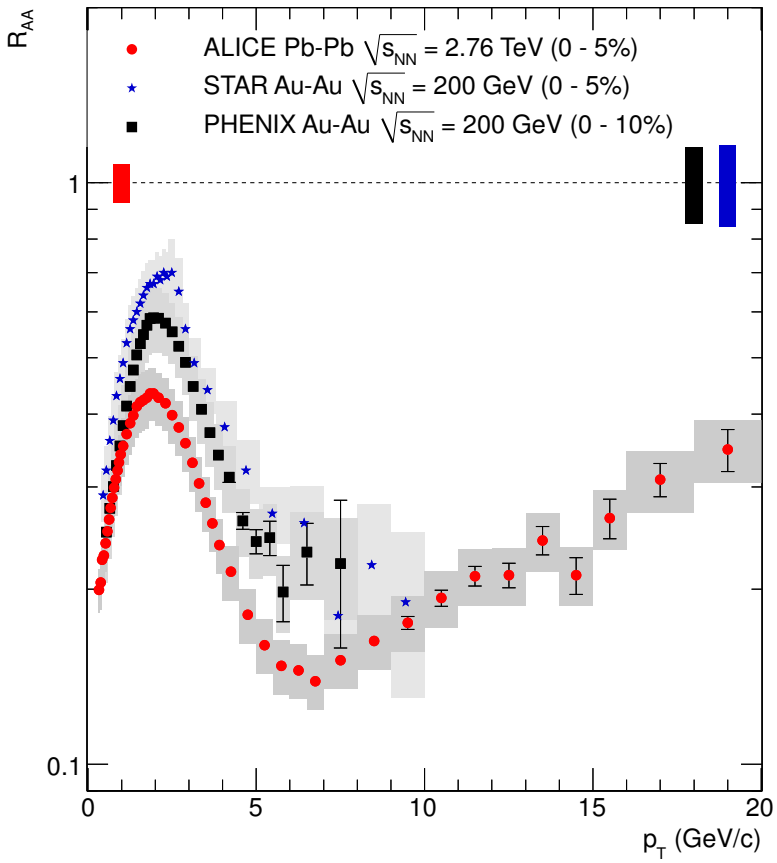

FIGURE 5 Various measurements of the nuclear modification factor R_{AA} for charged particles [50].

1.4 Jet fragmentation

It is difficult to study the evolution of the QGP because of its extremely short lifetime, that is at the order of femtoseconds. We have to then rely on probes

which are generated at the time of the collision and the QGP formation. One of the most used such probe is the jet, a collimated spray of particles. Its seed is a high-p_{T} particle, either a quark and a gluon. This quark or gluon lose energy via producing particles on the way, a phenomenon called the jet fragmentation. The produced particles go approximately in the same direction as the original high-p_{T} particle, because of the energy and momentum conservation, resulting in a conical distribution of particles. This shape is further reinforced by angular ordering, i.e. the phenomenon that each fragment leaves in smaller angle than the previous one [51]. Once the energy of the particles is at the order of Λ_{QCD}, the hadronization occurs.

This chain of thought is formulated mathematically in the QCD factorization theorem [52]. The high-p_{T} hadron production cross-section in hadron-hadron collisions consists of three independent domains

$$\begin{aligned} \mathrm{d}\sigma^{\mathrm{hard}}_{AB\to h} = f_{a/A}(x_1, Q^2) \otimes f_{b/B}(x_2, Q^2) \\ \otimes \mathrm{d}\sigma_{ab\to c}(x_1, x_2, Q^2) \otimes D_{c\to h}(z, Q^2). \end{aligned} \tag{13}$$

The first is the starting point, the parton distribution functions $f_{a/A}$ and $f_{b/B}$. They encode the probability density of finding a parton a with a certain momentum fraction x_1 inside the hadron A at the resolution scale Q^2. The combined HERA and ZEUS measurement of the PDFs [53] is shown in Figure 6. The second term $\sigma_{ab\to c}$ is the parton-parton cross-section. And the last term, $D(z, Q^2)$ is the fragmentation function, which is the probability of a parton to fragment into a hadron with momentum fraction $z = \frac{p^{\mathrm{hadron}}}{p^{\mathrm{parton}}}$.

Contrary to the vacuum propagation, where the energy loss was caused by emitting $q\hat{q}$ pairs or gluons, in the presence of the medium the particles can lose energy via scattering and gluon bremsstrahlung as well. The two possibilities are illustrated in Figure 7. The different energy loss in medium as compared to the vacuum brings about the phenomenon called the jet quenching. Some models, like Q-PYTHIA [54] predict a change of the shape of the fragmentation function in the presence of a medium, therefore it is interesting to compare experiments with and without QGP formation, like in this thesis, comparing Pb–Pb results with that of pp.

There are two ways to find a jet, either by jet reconstruction algorithms, or via two-particle correlations.For the jet reconstruction, one could follow two paths. First is to focus on the geometry and collect all particles around a high-p_{T} particle (i) in a predefined cone radius (R)

$$R^2_{ij} = (\eta_i - \eta_j)^2 + (\varphi_i - \varphi_j)^2 < R^2. \tag{14}$$

The second method, called the sequential recombination, focuses on the momentum differences of the particles. Here we sum up momenta of hadrons which

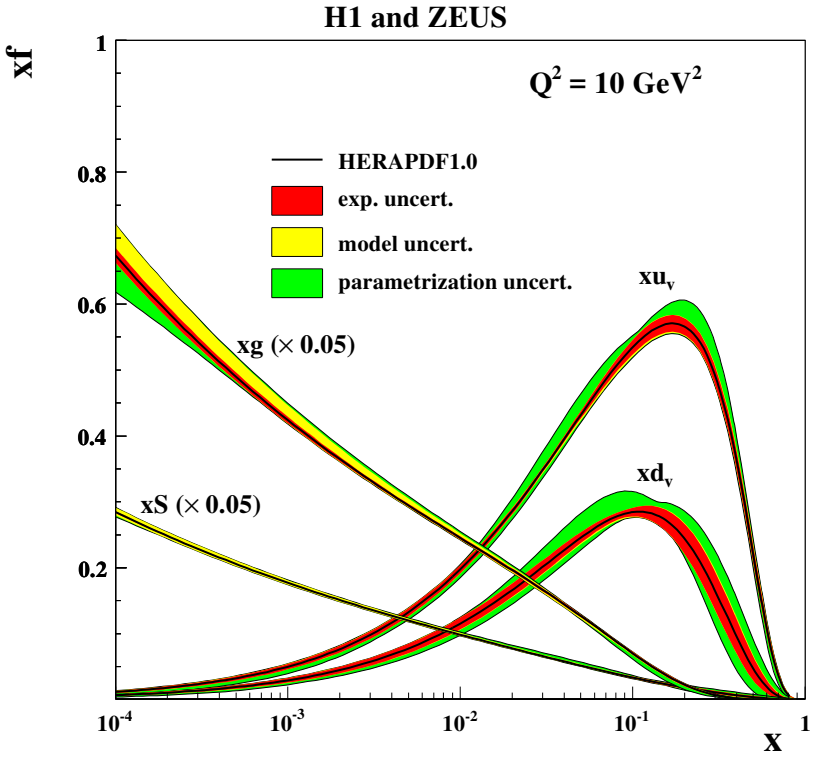

FIGURE 6 The parton distribution functions from combined data of HERA and ZEUS [53].

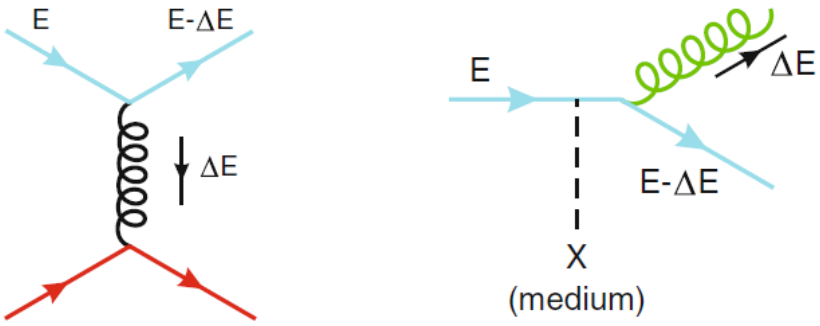

FIGURE 7 Energy loss by scattering (left) or gluon radiation (right).

have the smallest difference in transverse momentum weighted with R_{ij}^2/R^2

$$d_{ij} = \min(p_{\mathrm{T}i}^{2p}, p_{\mathrm{T}j}^{2p}) \frac{R_{ij}^2}{R^2}. \tag{15}$$

The value of p distinguishes between the three most used algorithms: $p = 0$ is called the Cambridge/Aachen algorithm [55], $p = 1$ marks the k_{T} algorithm [56] while $p = -1$ is called the anti-k_{T} algorithm [57].

The two-particle correlation method follows a different logic. Here we do not focus on the jet a priori, but collect all particles, and calculate all pairs' azimuthal angle and pseudorapidity difference ($\Delta\varphi$, $\Delta\eta$) in an event. After doing this for all events, the jet peak emerges naturally at ($\Delta\varphi$, $\Delta\eta$) = (0, 0). This will be further detailed in chapter 9, here we just make the point that this method has clear advantages over the jet reconstruction algorithms in certain regimes and for certain problems. In case of this analysis the two-particle correlation method is preferred as it is applicable at the p_{T}-range of the analysis, and it is not concerned with a definition of a jet, thus more robust at the edges of the jet. This is especially advantageous when studying the softer particles that carry information about the jet-medium interaction.

As discussed in the beginning of the section, the jets can probe the medium and provide information on its properties and evolution. The thesis is concerned with the different jet shapes measured via two-particle correlations in the presence of QGP (Pb–Pb collision) and without (pp collision). Gluon and quark-initiated jets lose energy differently during their traversing of the medium. It is worthwhile to summarize what one would expect from pure quark and pure gluon jets, before studying the role of the medium. Quark jets are expected to be narrower than gluon jets. From the semi-classical approximation [58]

$$\frac{\sigma_g^2}{\sigma_q^2} = \frac{\langle N_g \rangle}{\langle N_q \rangle} = \frac{C_A}{C_F} = \frac{9}{4}, \tag{16}$$

where σ_g is the width of the gluon jet and σ_q is the width of the quark jet. It is clear from the formula that the width difference is related to multiplicity differences, and ultimately the color factors (C_A and C_F). Gluon jets have a larger fluctuation in multiplicity by a factor of $\sigma_g/\sigma_q = \sqrt{C_A/C_F} = 3/2$. The interaction with the medium can introduce further distinction between the two sources of jets, but they will be discussed in chapter 12.

1.5 Monte Carlo event generators

To carry out the theoretical calculation of what one would expect in a heavy-ion or a proton-proton collision, we rely on Monte Carlo event generators and (mostly)

CPU power. The involvement of computers is justified by the extremely complex nature of such calculations. The logic was presented in the previous chapter. First the initial stage, i.e. the stage before the collision, has to be estimated. For that we use the Parton Distribution Functions (PDF). After this, the collision itself can be modeled, and its hard scatterings can be calculated perturbatively from QCD (pQCD). The further evolution of the generated shower, the hadronization, as well as collisions with lower momentum transfer of the order of Λ_{QCD}, however, cannot be calculated perturbatively. For these we need to invoke phenomenological models. Monte Carlo event generators in general [59, 60] go through these calculations, and provide a list of final state particles at the end, which can be compared to the experimental observations. The ones related to the LHC physics are discussed in Ref. [61]. In the following subsections, the MC generators used in this thesis will be review briefly.

1.5.1 PYTHIA

In the work of this thesis, the PYTHIA event generator [62] was used to estimate the efficiency of the pp collisions. PYTHIA is the most popular event generator in high-energy physics, partly because of its continuous long development, dating back to the development of JETSET [63], its predecessor, to 1978.

PYTHIA follows similar steps of calculation as described above. It requires the PDFs and calculates the $2\rightarrow2$ collision, and the following parton shower modeled with $1\rightarrow2$ (and $2\rightarrow3$) splittings, where the virtuality decreases in every step [64]. Initial state radiation is modeled as a shower that propagates back in time [65]. Taking into account the collinear splittings, the probability of these showering processes (both initial state and final state) follow the DGLAP evolution [66, 67, 68]. After the showering, around the energy scale of Λ_{QCD}, the perturbative method cannot work any more, and one must turn to a different approach. This is also the scale when the final state particles, the hadrons are expected to appear. Instead of the simple local parton-hadron duality [69], PYTHIA uses a more sophisticated model for hadronization, namely the Lund string fragmentation model [70]. In the last step of the calculation, the unstable hadrons decay according to their branching ratio.

MC generators in general, and PYTHIA is no exception to that, still have a few parameters that can be tuned. While estimating the efficiency of the pp data, the so-called Perugia-0 tune [71] was used. The setting for this tune was obtained to describe best the data from LEP, Tevatron and SPS, so it is feasible to use it for Run 1 LHC data.

1.5.2 HIJING

For the evaluation of the efficiency of Pb–Pb collisions, the HIJING (Heavy Ion Jet INteraction Generator) [72] event generator was used. It combines perturbative models and low p_{T} multistring phenomenology to provide the best description of the data of high-energy pp, pA and AA collisions. It calculates heavy-ion collisions as a superposition of binary collisions, using Glauber geometry

1.5.3 AMPT

The final observable of the analysis was compared to results obtained from AMPT (A Multi-Phase Transport Model) [73, 74] simulations.

The AMPT is the most complicated Monte Carlo generator described in this thesis. It requires an input from HIJING in the form of excited strings and mini-jets, and calculates their interactions with the Zhang's Parton Cascade model (ZPC) [75]. The hadronization can be set either to the quark coalescence model, or, as in PYTHIA, to the Lund string fragmentation model. An additional step is the (also optional) hadronic rescattering, that is simulated with the ART model [76].

2 EXPERIMENTAL DETAILS

2.1 CERN

CERN is currently the largest accelerator complex in the world. It is located in the suburb of Geneva, on the French-Swiss border. It is a large international collaboration consisting of 22 member countries along with 37 countries with cooperation agreements, and 3 observers. More than 600 institutes and universities use CERN facilities. Its current layout is depicted in a cartoon in Figure 8, but before discussing its experiments, let us review shortly its main discoveries.

Its first accelerator, the Synchrocyclotron (SC) has started to operate[1] already in 1957. A year after its start, it has found the (yet) missing β-decays of the charged pion [78], providing a verification of the V-A coupling theory.
CERN's Proton Synchrotron (PS) had produced of the first antideuteron [79] in 1965, along with the AGS.
CERN was also home of the first Multiwire Proportional Chamber (MWPC), invented by George Charpak in 1968, which revolutionized particle detection [80]. Up to that time, particle identification and momentum measurements were based on analyzing the particles' tracks recorded by bubble and spark chambers, which required a lot of manual work, the "photographed" trajectories were fitted by hand. The signal of the MWPC could be fed into computers, automatizing the analysis and also increasing the detection rate by a factor of thousand.
The mediators of the weak interaction ($W^{\pm}$, and Z^0) were discovered in 1983 in the Super Proton Synchrotron (SPS) [81, 82, 83, 84]. The discovery of direct CP violation was reported by the NA48 experiment [85] in 1999. Researching antimatter is a distinguished program at CERN, in 1995, PS210 experiment created the first antihydrogen atom [86], and recently, in 2011, ALPHA was able to maintain it for 1000 seconds [87]. Another fundamental particle, the Higgs boson, was

[1] https://home.cern/about/accelerators/synchrocyclotron

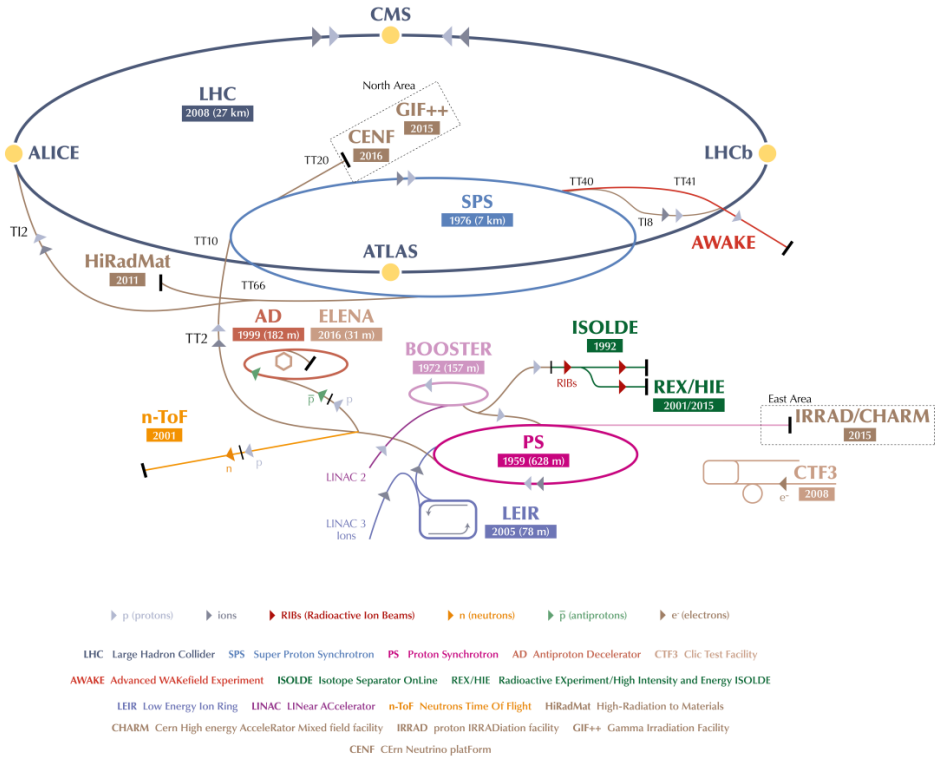

FIGURE 8 The schematic view of the CERN detector complex. The interested reader can find the true scale version of the layout in the Appendix 1. The figure is from [77].

found recently at CERN's Large Hadron Collider (LHC), simultaneously by the CMS [88] and the ATLAS [89] collaborations. The latest discovery was finding the pentaquarks [90] by the LHCb collaboration.

From this short history one can see that CERN has built larger and larger accelerators over the time. A large chain is built this way, and to grasp how complex the acceleration process is, let us follow the path of the proton, from its origin, the hydrogen bottle, to the tunnel of the Large Hadron Collider (heavy-ions follow a similar path). First the hydrogen's electrons are stripped in a duoplasmatron by a strong electromagnetic field. Once they lose their electrons, they can be accelerated with electric fields. All accelerations at CERN are performed by Radio Frequency Cavities. Then the protons are injected into the Linear Accelerator (LINAC), where they reach 50 MeV before being injected into the Proton Synchrotron Booster (PSB), where they get a boost up to 1.4 GeV energy. The Proton Synchrotron (PS) accelerates them further to 25 GeV. In the next step, the Super Proton Synchrotron (SPS), they reach 450 GeV, then they finally can be injected into the LHC, where they reach 3.5 TeV, resulting in a collision energy of $\sqrt{s} = 7$ TeV by the end of Run 1. In case of heavy-ions, the per-nucleon collision energy was $\sqrt{s_{\mathrm{NN}}} = Z/A \times \sqrt{s} = 2.76$ TeV. In current runs, the pp collision energy has doubled to $\sqrt{s} = 14$ TeV, while the heavy-ion per-nucleon collision energy is $\sqrt{s_{\mathrm{NN}}} = 5.02$ TeV.

The described pre-accelerators were all frontiers at their time and they did not descend into a secondary role, as they perform independent experiments when not providing beam for the LHC. The Proton Synchrotron (PS) feeds DIRAC, studying the strong force by the decay of unstable "pionium atoms", and the Antiproton Decelerator (AD), which gives home to AEGIS, ALPHA, ASACUSA, and ATRAP experiments. These all focus on antimatter and exotic matter production. AEGIS studies the gravitation of the antimatter (practically whether it falls up or down in the Earth's gravitational field), ALPHA and ATRAP investigate the symmetry between matter and antimatter by comparing antihydrogen to hydrogen. ASACUSA tests this (so far unbroken) symmetry with antiprotonic helium and antihydrogen. The Proton Synchrotron also provides beam for the CLOUD experiment, which tries to find a link between galactic cosmic rays and cloud formation, for ISOLDE, which studies atomic nuclei and their application in astrophysics, material and life sciences, and for nTOF, the neutron time-of-flight facility that studies neutron-nucleus interactions. The beam of the Super Proton Synchrotron (SPS) is used by COMPASS, NA61/SHINE and NA62. COMPASS studies the complex interaction between quarks and gluons and how the spin arises in protons and in neutrons from their constituents. NA61/SHINE researches the properties of hadrons in collisions of beam particles with fixed targets and NA62 focuses on testing the Standard Model by inspecting measuring rare kaon decays. And there is AWAKE [91], the Advanced Proton Driven Plasma Wakefield

Acceleration Experiment, a proof-of-principle accelerator project in R&D stage. It investigates the possibilities of a new type of acceleration. A proton is shot into a plasma state matter, which then generates a wakefield, that could accelerate a particle if the timing is right. Should this technology succeed, it would result in much smaller and economic accelerators.

Although CERN is known for its accelerators, it hosts other experiments as well. Good examples are CAST, which searches for (the hypothetical) axions from the Sun, and the Alpha Magnetic Spectometer (AMS), which looks for dark matter, antimatter and missing matter from a module on the International Space Station. Now we can start to zoom into the experiment which collected the data of this thesis, the ALICE detector, by starting with the Large Hadron Collider ring.

2.2 The Large Hadron Collider

The Large Hadron Collider (LHC) [92] was built reusing the tunnel of CERN's Large Electron–Positron Collider (LEP). This was an economic solution, but it posed constraints on the LHC design. For example, as protons and heavy-ions do not suffer that much synchrotron radiation as the electrons, the accelerating ring could have had shorter straight sections and longer arcs. Another constraint was imposed by the relatively small cross-section of the tunnel. LEP, being a particle-antiparticle collider needed only one ring for the beams, while the LHC is a particle-particle collider, and needs to have two rings for the counter rotating beams. This led to the implementation of a novel, "two-in-one" superconducting magnet design [93], in which the two rings share the magnetic field, as illustrated in Figure 9. As a result of that, heavy-ion collisions are possible in the old LEP tunnel.

The LHC uses superconducting magnets to keep the particles on track along the ring. Traditional electromagnets are limited to $\sim$2 T, with niobium-titanium coils, however, we can reach a nominal magnetic field of 8.33 Tesla (with 11850 A current) without significant loss of energy. The power consumption of the advanced cryogenic system is not negligible, 150 kW is used to keep the 4.5 K temperature, and an additional 20 kW is distributed around the ring for keeping the helium at 1.9 K. This makes the LHC cooler than the outer space (that has an average temperature of 2.7 K). At this extremely low temperature, the liquid helium enters a superfluid state and exhibits excellent thermal conductivity. For the details on the magnet system of the LHC, see chapter 3 of [92], and for the cryogenics, details can be found in chapter 7. The precision of the LHC is also remarkable. Although only 27 km in circumference, and it is caved into molasse rock and limestone, it can still detect the tides. This is taken into account in the

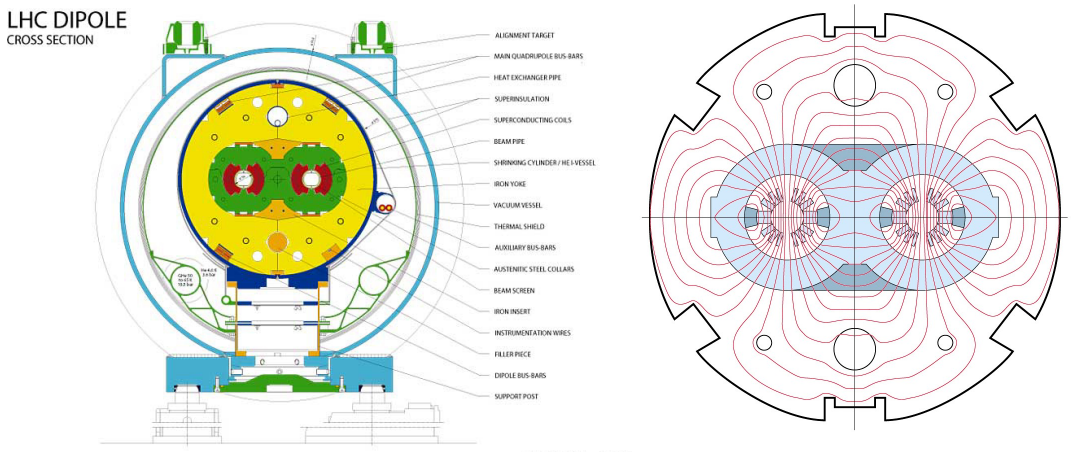

(a) The cross-section of the dipole magnet. Figure from [94].

(b) The computed magnetic flux of the dipole at B_0=10 T. Figure from [95].

FIGURE 9 The computed magnetic flux in the LHC dipole at $B_0 = 10$ T. Figure 9b.

connecting beam segments, and it is corrected for during the calibration of the machine [96][2]. It can also "feel" various geological changes, e.g. deformation of the tunnel shape by the hydrostatic pressure change of the nearby Lake Geneva.

The LHC has seven experiments along its ring, three smaller, the LHCf [98], TOTEM [99] and MoEDAL [100], and four larger, ATLAS [101], ALICE [102], CMS [103] and LHCb [104]. Each small experiment share the cavern with a large one, so it seems natural to introduce them together. Let us go clockwise in the LHC ring (see Figure 10), starting with ATLAS (and LHCf) which lie between the two injection points. I will exclude ALICE, as it will be detailed in a separate section.

ATLAS, "A Toroidal LHC ApparatuS" [101], is 7000-tonne detector, and is 46 m long, 25 m high and 25 m wide (now we defined what we mean under larger experiment). It is focused on particle physics problems such as testing predictions of the Standard Model (SM), and to discover or confirm new theories which go beyond that. It was involved with the discovery of the Higgs boson [89]. Its further physics program is to investigate the CP violation. So far Standard Model's CP violation does not explain the lack of antimatter in the Universe. New theories involving particle production can be studied with the ATLAS detector. It can also perform measurements on the properties of top quark (even study t-tagged jets) [105]. The tremendous energy released in a typical collision at the LHC gave hope that lower mass SUSY particles [106] could be already detected. Instead, ATLAS has ruled out most SUSY models [107, 108] and has set a lower limit on chargino and neutralino masses of a few hundred GeV [109]. The search continues, but possibly SUSY will be discovered beyond LHC energies.

LHCf, the "Large Hadron Collider forward" detector [98] is dedicated to

[2] It was already taken into account with LEP [97].

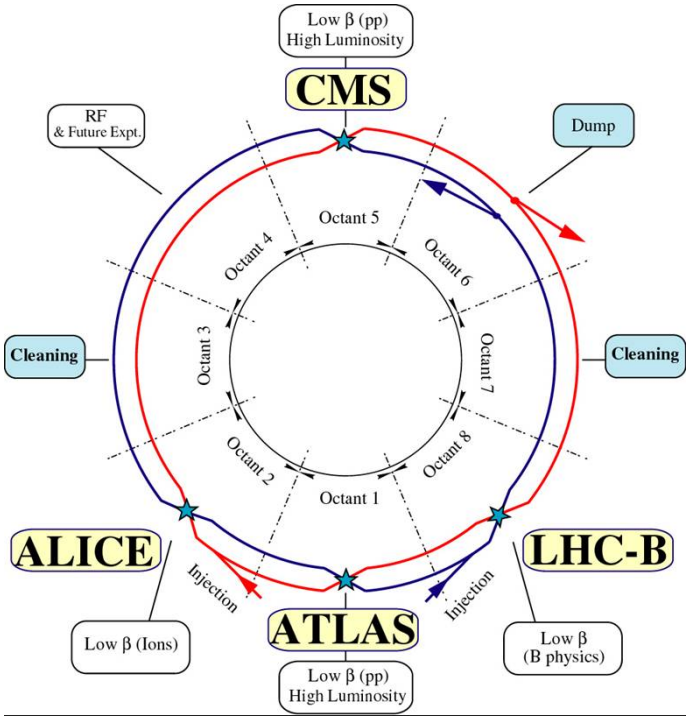

FIGURE 10 Schematic view of the LHC. Figure from [92].

astroparticle physics. It measures particles created very close to the beam line, thus simulating ultra-high-energy cosmic rays. Therefore it is located 140 m away from the ATLAS interaction point (on both sides). Its results are studied together with results of dedicated high-energy cosmic ray measurements, such as the Pierre Auger Observatory in Argentina [110], and the Telescope Array Project in Utah [111].

The next experiment, that was also involved in the Higgs discovery [88], is the CMS, the "Compact Muon Solenoid" detector [103]. It is even heavier than the ATLAS with its 14000-tonne weight, but slightly smaller. Its compact and unique magnetic field, which is generated by a cylindrical coil of superconducting fibers, reaching 4 T (at 18500 A current), is contained by a steel "yoke", which solely weights 12500 tonnes. ATLAS and CMS share most of their physics program, and their different technical solutions along with the different magnet-system design make the combined results more reliable.

The TOTEM, the "TOTal, Elastic and diffractive cross-section Measurement" experiment [99], as suggested by its name, focuses on diffractive physics and elastic cross-section measurements. Like LHCf, it is also close to the beam line, yet it is further away from the interaction point, it is almost half a kilometer around CMS. Some of its detectors can be moved vertically and horizontally in the accelerator vacuum. As it is very close to the beam, it can also complement beam quality measurements [112].

LHCb stands for "Large Hadron Collider beauty" [104], as it is specialized in studying the beauty quark. Its layout is different from the other three main

experiments that surround the interaction point, it is a single arm spectrometer weighting 5600 tonnes. This difference comes directly from the physics it is after, B-hadrons[3] are predominantly produced in the forward cone, so LHCb is concentrated in the forward region as well. This experiment is dedicated to find signatures of new physics by studying the properties of B-mesons.

The MoEDAL, "MOnopole and Exotics Detector At the LHC" experiment [100] was designed to search for magnetic monopoles. Magnetic monopoles are expected to be extremely destructive, so for their detection 10 layers of long-chain molecules in plastic coating are installed. If they are formed in collisions in the LHC, the monopoles would rip through these layers. If this track points back to the interaction point, we have a hint for either a magnetic monopole, or another beyond Standard Model particle, collected under the phrase "highly ionizing Stable Massive Particle" (SMP).

2.3 The ALICE experiment

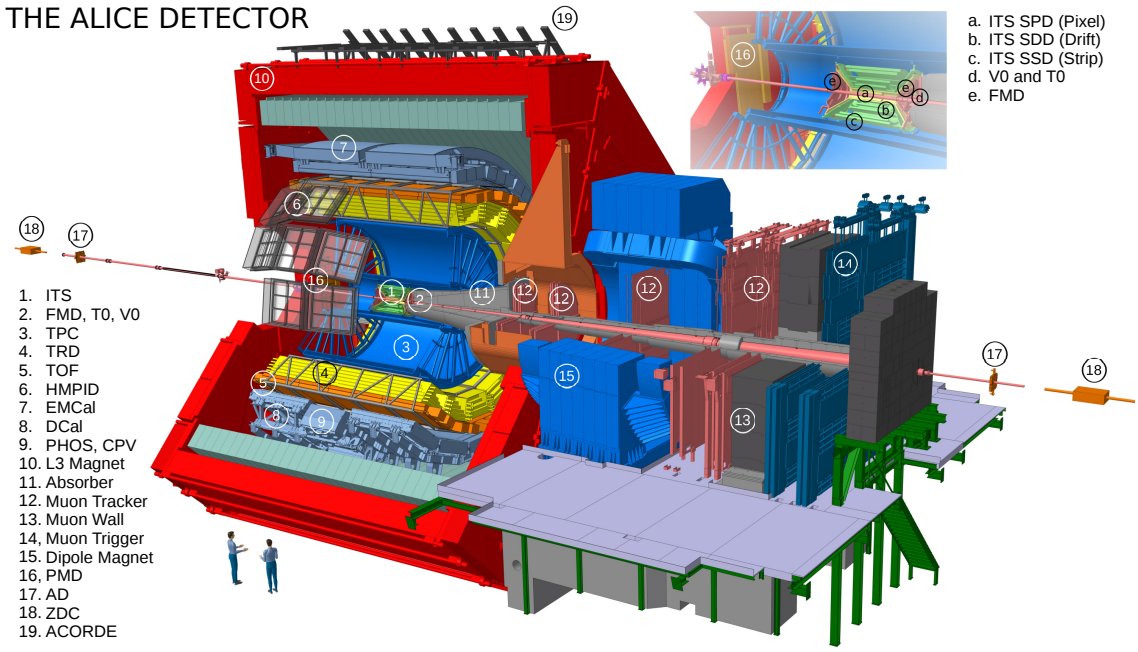

FIGURE 11 The ALICE detector. Figure from [113].

The ALICE, "A Large Ion Collider Experiment" [102] is the only dedicated heavy-ion detector in the LHC ring. It was proposed in 1992 at a meeting "Towards the LHC Experimental Programme". The ALICE collaboration was formed shortly after, and the first Letter of Intent was submitted already in 1993 [114]. Currently the collaboration counts more than 1000 scientists from over 100 physics

[3] These are hadrons which have a b or $\bar{b}$ valence quark.

institutes in 30 countries. The ALICE experiment focuses on the properties of the strongly interacting new state of matter, the quark-gluon plasma. Its place in the QCD phase diagram is marked in Figure 3. As detailed in chapter 1, this new state of matter can be formed at LHC energies, already at Run 1 conditions, that had a center of mass energy of 2.76 TeV. Being the only dedicated heavy-ion detector imposes several constraints on ALICE, one of which comes from the luminosity of the LHC beam. The beam is optimized for LHC's particle physics detectors, which study mostly pp collisions (CMS and ATLAS), and while they are capable of processing heavy-ion runs, the precise low-p_{T} tracking and PID of the ALICE experiment cannot deal with that track density. To still be able to use the same beam as the other experiments, the luminosity levelling technique [115] was introduced, where we shift slightly the two colliding beams to reach a target luminosity, typically few orders of magnitude lower than that of the LHC, depending on the colliding systems.

The layout of the experiment is depicted in Figure 11, it is a 26 m long, 16 m high and 16 m wide, 10,000 tonne detector. It is located at the 2$^{\mathrm{nd}}$ octant of the LHC ring (see Figure 10), 56 m under the French village of Saint-Genis-Pouilly. Similarly to the other three main experiments of the LHC, the ALICE detector was also built around the interaction point of the two counter-circulating beams. Its detectors can be divided according to their roles, and this categorization usually correlates with their location as well. We distinguish trigger detectors, tracking detectors, which lie around the interaction point and going further out we find the electromagnetic calorimeters, which are usually at the outer end as they measure energy deposition by absorbing the particles. There are also the muon spectometers in the forward region.

It is important to determine when the collision takes place to avoid noise from cosmic radiation or beam-gas interactions. This task is performed by the so-called level 0 (L0) trigger, typically 1.2 μs after the collision. Also, sometimes we want to select events according to a more specific information than just the event taking place, in this case we demand a combination of responses from the detectors which have fast trigger capacity (e.g. T0, V0, ZDC, SPD, TOF, TRD, PHOS, EMCal, Muons, ACORDE). Combining the signal from these detectors we can further select events with a higher logic criteria, these are called the L1, and L2 triggers (taking as long as 6.5 μs and 100 μs, respectively). With these we can e.g. select only central collisions, or trigger on jet events. The detectors will be introduced in groups of their aforementioned roles.

The forward and trigger detectors

The forward (L0) trigger detectors are the T0, the V0, the ACORDE, the FMD, the PMD, the ZDC and the ZEN.

The T0 (Time 0) detector is a very important detector with several roles. It acts as an L0 trigger, and provides a wake-up signal to the TRD prior to L0. It discriminates against beam-gas interactions, and generates a start time for the Time of Flight detector. It complements the V0 counters and so can generate minimum bias and multiplicity triggers (semi-central and central). Its timing precision is quite sharp, better than 25 ps. The detector consists of two arrays of Cherenkov counters, the T0-C, located at 72.7 cm from the nominal vertex, and the T0-A, which is 375 cm from the interaction point on the opposite side.

The V0 (Vertex 0) detector also consists of two separate set of scintillator counters, the V0C and the V0A. It is also a multipurpose equipment. It provides the minimum bias trigger signal, and measures the centrality from the multiplicities. If one imposes a cut on the multiplicities, it can act as a centrality trigger.

ACORDE, the ALICE Cosmic Ray Detector is located on the upper surface of the L3 magnet. It provides L0 trigger signal, and it is involved in calibration and alignment procedures for other ALICE detectors. Combined with the TPC, TRD and TOF, it can detect single atmospheric muons and multi-muon events in the knee of the cosmic ray spectrum, that is around a 10^6 GeV particle/m^2/year.

The Forward Multiplicity Detector's (FMD) main purpose is to measure the multiplicity in the pseudorapidity range of -3.4$<\eta<$-1.7 and 1.7$<\eta<$5. The ITS pixel detector (detailed later) covers the missing pseudorapidity range with some redundancy, which allows for both cross-checks between the two subdetectors and for a continuous coverage in η.

The Photon Multiplicity Detector (PMD) measures the multiplicity and spatial distribution of photons in the 2.3$<\eta<$3.7 pseudorapidity range. It serves as an estimator of the transverse energy and the reaction plane, event-by-event.

The Zero-Degree Calorimeter (ZDC) measures the energy of the non-interacting, so called spectator nucleons in the forward direction, at almost 0° relative to the beam direction and 116 m away from the interaction point. With this measurement we can gain information on the number of participating nucleons (number of participants), which are intimately related to the geometry of the collisions:

$$E_{\mathrm{ZDC}}(\mathrm{TeV}) = 2.76/2 \times N_{\mathrm{spectators}} \tag{17}$$

$$N_{\mathrm{participants}} = A - N_{\mathrm{spectators}} \tag{18}$$

assuming 2.76/2 TeV energy per nucleon. In reality, however, this simple calculation does not hold, because in most central and most peripheral heavy-ion collisions, the spectators tend to be fragments having a similar charge-to-mass ratio as of the original Pb nucleus, thus these fragments will stay in the beam pipe,

invisible to the ZDC. This energy dependence on the centrality makes it a good centrality estimator, but on the other hand, we still have to be able to separate the most central and most peripheral events. To do so, two electromagnetic calorimeters (ZEM) were installed only 7 m away from the interaction point, also along the beam line. It measures the energy emitted in the forward rapidity $4.8 < \eta < 5.7$ (the energy deposition is dominated by photon detection $\pi^0 \to \gamma\gamma$), and since the measured energy is a monotonic function of the collision centrality, the separation is possible.

Tracking detectors

The tracking detectors measure the momentum of the particles, and they are also crucial for particle identification, and vertex reconstruction. In the ALICE experiment, we have the TPC, the ITS and the TRD to perform these tasks.

The Time Projection Chamber (TPC) will be detailed later, in chapter 3, here it will be treated like the other detectors, only a brief summary of the operation purpose will be given. The TPC is the main tracking detector and the largest of its kind. It covers $|\eta| < 0.9$, and full azimuth angle. It also has a good momentum resolution in a wide p_{T}-range, from 0.1 GeV/c to 100 GeV/c. It is responsible for measuring the momentum of charged particles (with good two-track separation), particle identification and vertex determination.

The Inner Tracking System (ITS) is a pixel detector system and its main goal is to determine the primary vertex (with resolution < 100 μm). It is also responsible for the reconstruction of the secondary vertex (vertices) from the decays of Hyperons, D and B mesons and also for complementing the TPC's tracking at low transverse momentum, below 200 MeV/c as well as for reconstructing particles going through the dead zones of the TPC. It is a detector system, consisting of six layers of silicon detectors. The two innermost layers are made of Silicon Pixel Detectors (SPD), the middle two layers of Silicon Drift Detectors (SDD), while the two outermost layers are made of double sided Silicon Strip Detectors (SSD).

The Transition Radiation Detector (TRD) provides excellent electron identification above 1 GeV/c momenta. Below that, electrons can be identified from their energy loss in the TPC. This detector makes use of the combination of the Transition Radiation, the phenomenon which occurs when particles radiate when the medium in which they traverse changes. It is filled with a suitable gas mixture fine-tuned for a specific energy loss, to reject pions.

Particle Identification

The particle identification (PID) is usually carried out by combination of detectors, but there are two dedicated solely to this purpose, one of which is the Time-

Of-Flight (TOF) detector. It measures the time passed by between a reference time (provided by the T0 detector) and the time the particle hits the detector. This way it measures velocity instead of momentum, thus it can differentiate between the mass of two particles (m_1 and m_2) having the same momentum,

$$\Delta t = L\left(\frac{1}{v_1} - \frac{1}{v_2}\right) \approx \frac{Lc}{2p^2}(m_1^2 - m_2^2), \tag{19}$$

where L is the distance they traverse. With this method the TOF can provide PID below about 2.5 GeV/c for pions and kaons, and up to 4 GeV/c for protons, with a π/K and K/p separation better than 3σ. See Figure 12.

The High Momentum Particle IDentification detector [116] is the other PID detector in the ALICE experiment, it extends the p_{T}-range of the identification provided by the TPC, ITS and TOF, up to 3 GeV/c for π/K, and up to 5 GeV/c for K/p. The operation principle of this Ring Imaging Cherenkov (RICH) counter is to measure the angle of the Cherenkov radiation (θ_C) emitted in a medium with refractive index $n > 1$, called the Cherenkov radiator, and calculate its velocity according to the simple formula

$$\cos\theta_C = \frac{c}{nv}. \tag{20}$$

When this angle is plotted against the measured momentum, it provides excellent PID, as can be seen in Figure 12.

In addition to the TOF and the HMPID, the TPC, and the ITS can also perform PID via measuring the energy loss characteristic to the particles. The energy loss is described by the "Bethe-Block" equation (section 27.2.2 of [117]):

$$-\left\langle\frac{dE}{dx}\right\rangle = Kz^2\frac{Z}{A}\frac{1}{\beta^2}\left[\frac{1}{2}\ln\frac{2m_ec^2\beta^2\gamma^2T_{\max}}{I^2} - \beta^2 - \frac{\delta(\beta\gamma)}{2}\right], \tag{21}$$

which in this form describes the mean rate of energy loss in the region $0.1 < \beta\gamma < 1000$ for intermediate-Z materials with an accuracy of a few percent. In the equation, K is a constant calculated from the electron constants, the classical electron radius (r_e) and the electron mass (m_e), $K = 4\pi N_{\text{Avogadro}} r_e^2 m_e c^2$. The further parameters, Z and A, are the atomic number and the atomic mass of the absorber, respectively. $T_{\max}$ is the maximum energy transfer possible in a single collision, I is the mean excitation energy, while $\delta(\beta\gamma)$ is the density effect correction to ionization energy loss. This equation presents the energy loss as a function of β.

We usually measure p, see the upper panel of Figure 12, where measured $\mathrm{d}E/\mathrm{d}x$ of the ITS and the TPC are shown. Particles with different mass will form distinct groups, and each curve has a minimum which is characteristic to the particles, so they can be identified. The lines on that figure correspond to a fit of a parametrized version of the Bethe-Block formula, which was originally proposed by the ALEPH collaboration [118]

$$f(\beta\gamma) = \frac{P_1}{\beta^{P_4}}\left(P_2 - \beta^{P_4} - \ln\left[P_3 + \frac{1}{(\beta\gamma)^{P_5}}\right]\right), \tag{22}$$

where P_{1-5} are fit parameters. The lower panel of Figure 12 shows a different tactic for PID, measuring β as a function of p as described above for the TOF, and via the Cherenkov angle in the HMPID detector which is again sensitive to the mass.

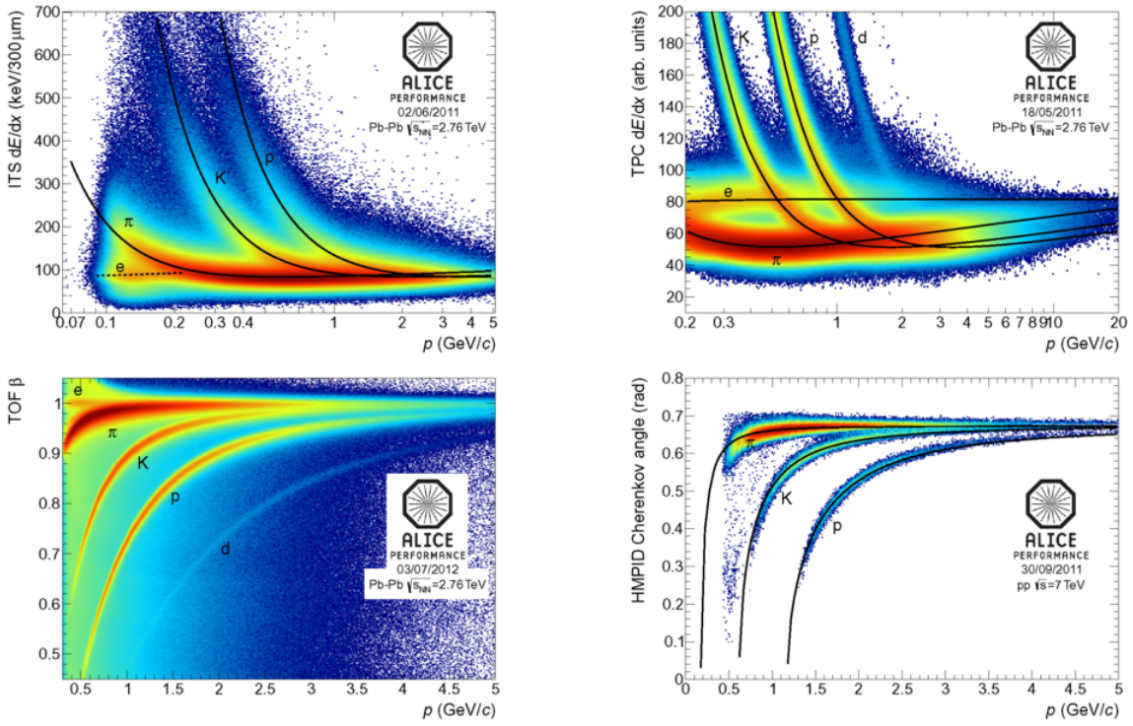

FIGURE 12 The PID performance of the ALICE detector. The figure shows the ITS dE/dx vs. p, the TPC dE/dx vs. p, the TOF β vs. p, and the HMPID Cherenkov angle vs. p. The figure is from [119].

Calorimeters

There are three calorimeters in the ALICE experiment, the PHOS and the EMCal and the DCal.

The PHOton Spectometer (PHOS) is a high granularity electromagnetic calorimeter, designed to work with high multiplicities. It is located on the bottom of the central barrel, covering a limited pseudorapidity range, $-0.12 < \eta < 0.12$, and 100° azimuth angle. Its main goal is to measure the initial phase of the collision from low-p_{T} direct photons, and jet quenching from high-p_{T} π^0- and γ-jet correlations. This is made possible with its good energy and position resolution. Both goals require the clear separation of the direct photons from photons from decays. At high-p_{T}, this is done via tower shape analysis, while at low-p_{T} we can rely on the analysis of their invariant mass.

The ElectroMagnetic CALorimeter (EMCal) is a large Pb-scintillator calorimeter. It is located on top of the ALICE magnet coil, which limits both its size –

its radius from the beam line is ~ 4.5 m –, and its weight, as the L3 magnet has to support it. It covers $|\eta| < 0.7$ and 107° in azimuth, lying on the opposite side of the PHOS. The EMCal increases the electromagnetic calorimeter coverage of the ALICE experiment by almost an order of magnitude, provides fast L0, L1 trigger signals for hard jets, photons and electrons. It also enables full jet reconstruction by measuring not only the charged, but also the neutral components of the jets.

The Di-jet calorimeter arm (DCal) was installed after the first shutdown of the ALICE detector, in 2013-2014 [120], around the PHOS detector. Its main purpose is to extend the acceptance of the EMCal to provide better coverage for di-jets, and allowing for hadron-jet and jet-jet correlation measurements. Thus the DCal and the EMCal are located back-to-back in azimuth. Similarly to the EMCal, it also covers $|\eta| < 0.7$ in pseudorapidity.

Muon detectors

The Muon spectometer is focusing on heavy-flavour physics, by detecting muons in the range -4.0<η<-2.5. It is capable of measuring the heavy-quark vector-mesons (J/Ψ, Ψ', Y, Y′, Y″) and the ϕ meson via their $\mu^+\mu^-$ decay channel. It is shielded from hadrons and photons (see marker 11 in Figure 11), the absorber is followed by the high-granularity tracking system (12), a dipole magnet (15), another filter, but in this case against muons (13), and four planes of trigger chambers (14).

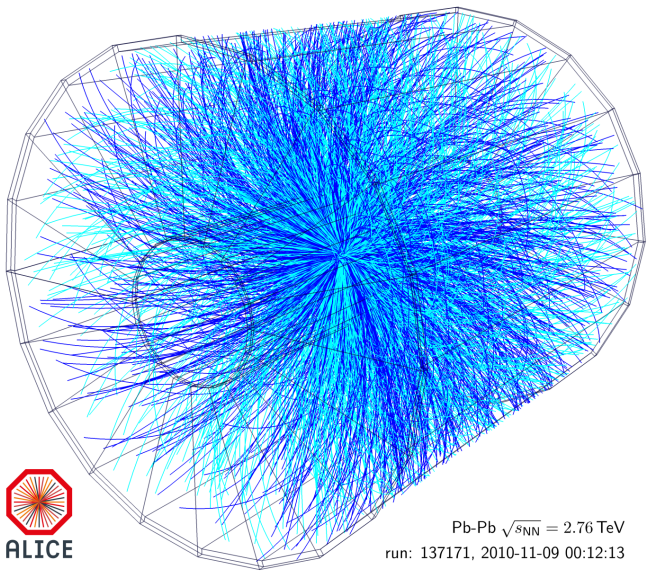

FIGURE 13 One of the first Pb–Pb collisions at the ALICE experiment in 2010. Figure from [121].

Closing remarks

Already in Run 1 (2010), the ALICE experiment faces the demanding task to process thousands of tracks in each event. Figure 13 shows one of the first Pb–Pb event recorded by the ALICE experiment in 2010, one can see that the image is quite busy. The experiment performs well under these conditions, but as the expected readout rate in Run 3 will be 100 times the one of Run 1, several adjustments are needed. To understand what physics we expect to explore with higher luminosity runs, and what inevitable change in its detectors that brings, turn to the next section (2.4). The upgrade of the Time Projection Chamber will be discussed in a separate part (II).

2.4 ALICE Upgrade during Long Shutdown 2

ALICE, along with all major experiments, is upgraded in every few years, either to keep up with the increasing beam energy and luminosity, or to introduce new detectors. Currently, regarding Run 3 after the Long Shutdown 2, the focus is at the luminosity, as the beam energy will not change. The schematic timeline of the LHC luminosity is shown in Figure 14, and the ALICE experiment has to be adjusted to that [122].

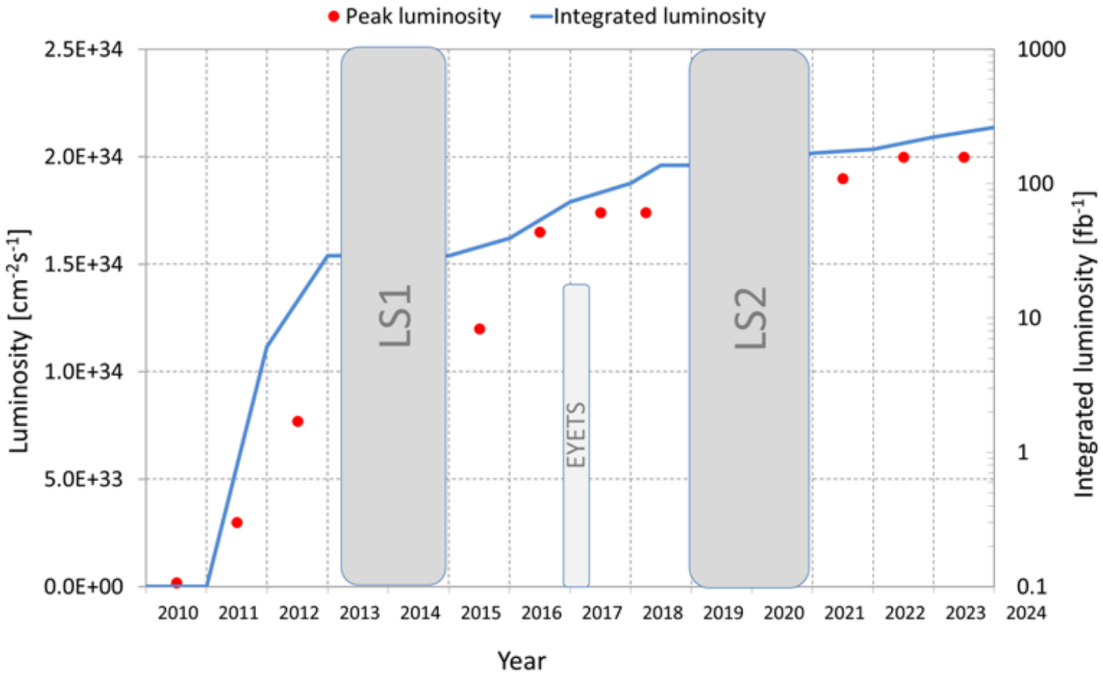

FIGURE 14 The luminosity plan of the LHC, peak luminosity is shown with red dots, the integrated luminosity if with blue lines. Figure from [123].

After Run 1 and the first Long Shutdown (LS 1), the LHC energy was in-

creased to center of mass energy of pp collision of $\sqrt{s}$ = 13–14 TeV and achieved a peak luminosity of $\mathcal{L} = 10^{34}$ cm^{-2}s^{-1}. This was also the time when the DCAL and the TRD detectors, along with PHOS modules, were installed into the ALICE detector. The TPC's gas mixture was changed to Ar-CO_2, which has larger primary ionization improving the momentum resolution.

After Run 2 and the second Long Shutdown (LS 2), the LHC's energy will be unchanged, the luminosity, however, will be higher in Pb–Pb collisions, reaching an integrated luminosity of $\mathcal{L}_{\text{int}} = 1$ nb^{-1}. The ALICE experiment expects an average luminosity of 2.4×10^{27} cm^{-2}s^{-1}, which will result in $\mathcal{L}_{\text{int}} = 10$ nb^{-1} of data collected during Run 3 (2020-2026). In order to achieve this performance, the ALICE experiment will undergo a major upgrade during LS 2. This includes a new, low-material ITS, and its extension to forward rapidity (MFT). The Muon Spectrometer will have vertexing capabilities, and of course the TPC's readout electronics and gating grid technology will be replaced. Part II and the following chapters detail the necessary changes that will be applied to the TPC detector, along with the upgrade's physics program.

In the ALICE Physics Program in Run 3 based on the Technical Design Report [124] along with its addendum [125] the following measurements are planned. The measurement of yields and azimuthal distributions of hadrons with (c, b) heavy-quark thermalization in the QGP, the production of quarkonia at low-p_{T}, to study their possible dissociation and regeneration in the QGP. It intends to measure the low-mass di-electron production to extract information on early temperature and the partonic equation of state, and to characterize the chiral phase transition. Further plans include the measurement of jet correlations, in particular their structure and particle composition, to study the mechanism of partonic energy loss in medium, and the the production of nuclei, anti-nuclei and hyper-nuclei.

Now that the motivation for the upgrade is given, we can turn our attention to the technicalities of the upgrade, focusing on the main tracking detector of the ALICE experiment, the TPC, which is detailed in the following part (II).

Part II

The Time Projection Chamber Upgrade

This part describes the expected upgrade of the ALICE experiment's main tracking detector, the Time Projection Chamber (TPC). In the first chapter of this part (chapter 3), the detector itself is reviewed, with emphasis on its caveats, so that the reader could appreciate the necessity for change in the upcoming higher multiplicity runs. The main development in the detector will be the replacement of the current readout electronics with a new technology, the Gas Electron Multiplier foils. This replacement would allow for a continuous readout of the data, and that would result in a hundredfold increase in the TPC's data-taking capability (and because TPC is the central tracking detector, a similar increase in the capabilities of the ALICE experiment). In the subsequent chapter (chapter 4), the operating principles and technical details of the GEM foils are introduced. chapter 5 details the Quality Assurance (QA) procedure of these foils, and the author's contribution to this project.

In the advanced QA (QA-A) protocol (section 5.2), three additional measurements are performed on top of the basic QA (QA-B) (section 5.1). These are the long-term high-voltage test (subsection 5.2.1), the optical scan (subsection 5.2.2) and the gain measurement (subsection 5.2.3). Once a foil passed all criteria, the most interesting measurement is the gain, which outputs the foil's gain map. Unfortunately, this measurement takes a very long time, and during the QA procedure it was possible to measure only a handful of foils. The optical test, however, was run for all foils. In chapter 6, the correlation between the optical and gain scan is investigated, so that we can predict the foils' gain map only from the optical measurement.

3 THE TIME PROJECTION CHAMBER DETECTOR

Before going into the details of its upgrade, let us review the current parameters and layout of the detector. The Time Projection Chamber (TPC) [124] is a cylindrical gaseous detector. It is the main tracking detector of the ALICE experiment, and also the largest TPC in the world. Its active volume is 90 m^3, it has an inner radius of about 85 cm, an outer radius of about 250 cm, and an overall length along the beam direction of 500 cm. Its acceptance is limited to mid-rapidity, $|\eta|$<0.9, but covers the full azimuth $\phi = 2\pi$, except for the dead zones at the boundaries of the 18 TPC sectors. The detector itself is sketched in Figure 15.

It is filled with a Ne-CO_2-N_2 (85.7-9.5-4.8) gas mixture. The charged particles traversing the TPC would ionize this gas. The knocked-out electrons drift towards the end plates of the cylinder, because a drift field of 400 V/cm is applied along the z-direction, between the middle of the detector and the endplates. The electrons at the end plates are collected with position sensitive multi-wire proportional chambers (MWPC), measuring their x and y position, the third coordinate z is calculated from the drift time. Technically, we measure the position in radial coordinates. The MWPCs measure the radial coordinates, the anode wires arranged in the azimuth direction measure the radial coordinate. To measure the azimuth angle, each cathode plane is divided into strips along the radial direction.

At both of the endcaps, there are 72 Readout Chambers (ROC), 18x3 Outer ROCs (abbreviated as OROC) and 18 Inner ROCs (IROC). Figure 16 show the pad-row structure of one ROCs, demonstrating also its tracking in the transverse plane. The third dimension (z) is calculated from the measured drift time (the total drift time being 92 μs). The tracking is not performed by the TPC alone, but with a combination of detectors (for details, see Figure 32 and surrounding text). The most important detectors are the TPC and the Inner Tracking System (ITS) that are aligned with very high precision via cosmic rays and pp collisions. The alignment is better than 100 μm [127]. This combined tracking of the TPC and the

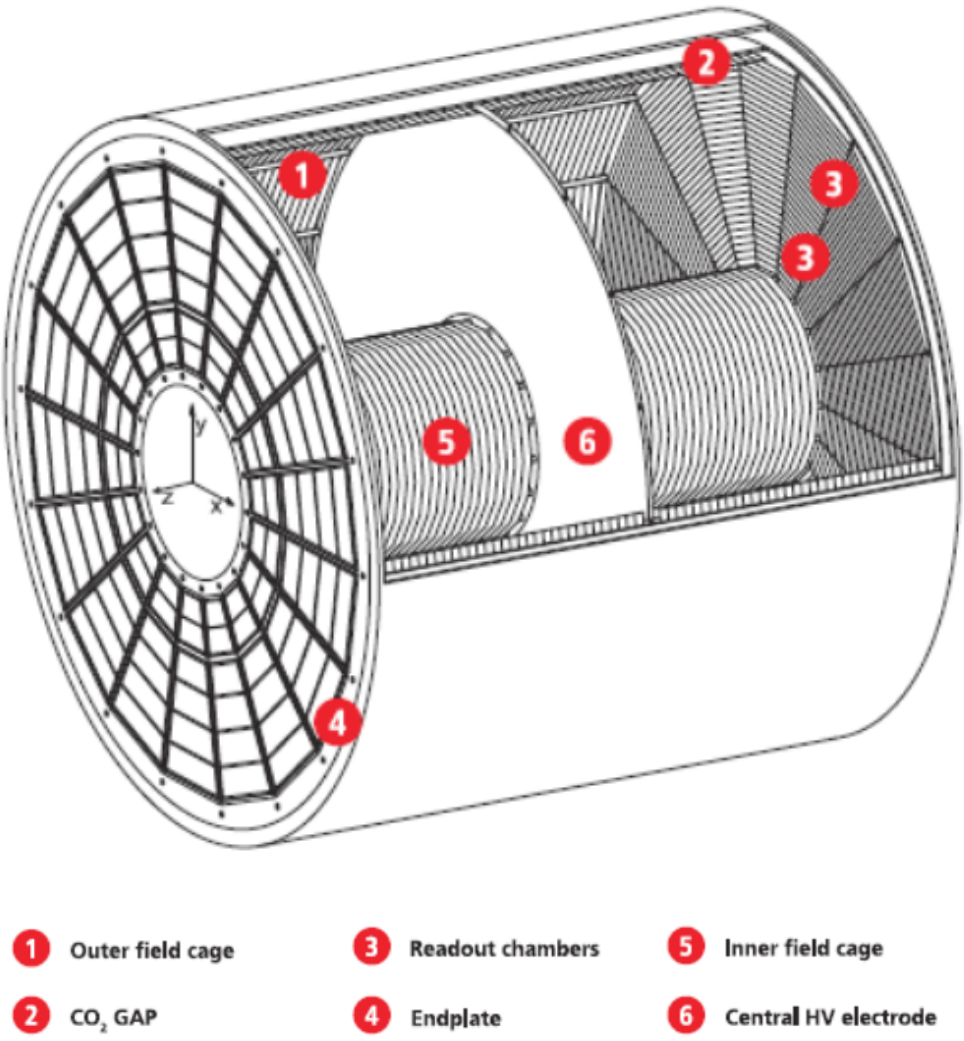

FIGURE 15 The cross section of the TPC. One can see the Outer field cage (1) and Inner field cage (5), between these lays the active area that is be ionized. On the sides are the two Endplates (4) with the multi-wire proportional (MWPC) Readout chambers (3).

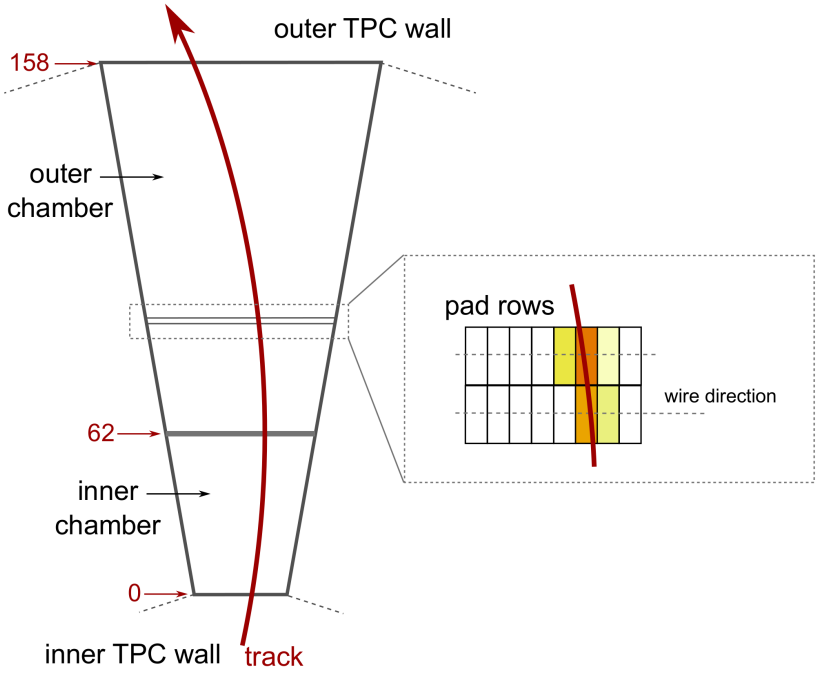

FIGURE 16 The pad-row structure of a ROC, occupying one of the 18 TPC sectors. Figure from [126]

ITS results in a remarkable tracking range for charged particles, the ALICE experiment can reconstruct tracks in the range of 0.05–100 GeV/c with a resolution of 1–10%, depending on the p_{T}. The TPC also performs particle identification via the measurement of $\mathrm{d}E/\mathrm{d}x$ in the fill gas (see Equation 21 and the surrounding text for details), with a resolution of 5% [128]. The performance of the PID was shown in the top right panel of Figure 12.

Currently there is a gating grid technology applied at the readout of the avalanche electrons from the gas volume. Ions would distort the signal, so the gate opens every 100 μs, closes for 300–500 μs, shutting out most of the slower moving ions, but resulting in a relatively large dead-time. The upgrade of the TPC will tackle this disadvantage via replacing the readout with GEM foils so that it would allow for continuous readout, even at the expected 50 kHz event rate, while also shutting out most of the distorting ions. In the next chapter, we turn our attention to the operating principle and quality assurance of these GEM foils.

4 GAS ELECTRON MULTIPLIER FOILS

A Gas Electron Multiplier (GEM) is a type of gaseous ionization detector invented by F. Sauli [129] in 1997. It is a thin polymer foil, with a typical thickness of 50–70 μm, coated with metal on both sides. In the ALICE experiment, we use kapton[1] foils coated with copper. The foils are also pierced quite densely, they have 50-100 holes in the area of a mm^2. The holes have a conical shape which they acquire in a two step chemical etching. First a combination of photolitography and acid etching procedure erodes 30–50 μm diameter holes with cylindrical shapes. In the second step, a chemical etching process is applied on both sides, extending the holes and bringing about the conical shape. The left panel of Figure 17 shows a picture of a section of a GEM, taken with an electron microscope. The cross section of a hole can be seen on the right panel of the same figure.

The working principle of these foils is based on electrodynamics. There is a large potential difference (140-400 V) applied to the two sides of the foil, which results in large field in each hole, acting as both a lens and an amplifier for the electrons [130]. The right panel of Figure 17 illustrates this effect, and one can follow the path of the electrons from their primary ionization and their lensing in the drift field until their readout via a transfer field. The amplification happens inside the holes, where the field is the strongest. As opposed to wire chambers, which typically have one voltage setting, a GEM-based detector requires several independent voltage settings: there is a drift voltage which drives the electrons from the ionization point to the GEM, an amplification voltage, and an extraction voltage that brings electrons from the GEM exit to the readout plane.

One of the main purposes of the introduction of this technology is to reduce the ion backflow [132, 133]. To maximize its insulation, not only one layer of GEM foils will be installed, but instead, a 4 layer stack will be built. The schematic cross section of it is shown in Figure 18. We consider two type of GEMs, the so-called

[1] Kapton is a polyimide film developed by DuPont in the late 1960s, see http://www2.dupont.com/Kapton/en_US/news_events/article20131115.html

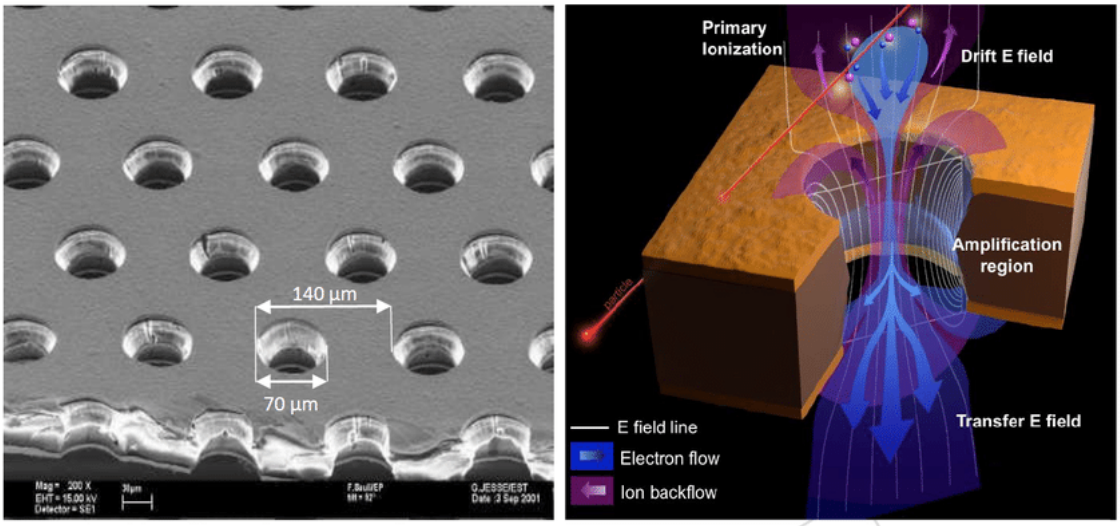

FIGURE 17 Left: Electron Microscope image of a few holes in a GEM foil. Right: Illustration of the path of electrons in a GEM. Figure from [131].

standard pitch (S) GEM, where the pitch size, i.e. the separation of the holes inside a foil is around 140 μm, and a large pitch (LP) GEM, where the holes' spacing is two times larger, 280 μm. The two outer layers, layer 1 and 4 will be built with S GEMs, while the two inner layers, 2 and 3, will use LP GEMs to serve as an extra insulator against the ion backflow. The multi-layer setup also allows for operating the individual GEMs at lower voltages and still have a few order of magnitude increase in the gain, yet without the occurrence of discharges [134].

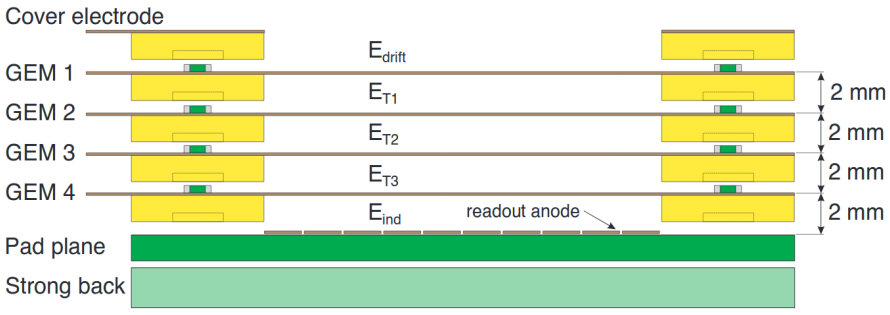

FIGURE 18 Schematic exploded view of the cross section of the GEM stack. Each GEM foil is glued onto a 2 mm thick support frame defining the gap [124].

Recall the Readout Chamber's geometry of the TPC as shown in Figure 16 of chapter 3. Each ROC is divided into an Inner and 3 Outer ROC. Therefore the barcode name of the foils adopted for the labeling starts with this information, I-*, O1-*, O2-*, O3-*. The next part of the name marks the type (G1 and G4 are S-type foils, G2 and G3 label the LP foils), and the last part is a three digit number. So a fifth S-type IROC would have a name "I-G1-005", while an LP OROC 2 will bear e.g. "O2-G2-010". The foils' parameters are listed in Table 1.

The GEMs are produced at CERN, they are cut at CERN's Printed Circuit

Detector	Size (cm^2)	Active area (cm^2)	No. of HV sectors
IROC	54×54	1678.0	18
OROC 1	70×54	1997.3	20
OROC 2	77×54	2240.5	24
OROC 3	91×54	2949.0	30

TABLE 1 Parameters of the GEM foils.

Board workshop. They are then mounted to a special stretch frame, which ensures their flatness during the upcoming tests. After the basic quality control test (QA-B) at CERN performed by the ALICE experiment, the foils are sent to the dedicated advanced QA (QA-A) centers. In the next sections we review the QA procedures in detail.

5 QUALITY ASSURANCE OF THE GEM FOILS

5.1 Basic Quality Assurance of the GEM foils

The basic QA (QA-B) incorporates the most important QA criteria which a GEM should pass. This is performed already at CERN, right after the production. The procedure includes:

- a coarse optical inspection,
- HV cleaning,
- a leakage current measurement,
- a database documentation.

The first step, the optical inspection is by eye, the GEM is laid on to a table with LED back light, to see any major defects, holes, cuts and discolored regions which could indicate problems during the etching process. The position of these defects are then documented for later cross-checking at other institutes.

The second step is the HV cleaning. The foils are kept under very clean conditions, we allow 10^5 particles/m^3 of size 0.1 μm or larger in the clean room[1], and the foils leave this environment only in closed envelopes and boxes, yet, contamination might occur. It is very difficult to clean them after they got dusty. If we clean them by compressed air, for example, the dust particles would most likely end up sealing a hole, which obviously damages the quality of the foil. One way of getting rid of the remaining contamination is a procedure called the HV cleaning. In this process, we apply 600 V (at CERN, 500 V in other institutes) instantly to the GEM, and the induced sparks burn the remaining dust. The location of the sparks are also monitored, if the sparking happens at a given position and not

[1] This corresponds to the ISO 5 classification, where 5 denotes the decimal logarithm of the number of permitted particles per cubic meter of air of size 0.1 μm or larger, according to the ISO 14644-1 standard.

randomly, the foil is sent back for re-cleaning and it will be discarded if it fails this test for the second time. Last resort to clean the foil is to roll it with a special sticky roller.

Attached to the HV cleaning procedure is the leakage current measurement. Here we apply HV to the GEM in steps and measure the leakage current of each sector with a dedicated picoamper-meter (pA-meter) [135]. This measurement is also part of the advanced QA procedure, in that case just performed for a longer time, so it will be detailed later in subsection 5.2.1. Figure 19 shows an example screenshot of the database, where every measurement is documented.

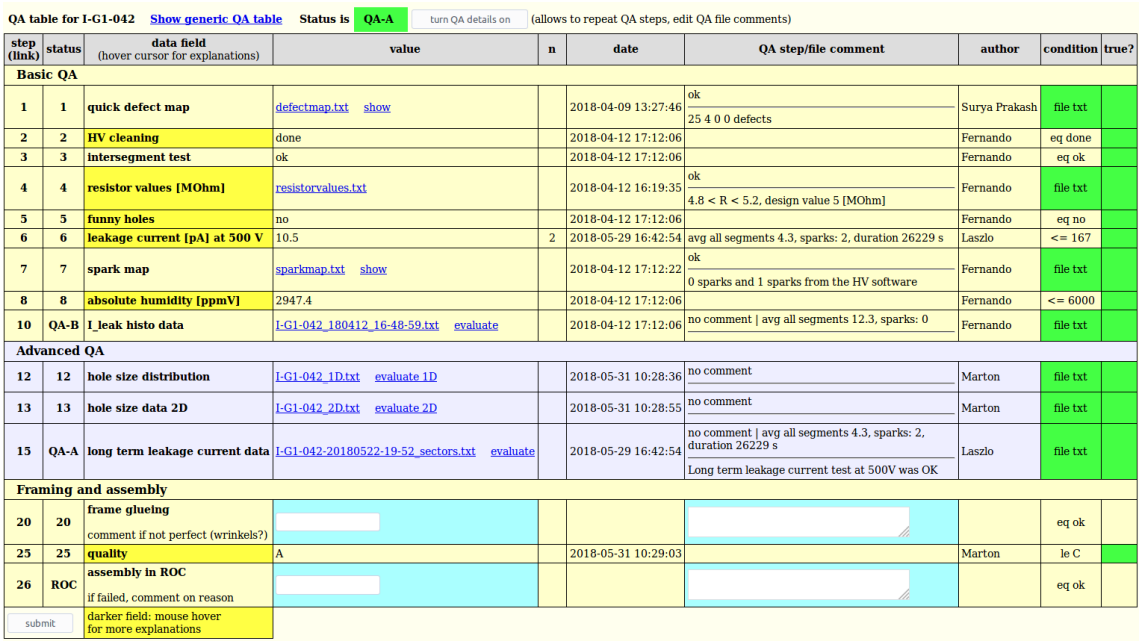

QA table for I-G1-042 Show generic QA table Status is QA-A turn QA details on (allows to repeat QA steps, edit QA file comments)

step (link)	status	data field (hover cursor for explanations)	value	n	date	QA step/file comment	author	condition	true?
Basic QA									
1	1	quick defect map	defectmap.txt show		2018-04-09 13:27:46	ok 25 4 0 0 defects	Surya Prakash	file txt	
2	2	HV cleaning	done		2018-04-12 17:12:06		Fernando	eq done	
3	3	intersegment test	ok		2018-04-12 17:12:06		Fernando	eq ok	
4	4	resistor values [MOhm]	resistorvalues.txt		2018-04-12 16:19:35	ok 4.8 < R < 5.2, design value 5 [MOhm]	Fernando	file txt	
5	5	funny holes	no		2018-04-12 17:12:06		Fernando	eq no	
6	6	leakage current [pA] at 500 V	10.5	2	2018-05-29 16:42:54	avg all segments 4.3, sparks: 2, duration 26229 s	Laszlo	<= 167	
7	7	spark map	sparkmap.txt show		2018-04-12 17:12:22	ok 0 sparks and 1 sparks from the HV software	Fernando	file txt	
8	8	absolute humidity [ppmV]	2947.4		2018-04-12 17:12:06		Fernando	<= 6000	
10	QA-B	I_leak histo data	I-G1-042_180412_16-48-59.txt evaluate		2018-04-12 17:12:06	no comment | avg all segments 12.3, sparks: 0	Fernando	file txt	
Advanced QA									
12	12	hole size distribution	I-G1-042_1D.txt evaluate 1D		2018-05-31 10:28:36	no comment	Marton	file txt	
13	13	hole size data 2D	I-G1-042_2D.txt evaluate 2D		2018-05-31 10:28:55	no comment	Marton	file txt	
15	QA-A	long term leakage current data	I-G1-042-20180522-19-52_sectors.txt evaluate		2018-05-29 16:42:54	no comment | avg all segments 4.3, sparks: 2, duration 26229 s Long term leakage current test at 500V was OK	Laszlo	file txt	
Framing and assembly									
20	20	frame glueing comment if not perfect (wrinkels?)						eq ok	
25	25	quality	A		2018-05-31 10:29:03		Marton	le C	
26	ROC	assembly in ROC if failed, comment on reason						eq ok	
submit		darker field: mouse hover for more explanations							

FIGURE 19 Screenshot of the database, tracking and documenting the Quality Assurance procedure.

5.2 Advanced Quality Assurance of the GEM foils

There are two advanced QA (QA-A) centers, one in the Helsinki Institute of Physics and one in the Wigner Research Centre. They perform the following measurements:

- long-term leakage current measurement
- high resolution optical scanning
- gain uniformity check

and give the final classification of the foils according to a traffic light system. Red means that the foil did not pass the basic selection criteria, so it cannot be used.

Yellow means it might be usable, passed the basic criteria but not the advanced, and finally, green means that it passed all, and the foil is perfect according to the tests performed. Yellow foils are considered usable, could be built into the TPC, but only after green foils are run out.

5.2.1 Long-term HV measurement of the GEM foils

The long-term HV measurement box is shown in Figure 20. Its inner container is adjustable, so it can house GEMs with all sizes of the upgrade. The HV pins are connected to the segments of the GEM foil, and the leakage currents are measured separately for each, by the connected multichannel picoamper-meter (pA-meter) [135]. The pA-meter was designed for the TPC Upgrade project[2]. The pA-meter reads out the data at a 1 kHz rate. The range for the current is $\pm$125 nA, where a 7 pA resolution can be achieved after initial calibration with an external high-precision source. Figure 21 shows an example of the measured leakage current for all sectors (labeled as channels). The accepted leakage current in each segment is 0.16 nA, foils with larger values are discarded. This accepted leakage current defines the range of the x-axis on the left panels of Figure 21 where the distribution of the currents are plotted. The right panels of Figure 21 show the time-dependence of the leakage current. In those figures, one can observe the ramp-up of the HV in the beginning of the dataset as a negative current and the ramp-down at the end (around 21:00) as a large positive current (both are outside of the y-range of the plot). One can also observe the occurrence of two sparks during the measurement as two vertical lines at around 6:00 and 7:00, respectively. Otherwise, the leakage current is constant. Although only one sector sparks at the same time, the HV power supply regulates the voltage to keep the current limit, this is why all channels react. Zooming into that area, it is usually possible to distinguish which channel initiated the drop in the current.

5.2.2 Optical scan of the GEM foils

Many things can go wrong during the etching process, that are not visible by eye, thus they will not be picked up at the coarse optical inspection QA step. It is expected that the hole parameters are connected with the foil's electric properties [136], so it is thus crucial to perform a precise optical measurement during the QA process. Smaller holes, for example, create more intense and focused fields around themselves, which would result in larger amplification of their avalanche electrons, i.e. larger local gain. The relationship between the hole diameters and the gain will be detailed in chapter 6.

In each QA-A laboratories, a scanning robot sitting on a xyz-table is in-

[2] Because of the high demand from the market, the developer has retailed it as an industrial product, see http://www.picologic.hr.

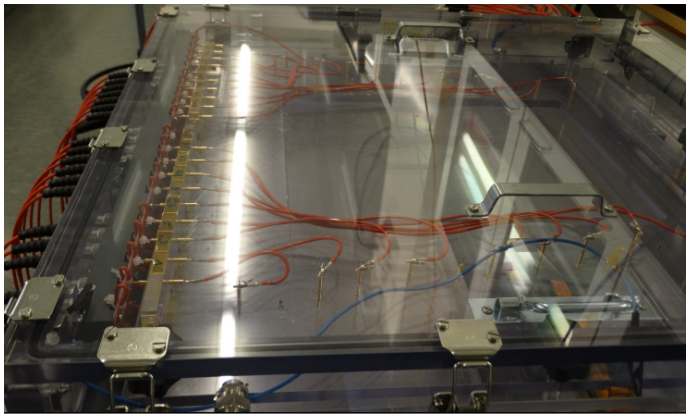

FIGURE 20 Long-term HV measurement equipment at the Helsinki QA center.

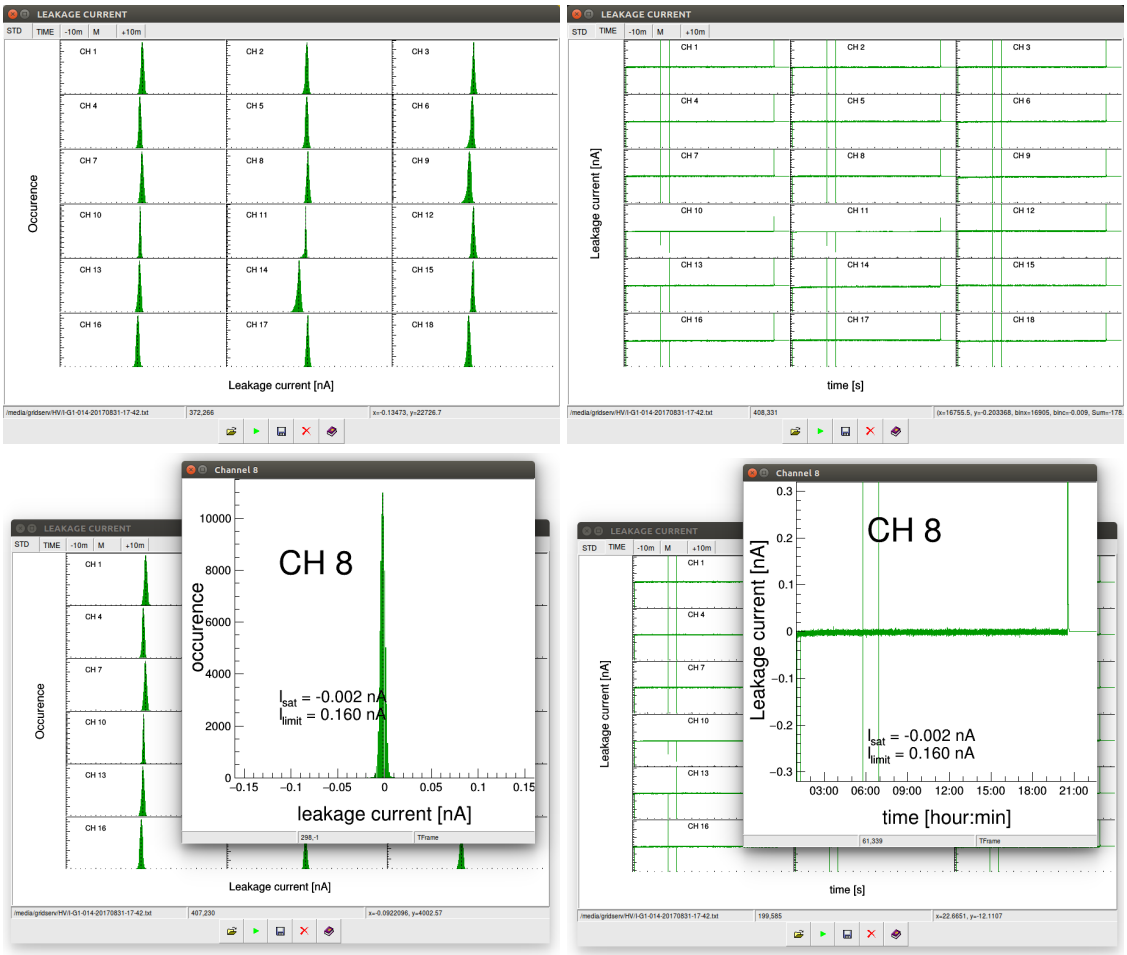

FIGURE 21 Example screenshots from the leakage current window of the TPCQA GUI [1]. In the upper left panel, the distribution of the leakage currents are shown, drawn in the range of acceptance. This gives a clear overview of the measurement, and it is easy to spot the errors (none in this case). The next tab, shown on the upper right panel, shows the leakage current as a function of time. The bottom panels demonstrate another functionality, upon clicking on a figure, a canvas with the corresponding channel will pop up to show the details.

stalled. The coordinate convention is such that x marks the bases of the trapezoid of the GEM foil, y the legs, and z is perpendicular to the plane of the foil. The setup is equipped also with a camera with a telecentric lens, a motor which can move the camera in all three directions, and of course an elaborate analysis software. The setup along with most of the software was developed and built at the Detector Laboratory of the University of Helsinki [137, 138]. The setup with a foil in a stretch frame is shown on the left panel of Figure 22. The right panel of that figure shows an example picture taken with the robot. That image is a superposition of two images, one with foreground-, and another with background illumination. The two are combined into one figure with false coloring. This method is needed because there are three diameters associated with a single hole. Recall the right panel of Figure 17. Here one can observe the hole geometry, the top and the bottom diameters are similar, but can differ slightly due to the separate etching process, and there is a smaller diameter in the middle. The background light brings out clearly these middle holes, while the foreground illumination captures the top (bottom, if the foil is flipped), as less light refracts from the slightly tilted rim.

This setup takes several (combined) images with area about 11.3 mm $\times$ 8.5 mm, corresponding to 2560 by 1920 pixels, respectively, resulting in 2000-3000 individual images of a GEM foil, depending on its type. The images are then fed into a neural network classifier, which extracts the hole parameters by fitting ellipses to the recognized contours. So with this optical scanning method, we can measure every hole in a GEM foil, which is not a trivial task considering that even the smallest foil, the IROC, has about 10 million of them.

Figure 23 shows the distribution of various hole parameters, the diameter, the standard deviation of the diameter in a mm^2 area, the density of the holes, and other maps. These are screenshots from the analysis program, called the TPCQA GUI [1], used at both of the QA-A laboratories to help classifying the foils. The optical scanning thus can also provide a good feedback to the manufacturing people, and helps to ensure the homogeneity and high quality of the GEM foils.

5.2.3 Gain scan of the GEM foils

The gain scanner directly measures the amplification of the GEM foil. The optimal solution would be to perform the gain scan on all foils, but unfortunately it takes up to 2-3 days to measure one foil, so it is impossible to keep up with the production. This scan is always performed after the leakage current measurement and the optical scan. In the beginning of the production, foils which showed interesting features were selected for gain scan (interesting meaning e.g. large rim, not uniform diameter distribution, etc.), later, as the quality of the foils became more stable and the different effects were better understood, foils were

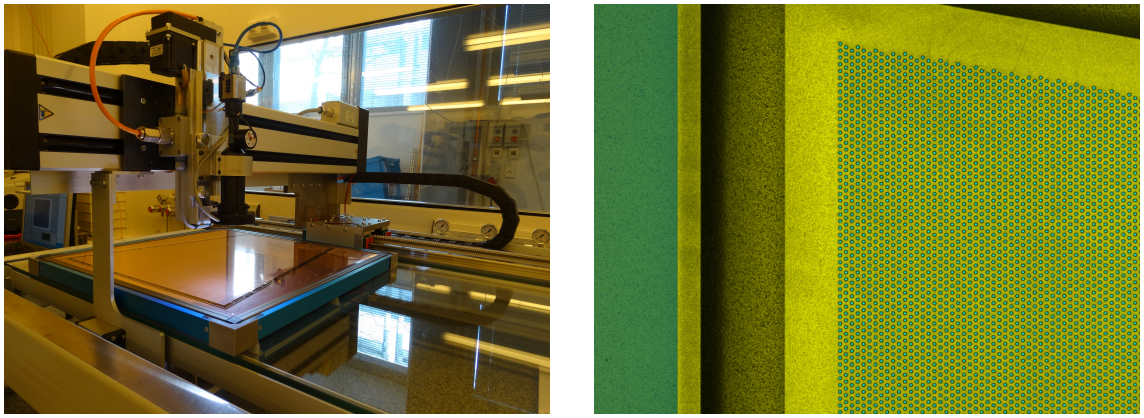

FIGURE 22 Optical measurement equipment in the Helsinki Advanced QA Center (left) and an example image taken with it of the corner of a GEM (right) with false colors.

selected mostly randomly.

The charged particles for the gain measurement are provided by a ^{55}Fe source, that is placed above the foil. It emits X-ray photons with 5.9 keV energy that will convert in the gain scanner's Ar+CO_2 gas mixture to electrons either via photoelectric effect or Compton scattering. These few keV electrons travel a few microns in the gas, ionizing the gas along their path.

Figure 24 shows a photo of the measurement apparatus with an IROC frame. Below the GEM frame, there is a multiwire proportional pad, with perpendicular wires with a resolution of 4mm in x and 3mm in y. (The coordinate convention is similar to that of the optical measurement.) When we apply voltage on the GEM (typically 500 V), it measures the amplification of those wires along with the amplification of the GEM. A reference measurement is also performed when there is no voltage applied to the GEM, in this case we can measure only the amplification of the wires. The HV measurement is then divided with the reference measurement, resulting in the gain map of the GEM. An example of this gain map is shown in Figure 24.

The DAQ collects the events and stores the fired channel numbers in both x and y, along with the corresponding ADC value for each event. The ADC stands for the Analog to Digital Conversion of the analog voltage difference measured in the readout:

$$\text{ADC reading} = \text{Analog voltage} \times \frac{\text{Resolution of the ADC} = 1023}{\text{System voltage} = 5\text{V}}. \tag{23}$$

My analysis software [1] converts the measurement values to an ADC x-y map in two steps: the cluster finding algorithm finds the cases where the fired channels form a continuous sequence, and returns their mean and the corresponding ADC value. Once this is done for all events (typically we collect 5 million events), the ADC distribution in each point is fitted by a Gaussian function to determine the mean ADC of the given point.

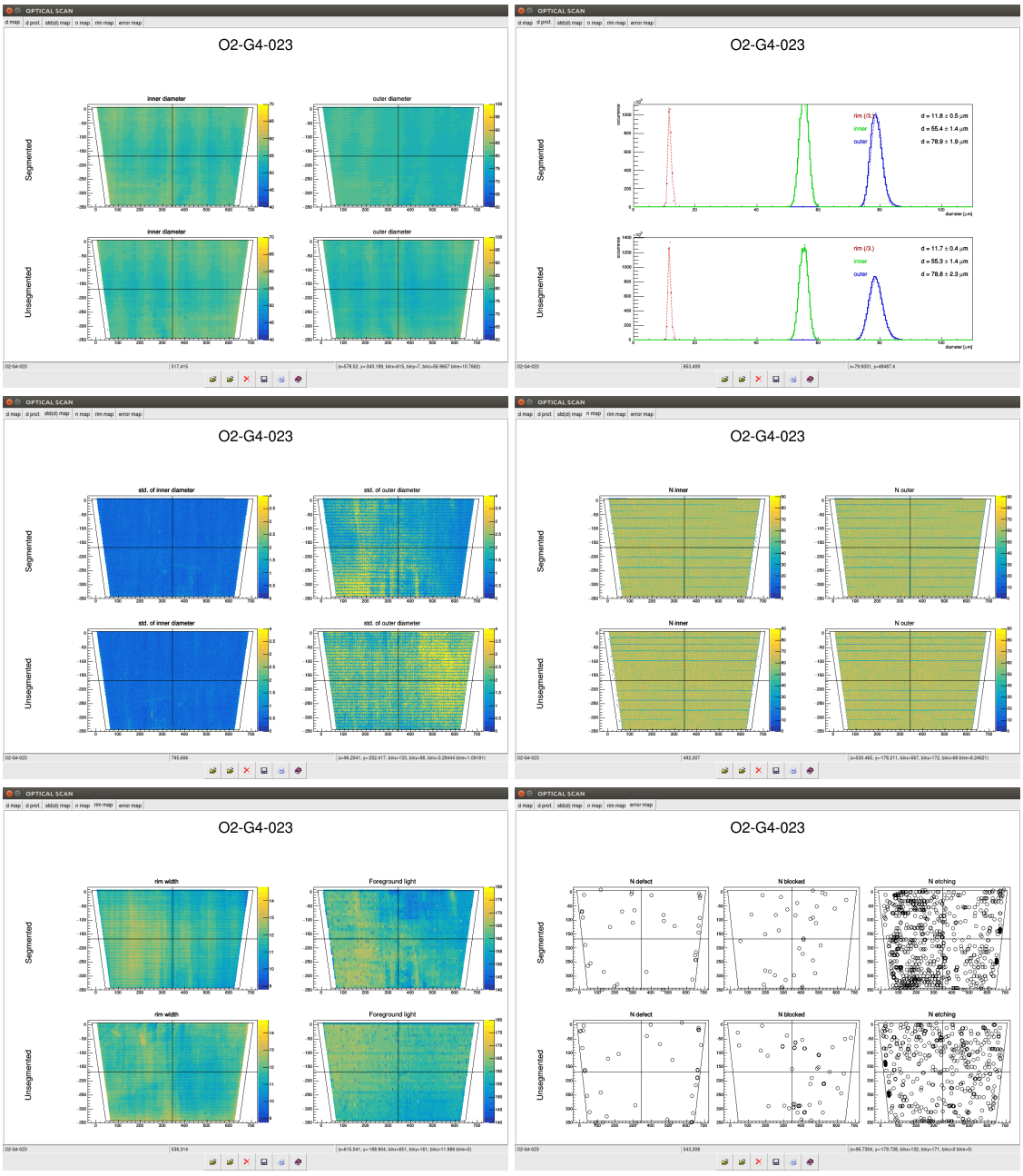

FIGURE 23 Example screenshots from the optical part of the TPCQA GUI [1]. It merges two scans from the two sides of a foil (segmented and unsegmented). The first tab shows the diameter maps, the second tab shows the diameter distributions along with their mean values determined from Gaussian fits. On the third tab, the standard deviation maps are drawn, on the fourth the number density maps, on the fifth the rim width maps and the foreground light maps, and finally, on the sixth, the error maps are plotted.

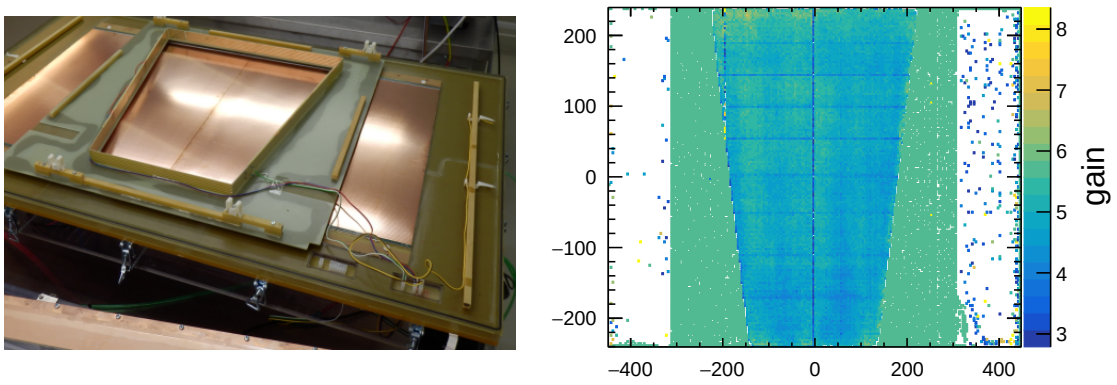

FIGURE 24 Gain scanning equipment from the Budapest QA center (left) along with a measurement result (right), where the x- and y-axis shows their size in mm and the measured gain is shown as a colormap. The edges are covered with a plexiglas plate, their shielding effect is also visible at the edges of the right figure.

The measurement itself is sensitive to external effects. For example one has to be careful to not switch on the neon light in the room, as the noisy electronics of the neon lights can affect the gain measurement. Using a huge volume the gas uniformity and purity can be crucial, thus systematic studies have been taken to check the effects of the used gas flow and the direction of the flow. From a physics point-of-view, the gas flow should be as high as possible to minimize the deterioration of the gas quality (from e.g. diffusion at the walls of the box), because the gain measurement is sensitive to the gas mixture. From an economic point-of-view, it should be minimized. After careful studies and optimization, the gas flow was set to 5 l/h. The direction of the flow was also investigated and found to be negligible within the statistical error of the measurement. However, the foils' insulator surfaces still charge up [139], and as a result of that, the effective gain of the foils can change over time. An example of this phenomenon is shown in Figure 25, where the average amplification μ of the foils is plotted as a function of time. In the example figure, three consecutive measurements were performed on the same foil that was kept under the same conditions. During the four hours of these measurements, a significant charge-up can be observed. The procedure of the measurement was adapted to this discovery, the foil is irradiated with the ^{55}Fe source for several hours before the measurements, and with quick control measurements we make sure that the saturated values are used for the gain calculation, i.e. for both the high-voltage measurement and for the reference.

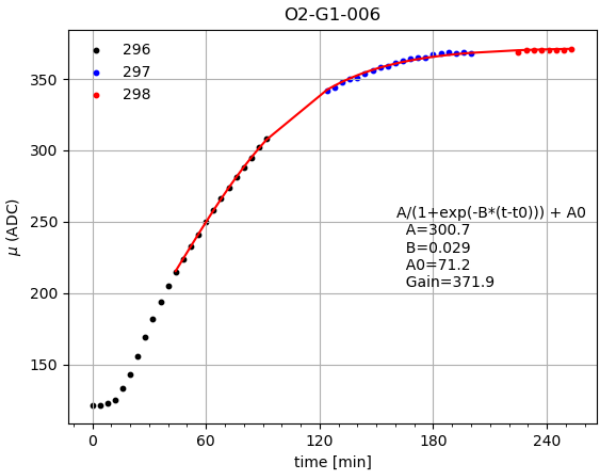

FIGURE 25 Example figure for charge up, showing the average amplification (μ) of the foil calculated in 4 minute-long intervals, for 3 consecutive measurements (labeled 296, 287, 298). Each measurement started with some time offset, but the foil was kept under the source and in the measurement box. The charge-up shows saturation, after 3 hours, and the gain is calculated from the saturated values of both the high-voltage measurement and the reference.

6 THE GEM CORRELATION STUDY

There is no universal formula which connects the hole parameters with the gain. Garfield and Magboltz simulations were performed to gain insight into their relationship [140]. Smaller, 10cm×10cm GEMs were studied in the Helsinki QA Center [136], and although it shows promising agreement, it does not guarantee results for the significantly larger GEMs of the TPC Upgrade. According to all studies, as well as our observations, the gain correlates positively with the bottom diameter of the GEM foils. In this section, using the measured gain and the measured diameter maps, we attempt to find a quantitative description of the phenomena.

For IROC S foils, the correlation between the gain and the bottom hole diameters is remarkably strong, see Figure 26, where the logarithm of the gain is plotted as a function of the bottom diameter. This agreement showed that in the measured range we can use a simple gain prediction formula

$$ln(\mathrm{gain}) = \mathrm{G}(\mathrm{d}_0 - \mathrm{d}_{\mathrm{bottom}}), \tag{24}$$

where d_0 is a constant that incorporates the effect of various environmental factors, e.g. the gas quality and the gas flow velocity. The G parameter is the gain coefficient, from the fit to the IROC S foils $G = 45.6 \pm 0.1$ mm^{-1} was obtained. As there is no reason to assume different behavior for the other type of the foils, this value is considered universal and will be used for the gain calculation of all foils.

The exact dependence on the middle holes are unknown. We consider the generalization of Equation 24 to the linear combination of the different diameters in the form

$$ln(\mathrm{gain}) = \mathrm{G}(\sum_{\mathrm{k}} \mathrm{d}_{0,\mathrm{k}} - \mathrm{d}_{\mathrm{k}}\mathrm{g}_{\mathrm{k}}), \tag{25}$$

where g_k are the individual weights for the different diameters, fulfilling the $\sum_k g_k = 1$ normalization criteria. The k index marks the top, bottom, and middle diameter. According to [140] as well as our observations, the gain correlates

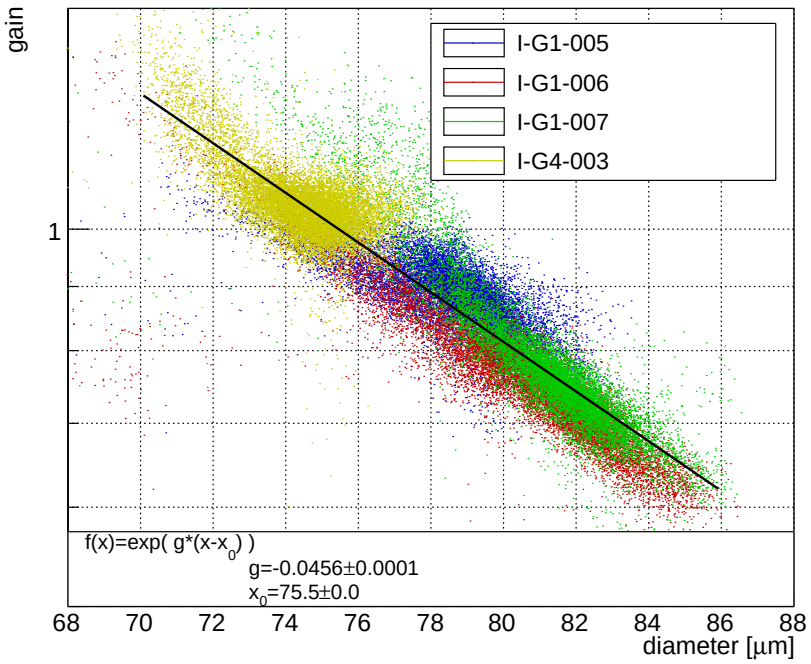

FIGURE 26 The logarithm of the measured gain plotted as a function of the measured (bottom) hole diameters. The figure hints an exponential dependence as parameterized in Equation 24. The values obtained from a fit will be considered universal for other type of foils.

negatively with the middle parameter, so the weight of d_{middle} was forced to be negative.

For each foil, the linear combination $\sum_k d_{0,k} - d_{\text{k}} g_k$ was generated and the corresponding gain was calculated. These maps were simultaneously fitted to the measured gain maps, respectively. The fit was performed in four separate classes; for IROC S-, for IROC LP-, for OROC S and for OROC LP foils, to avoid any bias. The gain coefficient G was fixed from the IROC S fit of Figure 26, the rest of the parameters are kept free.

It was found, that all foils prefer to have negative correlation with the middle holes, and tend to correlate with the average of the top and bottom holes, as opposed to our naive assumption of correlation only with the bottom holes. That assumption worked remarkably well for the IROC S foils, because the foil diameters also correlated with each other. Although it is desired, not all foils exhibit this property as they are very sensitive to their production environments. From the simultaneous fits, a good agreement is achieved across all foils with weight parameters $d_{\text{middle}} = -0.3$, $d_{\text{top}} = 0.8$ and $d_{\text{bottom}} = 0.5$. These parameters describe well all four classes of the examined foils. Figure 27 shows examples of the best gain predictions obtained with those parameters, compared to the measured gain. The prediction seems to be powerful enough to reveal all major patterns of the measured gain maps. For completeness, the worst foils are also compiled, and are visible in Figure 28. In most cases, the pattern is predicted, just the scale differs. In case of an OROC 2 LP foil, however, the prediction does not seem to pick up the trends, see bottom of Figure 28. The correlation between the measured and predicted gain, for all foils, can be seen in Figure 29. For every foil, the residual of the correlation was also calculated as the ratio of the predicted and the measured gain, and is shown in Figure 30. The prediction power can be characterized by the width of these distributions. It does not exceed 10%, that is the accuracy this analysis.

The QA criteria for the optical scan was determined with the gain-optical correlation in mind, and is summarized in Table 2, according to the traffic light system. The final evaluation of the foil is given by the worst case.

color code	hole RMS	rim mean	hole deviation
green	$< 4\mu$m	$< 15\mu$m	$< 5\mu$m
yellow	N/A	15-19 μm	5-10 μm
red	$> 4\mu$m	$> 19\mu$m	$> 10\mu$m

TABLE 2 The optical QA criteria. The hole RMS is calculated for each (top, middle and bottom) holes. The rim is defined as top-middle and bottom-middle. The last column, the deviation is calculated form the mean of the already measured foils.

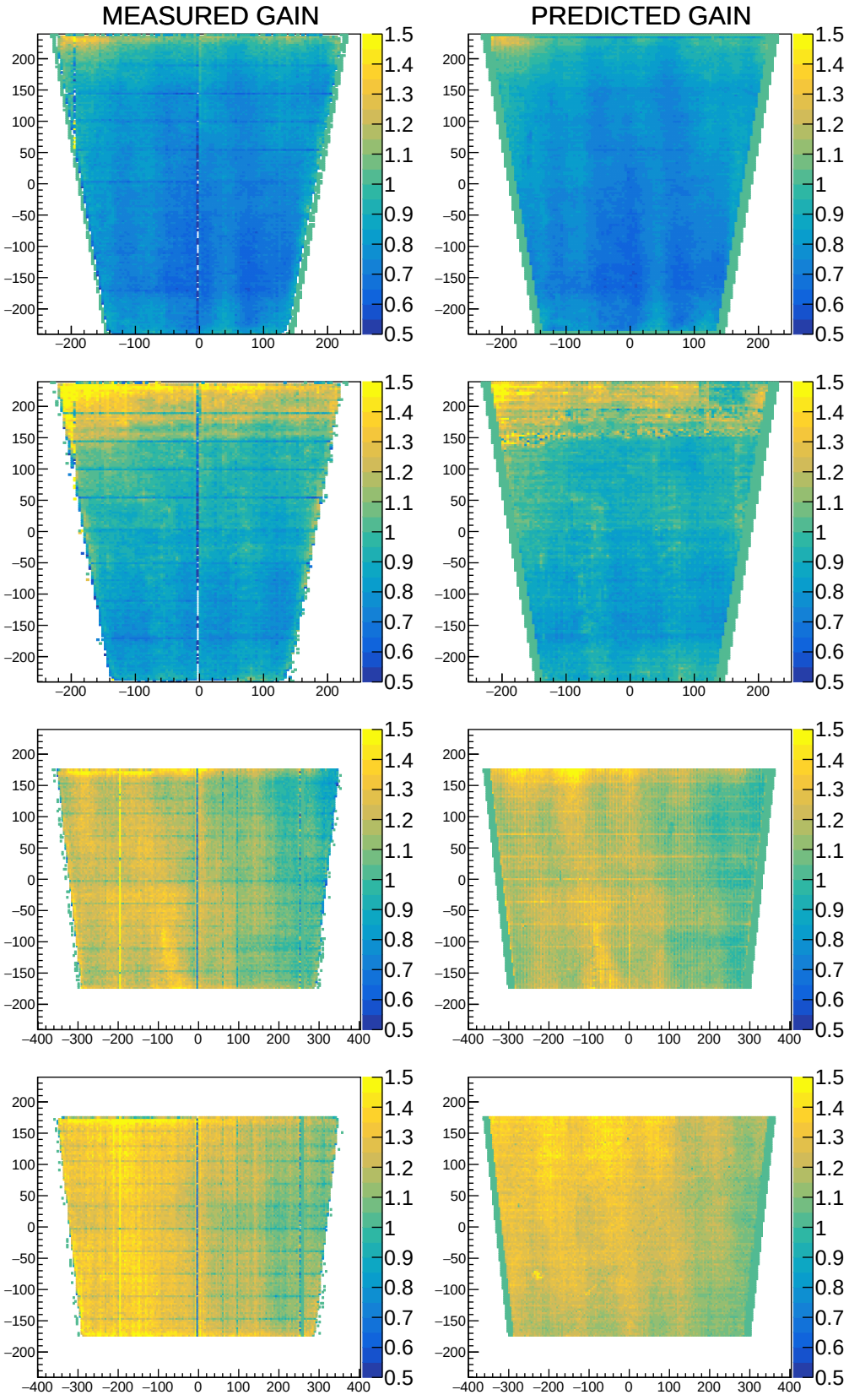

FIGURE 27 Selected best gain predictions along with the measured gains for each foil type measured in the Budapest QA Center, IROC S, IROC LP, OROC 2 S, OROC 2 LP, respectively.

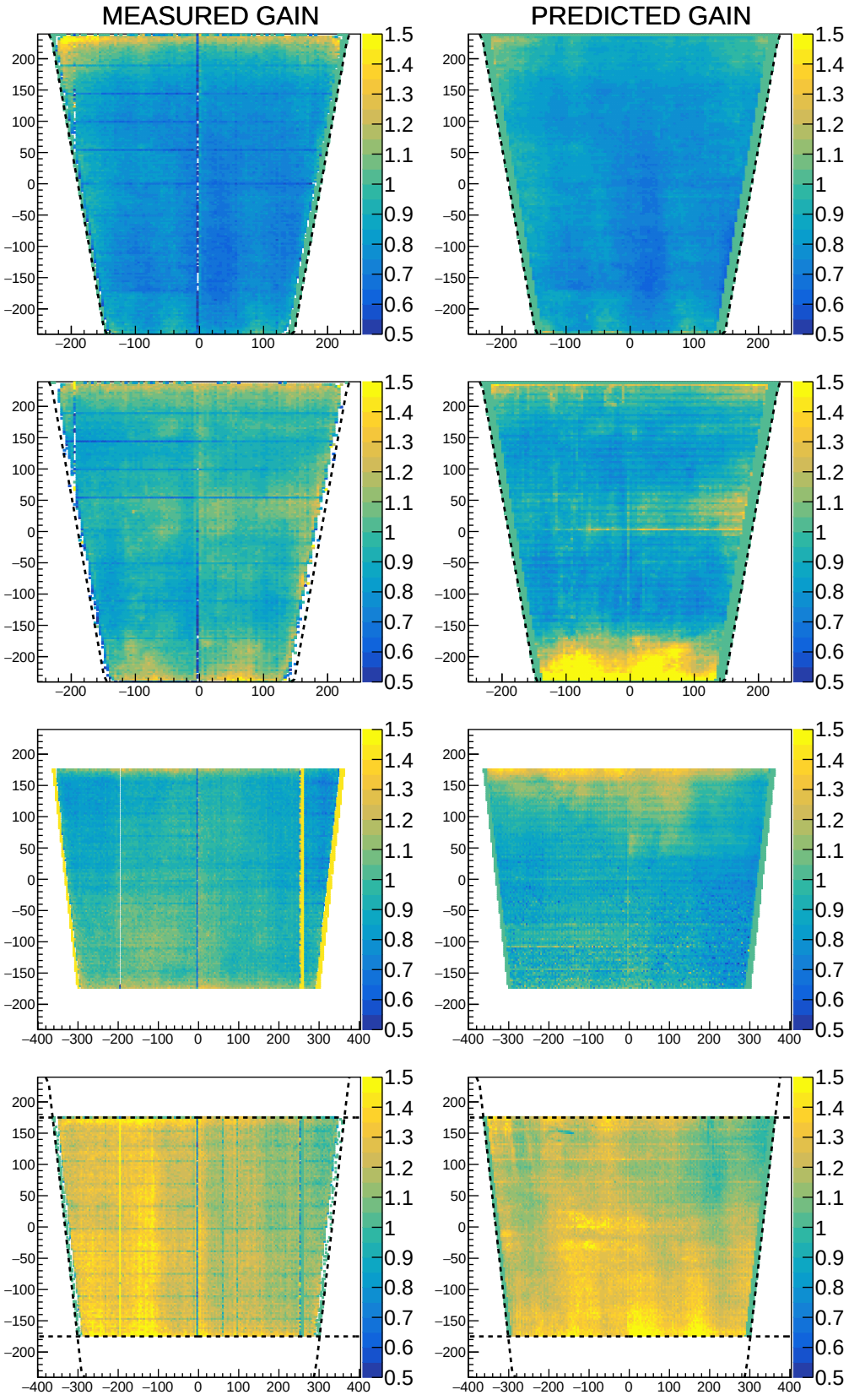

FIGURE 28 Selected worst gain predictions along with the measured gains for each foil type measured in the Budapest QA Center, IROC S, IROC LP, OROC 2 S, OROC 2 LP, respectively.

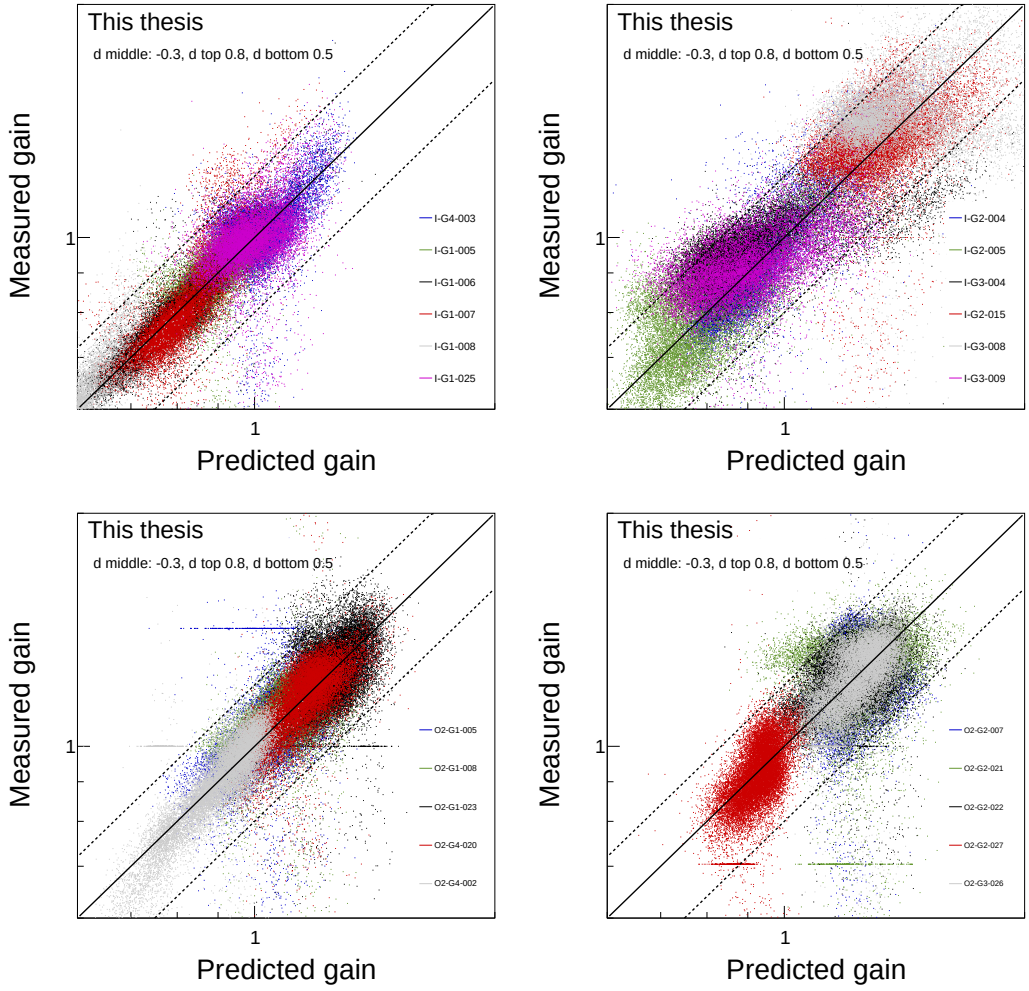

FIGURE 29 Correlation between the optical parameters and the gain for all measured foils. The IROC (top row) and OROC2 (bottom row) foils are treated separately, as well as Standard Pitch foils (left) and Large Pitch foils (right). The dotted lines in each figure show the $\pm$ 20% deviation from unity.

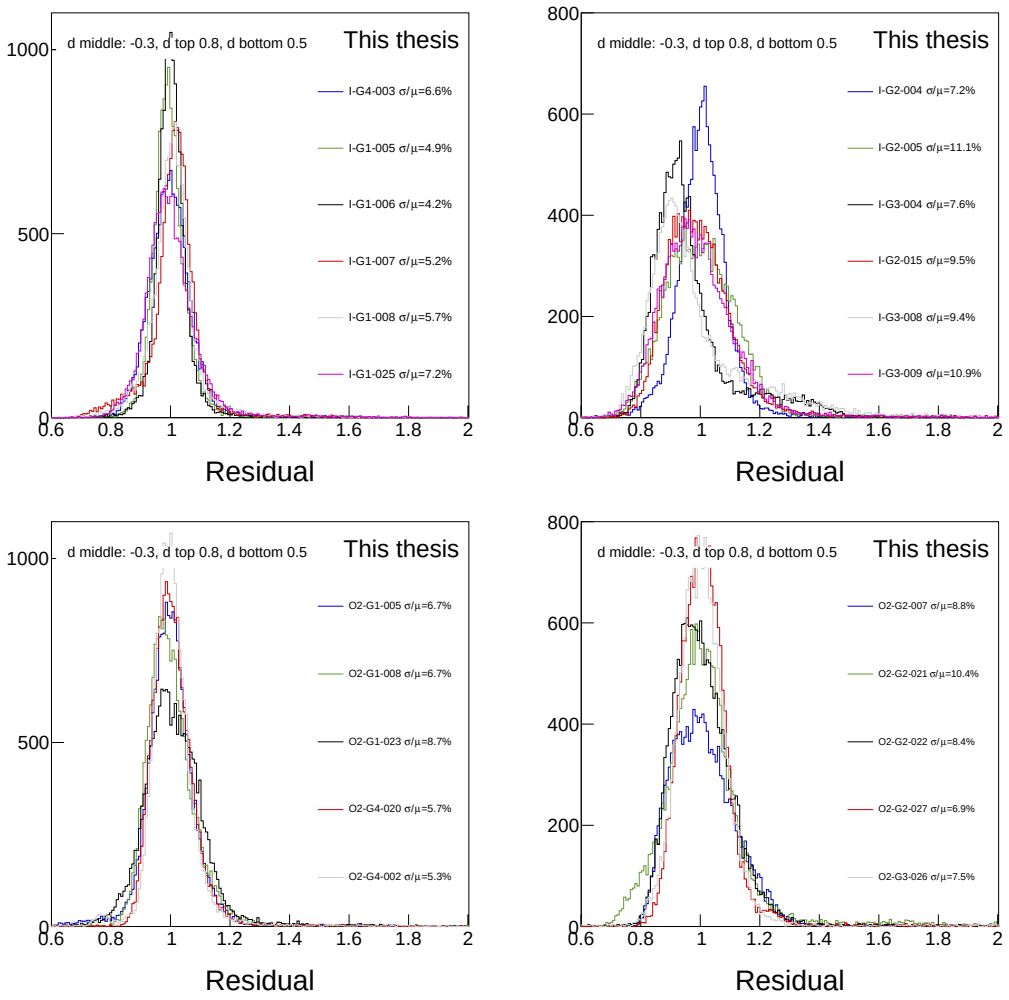

FIGURE 30 The residuals of the correlation between the optical parameters and the gain, calculated as the ratio of the predicted gain and the measured gain. The prediction power can be characterized by the width of these distributions, indicated in the label for each foil. Top row shows the IROC foils, the OROC2 foils are at the bottom. In the left (right) column the Standard Pitch (Large Pitch) foils are shown.

Part III

Jet shape modification analysis

In this part, the analysis of $\sqrt{s_{\mathrm{NN}}}$ = 2.76 TeV pp and Pb–Pb ALICE data will be presented. The physics motivation is to compare the jet shapes in pp collisions with the jet shapes measured in Pb–Pb collisions. The jets are extracted via the two-particle correlations method. With this comparison the goal is to see how the medium created in Pb–Pb collisions affects either the jet fragmentation, or the evolution of the jets.

The part starts with an introduction, reviewing the relevant jet reconstruction and correlation measurements in chapter 7. The description of the event and track selection (trigger, centrality) follows in chapter 8. This chapter also details the tracking in the ALICE experiment in general, and introduces the two track cuts used along this thesis. The QA of the data is also presented there. Then chapter 9 describes the analysis method. In chapter 10 the corrections applied to the ALICE data are presented. The two dominant ones are the efficiency, the acceptance corrections, and the role of other, standard ALICE corrections like the track merging correction and the resonance cut is also investigated. The chapter ends with the Monte Carlo validation of the method. In chapter 11 the systematic uncertainties are discussed, each source has a separate section with comparison figures supporting the conclusions. Two type of errors are considered, point-by-point (PbP), and scaling (SC) errors. The final uncertainties along with their types are summarized in Table 3. Finally, in chapter 12, the final results, as well as Monte Carlo comparisons are presented, and the conclusions from the analysis are drawn.

7 INTRODUCTION

This analysis focuses on jet shapes, especially how the presence of the QGP alters the observed jet shapes. Initial state effects, like modification of the PDFs, can be ruled out. They play a sub-dominant role, as pointed out in Ref. [141]. The source of this modification should then be a final state effect, it can be either the modification of the fragmentation functions, or the difference can come from the quenching of the jet in the medium.

The jet fragmentation function was measured at $\sqrt{s_{\mathrm{NN}}}$=2.76 TeV collision energy in CMS [142], and they found it exhibited a centrality-dependent modification. The modification was the strongest in the most central centrality bin. This result is in accordance with the theoretical expectations [143, 54, 144, 145, 146], that predicted a similar modification, and suppression of high transverse momentum particles. Enhancement of low-p_{T} charged particles ($p_{\mathrm{T}}<3$ GeV/c) in Pb–Pb collisions as compared to the pp results was also observed. There are other measurements indicating that the energy is redistributed inside the jet cone in the presence of the medium [147, 148, 149]. Central to peripheral jet yield ratios were measured for different jet radii R up to $R = 0.5$ [150], and a difference of up to 30% was observed for $p_{\mathrm{T,jet}}<100$ GeV/c. Similar conclusion was reached in other measurements [151, 152]. A modest, but significant centrality-dependent modification of the fragmentation function was also seen in ATLAS [153] for $100<p_{\mathrm{T,jet}}<387$ GeV/c jets.

The other conjured source of the modification is the jet quenching phenomenon (see e.g. Refs. [154, 155], and section 1.3), in which the jet shape modification is brought about via the different energy loss mechanisms in the presence of QGP as compared to vacuum. In Ref. [156] it is calculated and shown with a numerical study, that the jet quenching occurs because the medium cannot resolve the inner structure of the jets, if the color coherence of the system is preserved. The color charge than behaves as a single, effective charge in the medium. As a result of jet quenching, jets of heavy-ion collisions are narrower in high p_{T}

(e.g. above 100 GeV/c transverse momentum) than that of pp collisions [157]. In lower momenta, however, a broadening is expected and measured [158, 159, 160]. A similar, low-p_{T} broadening was also measured in jet-track correlations in CMS [161].

In this analysis, the transverse jet shape is studied using two-particle correlations. The analysis is similar to that of Ref. [159], but we are concentrating on the pseudorapidity direction and higher transverse momentum. A narrowing of the jet shape is observed while increasing the trigger momentum ($8<p_{\mathrm{Tt}}<15$ GeV/c). A similar narrowing was also reported using reconstructed jets, although in higher transverse momentum, $40<p_{\mathrm{T,jet}}<60$ GeV/c [157].

8 EVENT AND TRACK SELECTION

Event selection

In the analysis, 13.66 M Pb–Pb events (recorded in 2010 during Run 1) were studied. As the analysis focuses on medium properties, it is a common technique to compare heavy-ion results with results from proton-proton collisions. As a reference, we collected 51.5 M pp events of pp at the same center of mass energy.

As mentioned before in section 2.3, during the data taking we apply certain triggers, e.g. we do not record automatically everything but apply an online filter to get rid of data coming from e.g. beam-gas interactions or other unwanted sources. The trigger for both pp and Pb–Pb was minimum bias, which applies the least special conditions among the triggers. Another common choice is the central trigger, where most central events are preferred, but this was not available for the current dataset. Another possibility is to use the jet trigger, signaled by the ElectroMagnetic Calorimeter, this analysis, however, relies on the two-particle correlation technique, so this trigger choice was discarded as well. The minimum bias trigger was defined by a combination of hits in the V0 detector and the ITS [162], its two innermost layers are required to fire in coincidence with the V0. Also, it was required to be in coincidence with the crossing lead/proton bunches.

The centrality was determined by comparing the multiplicity as measured by the V0 with Glauber simulations [162, 163]. With the minimum bias trigger we do not impose any constraint on the centrality, so the centrality distribution for Pb–Pb is expected to be flat, in accordance with the measured one shown in Figure 31.

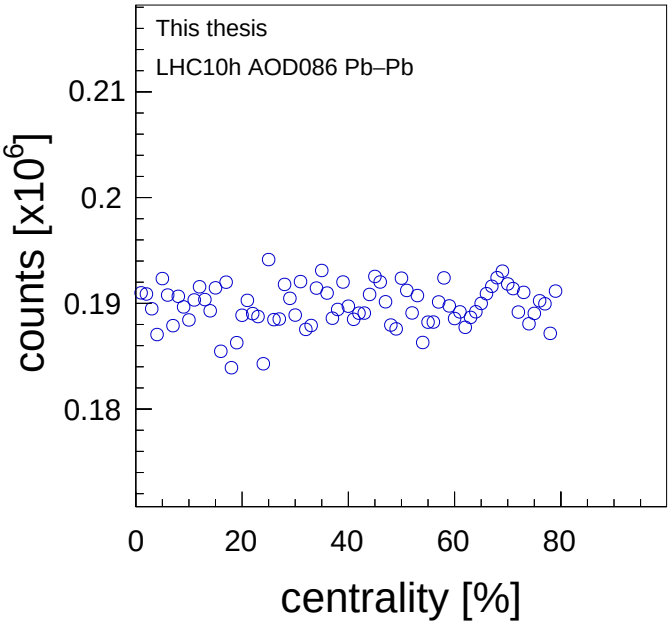

FIGURE 31 Centrality distribution of the Pb–Pb events with the minimum bias trigger.

Tracking in the ALICE experiment

Description of tracking follows closely the discussion presented in Ref. [164]. The reconstruction of tracks in the ALICE experiment is based on the technique of Kalman filters. In general, this technology is an iterative procedure, resulting from the successive sequencing of a prediction phase and a filtering phase. In the prediction step, the track parameters are extrapolated to find the next element, taking into account the uncertainties induced by interactions with matter (e.g. multiple diffusion, energy loss). If a space point is found in the prediction area, the filtering step will then recalculate the track parameters, taking into account the additional constraints imposed by this new point. Then we can search for the next space point and so on.

In the ALICE experiment, this iterative procedure is performed in 10 steps and with various detectors, the ITS, the TPC, the TRD and the TOF, and in each step we include or omit a different detector. The procedure is illustrated in Figure 32. We can also differentiate three stages, in the first, we estimate the track parameters with a helicoidal fitted to 3 points, the primary vertex and two points from the outermost region of the TPC. Those two points are also called the seed because they are the starting point of the procedure, and they are required to be separated by a few rows of pads of the TPC. During this initial approximation, the transverse radius of the vacuum tube (3 cm) is taken as uncertainty of the transverse position of the vertex. Figure 32 shows only one track, but in reality we have to deal with many tracks. So when the seeds are found, they have to be sorted according to their estimated transverse momentum. Then the search for

additional track points starts, each seed is extended from one row or pad to another in case of the TPC, and one layer from another once it reaches the ITS, up to the primary vertex. When a new point is found in the allowed region of the track, the track parameters are recalculated, corrected for energy loss and Coulomb diffusion. In order to perform these corrections, the mass of the particle has to be known. That either comes from the $\mathrm{d}E/\mathrm{d}x$ measurement of the TPC (considering only $\mathrm{e}^{\pm}$, $\mu^{\pm}$, $\pi^{\pm}$, $\mathrm{K}^{\pm}$ and $\mathrm{p}^{\pm}$ masses), or in case that information is not available, the charged pion's mass is assumed.

During the second stage, tracks are propagated from the vertex to the outside of the detectors, through the ITS and the TPC, then the TRD reconstructs its tracks independently, and the global tracking only includes that information if its transverse momentum is above a certain threshold (typically 3–5 GeV/c). Whenever possible, tracks are matched with the hits of the TOF detector.

In the third stage, all information being collected already, we refine the parameters with minimizing against the distance at the closes approach (DCA) to the vertex. The primary vertex is computed again using this refined information.

Track selection

The approach described above can be further specified once one considers detector-specific constraints, there are a lot of parameters to fine-tune. In the analysis, the track selection was performed by a set of conditions, summarized in the so-called TPCOnly track cut. If not mentioned otherwise, this cut will be used throughout the text, for both pp and Pb–Pb, and will be referred as "cut 1". As its name suggests, it relies mostly on information from the TPC detector, so its accepted pseudorapidity range is constrained to the TPC's acceptance, $|\eta|<0.8$. To understand this track cut in detail, recall the pad-row readout planes of the TPC, detailed in chapter 3. A useful quantity to introduce is the notion of the TPC cluster. When a charged particle travels through the TPC, it ionizes the gas inside which brings about a signal on a given pad-row at the endcaps. The criteria for a bunch of signals to be called a cluster is to have the imposed charge to exceed a certain threshold in a search window of 5 pads in wire direction and 5 bins in time direction. The maximum number of clusters per track is then 159. One can see that the number of TPC clusters is related to the track length, because low-p_{T} tracks usually will not reach the outer wall of the TPC (they bend more) so low-p_{T} tracks have fewer TPC clusters assigned. With cut 1 we require a minimum of 70 clusters to accept the tracks, this acts as a threshold trigger and ensures that we rely on enough information to fit the tracks, because tracks are determined by fitting the fired and accepted detector points. The track then can be further restricted based on the goodness of that fit, the condition: $\chi^2/\text{TPC cluster} < 4$ was

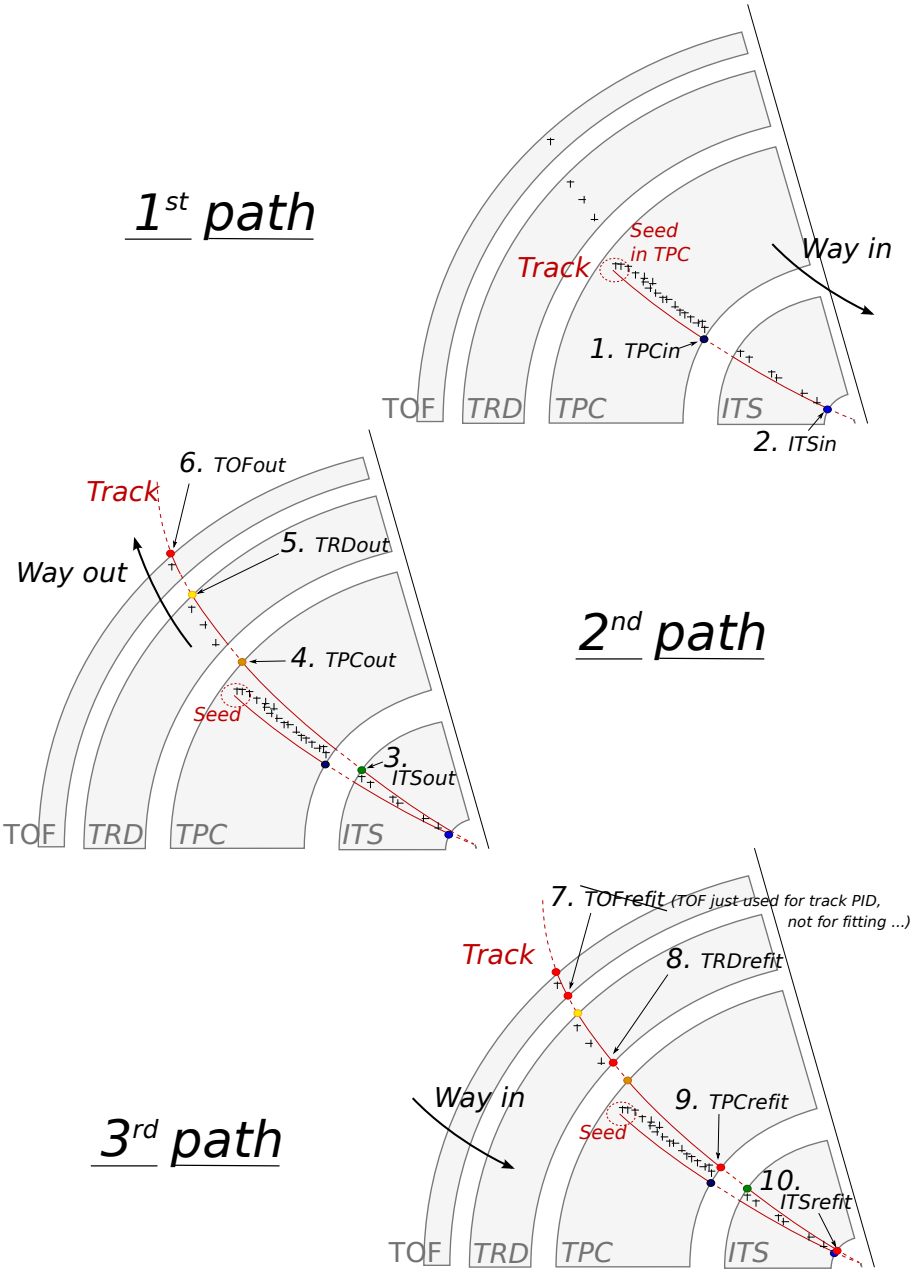

FIGURE 32 Principles of tracking of an event in the ALICE experiment, showing the three successive paths allowing to build a track and refine its parameters. Numbers ranging from 1 to 10 mention the bits that are activated in case of success during the propagation of the Kalman filter at the considered stage. Figure from [165].

applied here. The vertex was let to be determined by the SPD detector. Then the tracks' accepted distance of closest approach (DCA) to that vertex was maximized at 3 cm for the beam direction, and at 2.4 cm in the transverse plane. The cut was set to not accept kink daughters, which gets rid mostly of decaying tracks. These are mostly resonance decays whose track do not originate from the vertex. These would contaminate the sample, as the two-particle correlation method assumes a common vertex. At this low level this is all one can do about to exclude these particles, but later, more sophisticated cuts will ensure the purity of the tracks (see section 10.4).

In later systematic studies (detailed in chapter 11), another track cut will be tested, that will be referred as "cut 2" along the text. The cut itself is similar to the default cut 1, but has a tighter DCA cut to the vertex. It also includes another detector on top of the TPC and SPD, the ITS, and also requires a threshold for the ITS detector to form a cluster. It refits the tracks with points obtained by the ITS. Another difference is with the TPC setup, instead of the cluster-limit threshold applied in cut 1 (minimal number of TPC clusters), this cut sets a minimum to the crossed rows (N_{CR}) in the TPC. The two quantities are similar, but the latter takes into account the phenomenon of missing clusters. Clusters which should be in the path of the charged particle can be missing because of various reasons (e.g. charge is below threshold due to baseline shifts), and the number of crossed rows counts this effective cluster track length. It is an important quantity, because the p_T resolution scales with N_{CR}^2. The N_{CR} was set to 120.

Figure 33 and Figure 34 show the inclusive η and φ distributions for the two track selection criteria, respectively. The φ-uniformity justifies the use of cut 1 as a default cut despite its worse momentum resolution. Cut 2, however, has a pathological shape in φ, and any correlation analysis benefits from a uniform φ-distribution. The fact that a similar result is obtained by both cuts demonstrates the robustness of the analysis.

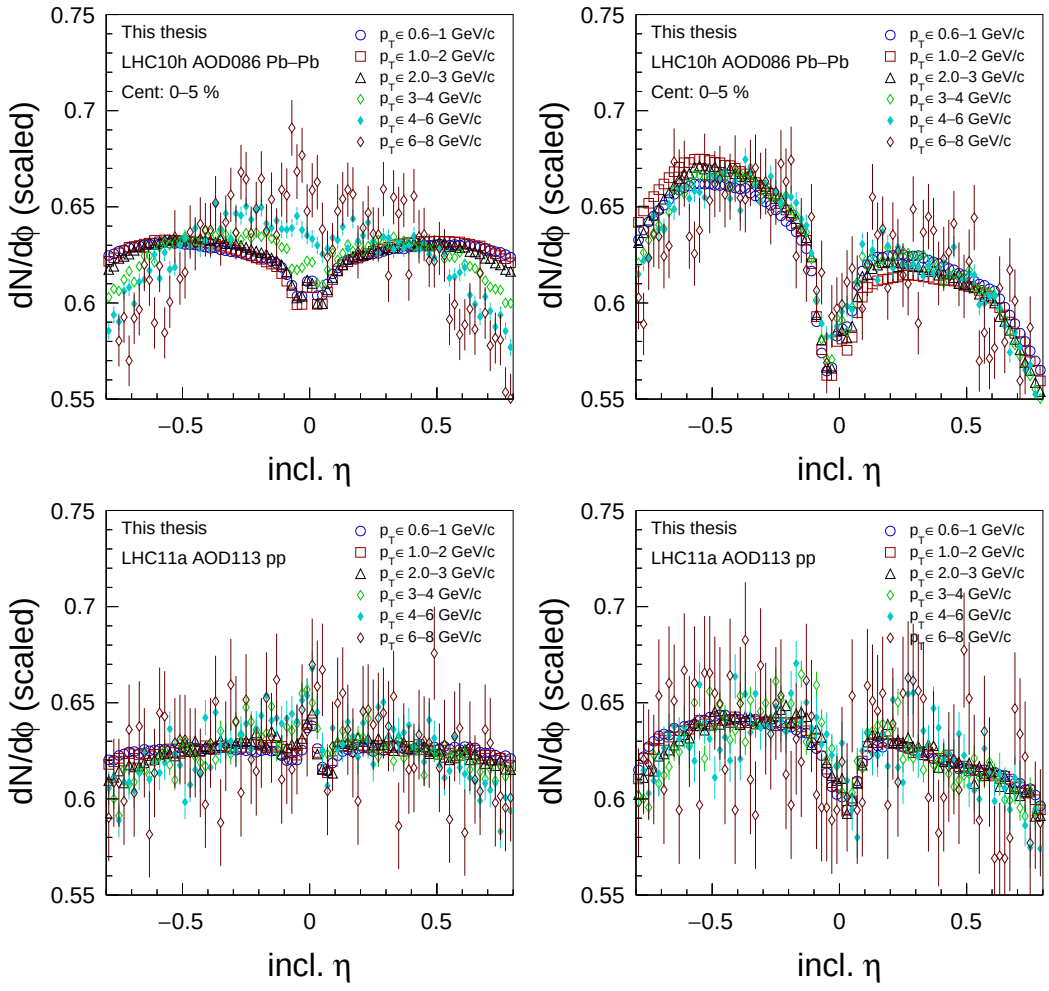

FIGURE 33 Inclusive η distributions for "cut 1" (left) and "cut 2" (right) track cuts in various p_{T} bins in Pb–Pb (top) and pp (bottom), respectively.

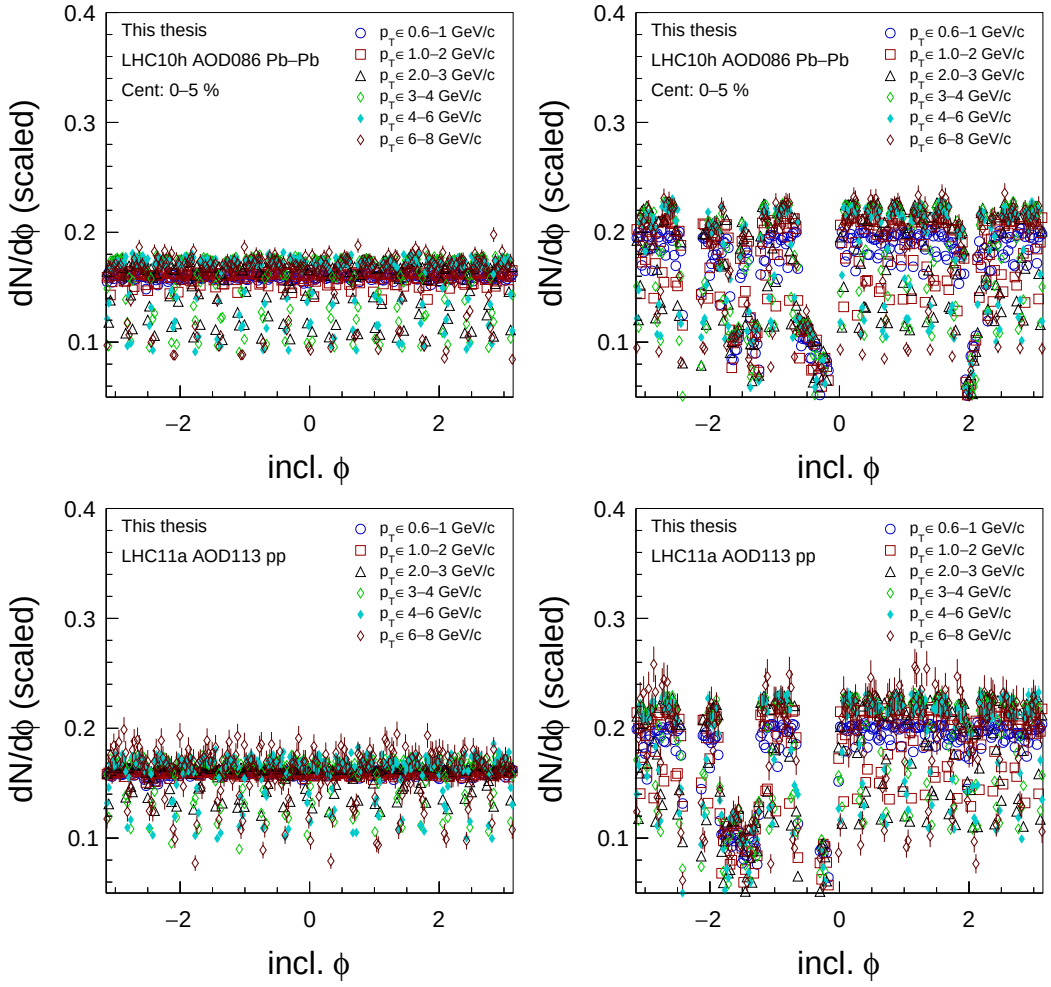

FIGURE 34 Inclusive φ distributions for "cut 1" (left) and "cut 2" (right) track cuts in various p_{T} bins in Pb–Pb (top) and pp (bottom), respectively.

9 THE TWO-PARTICLE CORRELATIONS METHOD

As opposed to jet-finding algorithms, the two-particle correlations method extracts jets from the events in a fundamentally different way. Here a trigger particle is selected, and it is required to fall into a preset, high-p_{T} window, to get rid of most of the thermal particles abundant in heavy-ion collisions. Those thermal particles have transverse momenta typically below 1.5 GeV/c, so with the high-p_{T} trigger of this analysis (above 6 GeV/c), it is likely to capture dominantly fragments of a high-p_{T} jet. We can also expect the trigger to be close to the jet axis. Then we examine all other particles in a given event, and collect those that fall into another p_{T} window. These are called the associated particles, and we go lower with their p_{T} than with the trigger's p_{T}, as we would like to collect even some of the thermal contribution of the jet. We then calculate the pseudorapidity ($\Delta\eta = \eta_{\mathrm{trigg}} - \eta_{\mathrm{assoc}}$) and azimuthal angle differences ($\Delta\varphi = \varphi_{\mathrm{trigg}} - \varphi_{\mathrm{assoc}}$) of the trigger and associated particles. We continue to do this for all trigger particles we can find in an event, and analyze all events. An important step in the analysis procedure is to correct for acceptance. The procedure is detailed in section 10.2, here we just note that acceptance correction was applied.

With this two-particle correlations method, the jet peak emerges naturally around ($\Delta\eta$, $\Delta\varphi$) = (0, 0). In this work, however, we focus on correlations in pseudorapidity, as the azimuthal direction was already studied more extensively (e.g. Refs. [166, 160, 167]). In order to do so, the ($\Delta\eta$, $\Delta\varphi$) correlation is projected to $|\Delta\varphi| < \pi/2$, that is called the near side of the jet. The jet fragmentation can be studied more efficiently here in the near side, as the far side ($|\Delta\varphi| > \pi/2$) is more smeared as a result of additional effects. The far side, in fact, is so smeared in the p_{T}-region of the analysis no peak is visible there.

The two-particle correlation method is demonstrated in Figure 35, on the left two figures the raw $\Delta\eta$ distribution and the acceptance correction is shown, the rightmost figure shows the extracted signal, the ration of the two. One can clearly observe that peak associated with contributions from jets.

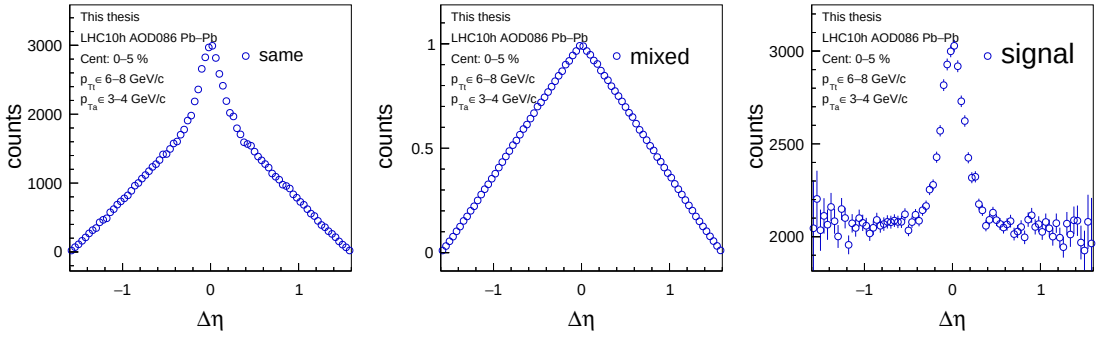

FIGURE 35 Raw, mixed event, and signal histograms to illustrate the mixed event correction, as in Equation 26.

That signal, called the per-trigger yield is defined as

$$Y(\Delta\eta) = C_{\text{single}}(p_{\text{Ta}}) \frac{1}{N_{\text{trigg}}} \frac{\mathrm{d}N_{\text{same}}/\mathrm{d}\Delta\eta}{B \times \mathrm{d}N_{\text{mixed}}/\mathrm{d}\Delta\eta} = C_{\text{single}}(p_{\text{Ta}}) \frac{1}{N_{\text{trigg}}} \frac{\mathrm{d}N}{\mathrm{d}\Delta\eta}. \quad (26)$$

As one can observe also in the right panel of Figure 35, the peak sits on top of a constant background[1], a contribution coming from uncorrelated particles and underlying events. An important part of the analysis is to remove that background to access the peak. Two functions were used to estimate the background and the peak, a Generalized Gaussian

$$f(\Delta\eta) = \text{backg.} + \frac{\text{yield}}{2\alpha\Gamma(1/\beta)} e^{-|\Delta\eta/\alpha|^{\beta}}, \quad (27)$$

and a Gaussian, with $\beta = 2$ substitution in the equation above. The background was approximated by a constant. In both cases, this constant + peak fit was only used to estimate the background. The two fits are shown in Figure 36. In the background estimation, the choice for the peak is rather indifferent. For the primary analysis the Generalized Gaussian (1) was used, because it was more stable across the analysis' various centrality and p_{T} bins, as well for different system types. Results obtained with a Gaussian (2) were used to estimate the systematic error.

Once we extracted the per-trigger yield, and removed the background from the underlying events, we can compare heavy-ion results with results from proton-proton collisions and gain insight to medium-induced phenomena. So similarly to the nuclear modification factor, R_{AA}, we define the per-trigger yield ratio, the I_{AA}:

$$I_{\text{AA}}(|\Delta\eta|) = \frac{Y^{\text{Pb-Pb}}|(\Delta\eta|)_{\text{backg. subtracted}}}{Y^{\text{pp}}(|\Delta\eta|)_{\text{backg. subtracted}}}, \quad (28)$$

i.e. ratio of the yield in Pb–Pb to the yield in pp collisions measured at the same center of mass collision energy. This quantity is sensitive to the modification of

[1] And flow if it was in the $\Delta\varphi$ direction.

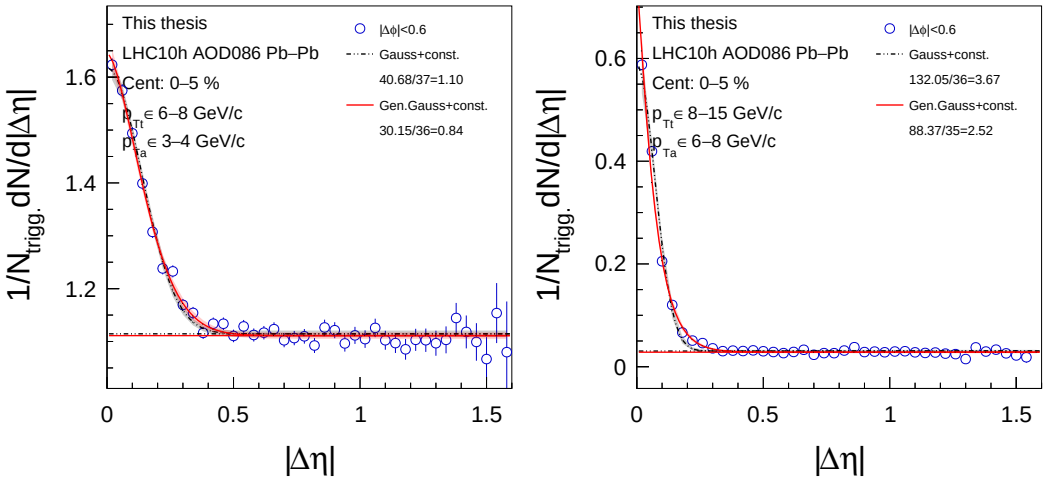

FIGURE 36 Example per-trigger yields with the two fit functions of the analysis for the lowest (left) and highest (right) p_{Tt}-p_{Ta} combinations, respectively.

the jet shape, and it shows a falling trend in case of narrowing, a rising trend for broadening, and would be a constant in case of no shape modification.

As a final investigation, a sanity check of the statistical error propagation is shown in Figure 37. Here the error on the I_{AA} is calculated from the raw pp and Pb–Pb spectra and the mixed events, and shown with a red line. This naive estimate matches the error calculated in the analysis shown with blue squares in the same figure.

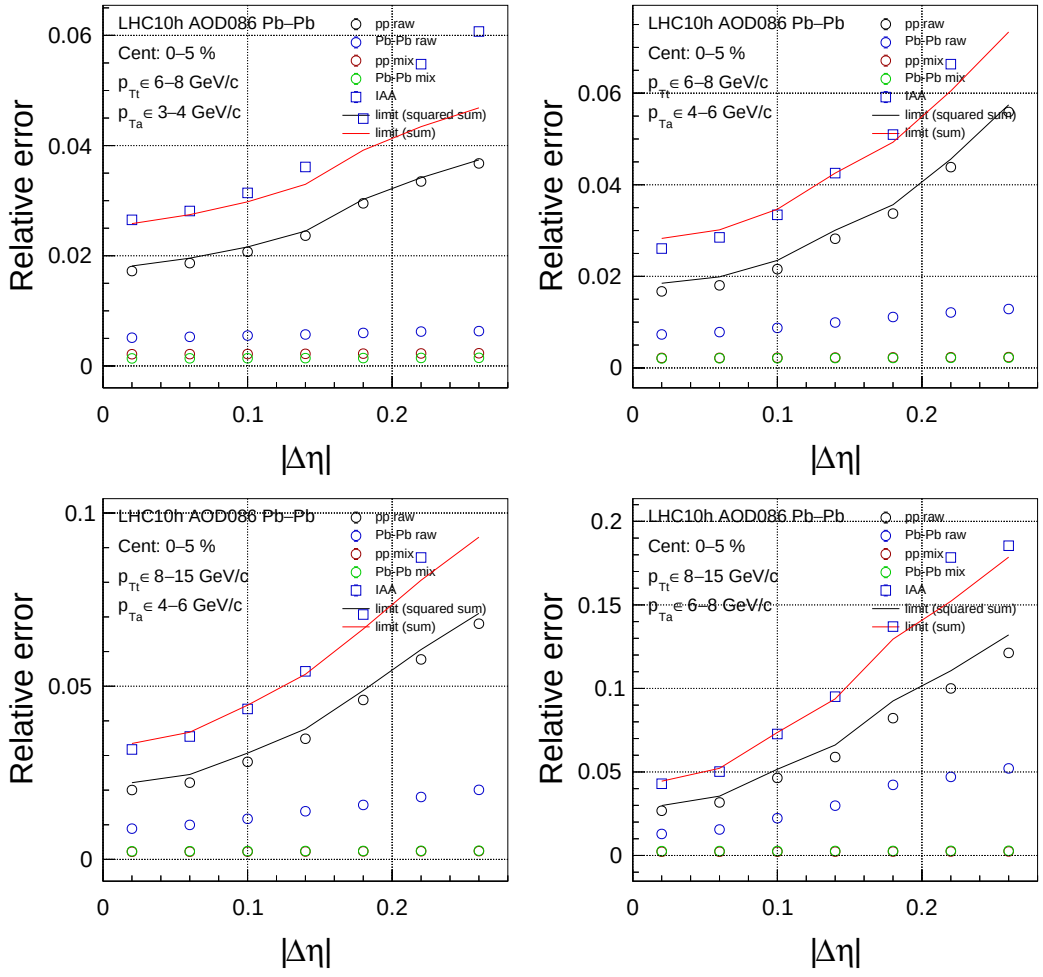

FIGURE 37 The relative error of the I_{AA} (blue squares), and the relative error calculated as a sum of its components, the raw and mixed event errors for pp and Pb–Pb (red line).

10 CORRECTIONS

10.1 Efficiency

Some fraction of all particles are always lost in an experiment, either at the detector level, or at the reconstruction level. We try to estimate this fraction, and correct our measurement so the final results should be as if the measurement conditions were ideal. In the current work, the transverse momentum and the $\Delta\eta$-dependence of the efficiency should be considered. The $\Delta\eta$-dependence of the efficiency was calculated and found to be negligible [168], so the tracking efficiency is considered to be only a function of track p_{T}, for data of both pp and Pb–Pb collisions. The tracking efficiency was obtained from an official ALICE Monte Carlo simulation, production LHC11b10a for pp and LHC11a10a_bis (HIJING standalone, LHC10h anchors) for Pb–Pb collisions.

The single track overall reconstruction correction takes into account both the contamination of the reconstructed track sample with fake primary tracks, and the track reconstruction efficiency. We define the track-to-particle overall reconstruction correction $C^{-1}(p_{\mathrm{T}})$ as

$$C^{-1}(p_{\mathrm{T}}) = \frac{M_{\mathrm{trigvtx}}(p_{\mathrm{T}}) + B(p_{\mathrm{T}})}{G_{\mathrm{trigvtx}}(p_{\mathrm{T}})}. \tag{29}$$

Here M_{trigvtx} denotes the number of properly reconstructed primary tracks and B gives the number of fake and secondary tracks. G_{trigvtx} stands for the number of true charged physical primaries emitted to $|\Delta\eta| < 0.8$ in triggered events where an event vertex was reconstructed. Let us point out that G_{trigvtx} and M_{trigvtx} are functions of the original MC generator p_{T} while B is a function of the reconstructed p_{T}. We assume that the reconstruction correction of the trigger and associated particles are independent. This correction factor is depicted in Figure 38, for both trackcuts (cut 1 and cut 2) and both collisions systems (pp and Pb–Pb).

In order to cross-check the efficiency correction, the inclusive charged track

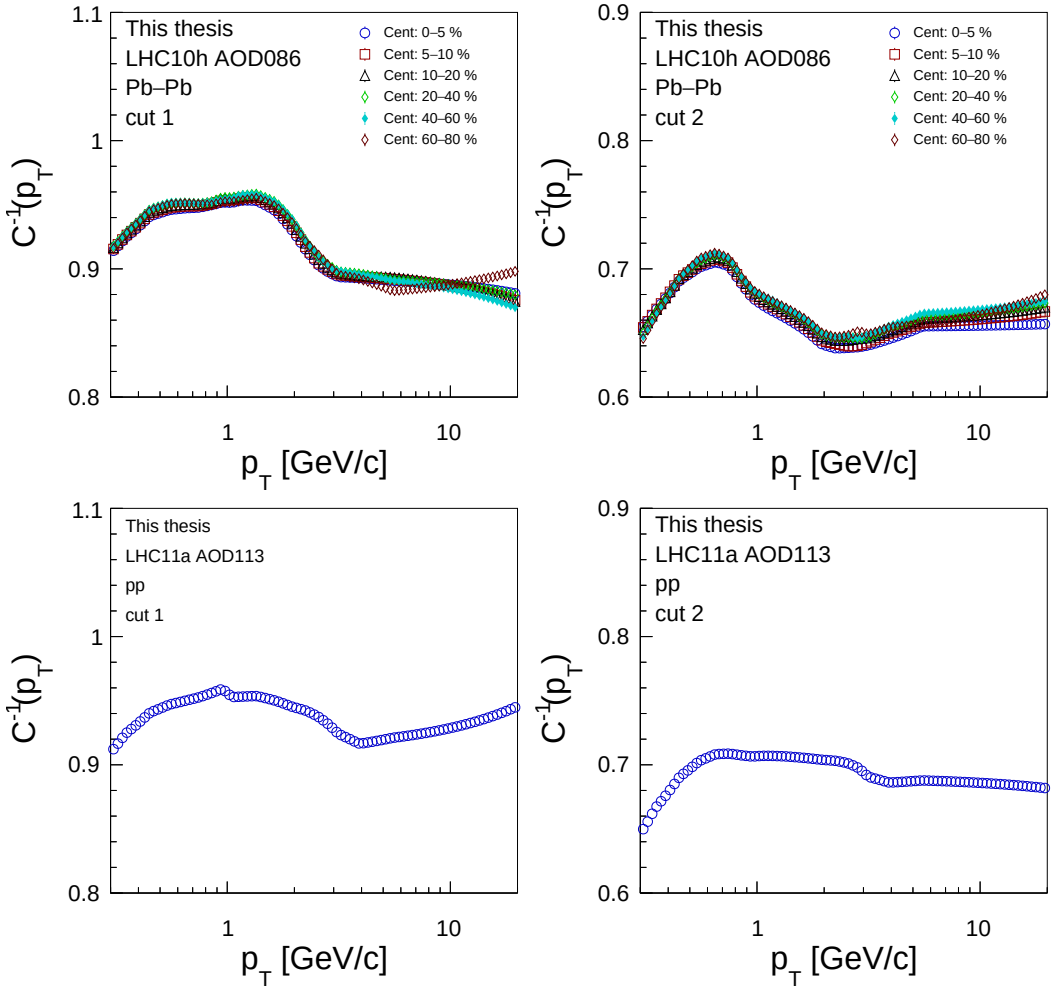

FIGURE 38 The overall reconstruction correction of Equation 29 for the "cut 1" (left) and "cut 2" track cuts in Pb–Pb data (top) and pp data (bottom).

p_{T} spectrum obtained will be compared with the published ALICE results [162]. The comparison is shown in Figure 39 for cut 2 and cut 1, respectively. The agreement is satisfactory for both cuts in the p_{T}-range of this analysis ($3<p_{\mathrm{Tt}}<15$ GeV/c). Further reassurance comes from section 10.5, where all corrections applied to the results are tested and validated. Note that the $\Delta\eta$ or $\Delta\varphi$ dependent histograms will be filled weighted with the overall reconstruction corrector factor of Equation 29.

10.2 Acceptance

The mixed event correction is a technique to correct for primarily the finite acceptance in $\Delta\eta$, but it also corrects for detector inefficiencies, such as dead sectors in the TPC or suppression of the tracks at the TPC sector boundaries. To build the mixed event distribution, the same ($\Delta\eta$, $\Delta\varphi$) histograms are calculated from tracks from different events. This ensures that no jet-like correlation is present there. The more detailed mathematical treatment is given in e.g. Ref. [169].

Since the mixed event can be understood as a geometrical acceptance and detector efficiency correction, it has to be normalized to not exceed 1. Practically it should be 1 at ($\Delta\eta$, $\Delta\varphi$) = (0, 0). Two-track cuts (detailed in section 10.3 and section 10.4), however, cause a dip around (0, 0), so the normalization was determined from the far side, taking advantage of the mixed event's $\Delta\varphi$-independence. One still has to correct for finite binning on the rapidly changing $\Delta\eta$ axis, as depicted in the cartoon in Figure 40. From the similarity of the two triangles (drawn with thick lines), one obtains the following proportionality:

$$\frac{x}{\Delta\eta_{\mathrm{bin}}} = \frac{h+x}{\Delta\eta_{\mathrm{max}}}, \tag{30}$$

where $\Delta\eta_{\mathrm{bin}}$ is the half of the bin width. Then the correction factor is:

$$\mathrm{C} = \frac{h+x}{h} = 1 + \frac{\Delta\eta_{\mathrm{bin}}}{\Delta\eta_{\mathrm{max}} - \Delta\eta_{\mathrm{bin}}}. \tag{31}$$

The normalization of the mixed event should be multiplied by this factor.

Ideally, the mixed event is flat along $\Delta\varphi$ and has a triangle shape in $\Delta\eta$, but in a realistic case, statistical fluctuations and detector inefficiencies distort this shape, so while determining the normalization, not a single bin in ($\Delta\eta$, $\Delta\varphi$) = (0, π) was used, but a projection along $\Delta\varphi$ around the away-side: $\Delta\varphi \in (0.6\pi, 1.4\pi)$. In the other ($\Delta\eta$) direction, two bins around 0 were used.

One can further reduce the statistical errors by merging the mixed event in the highest p_{T}-bins, where their shapes are very similar. Although the error on the

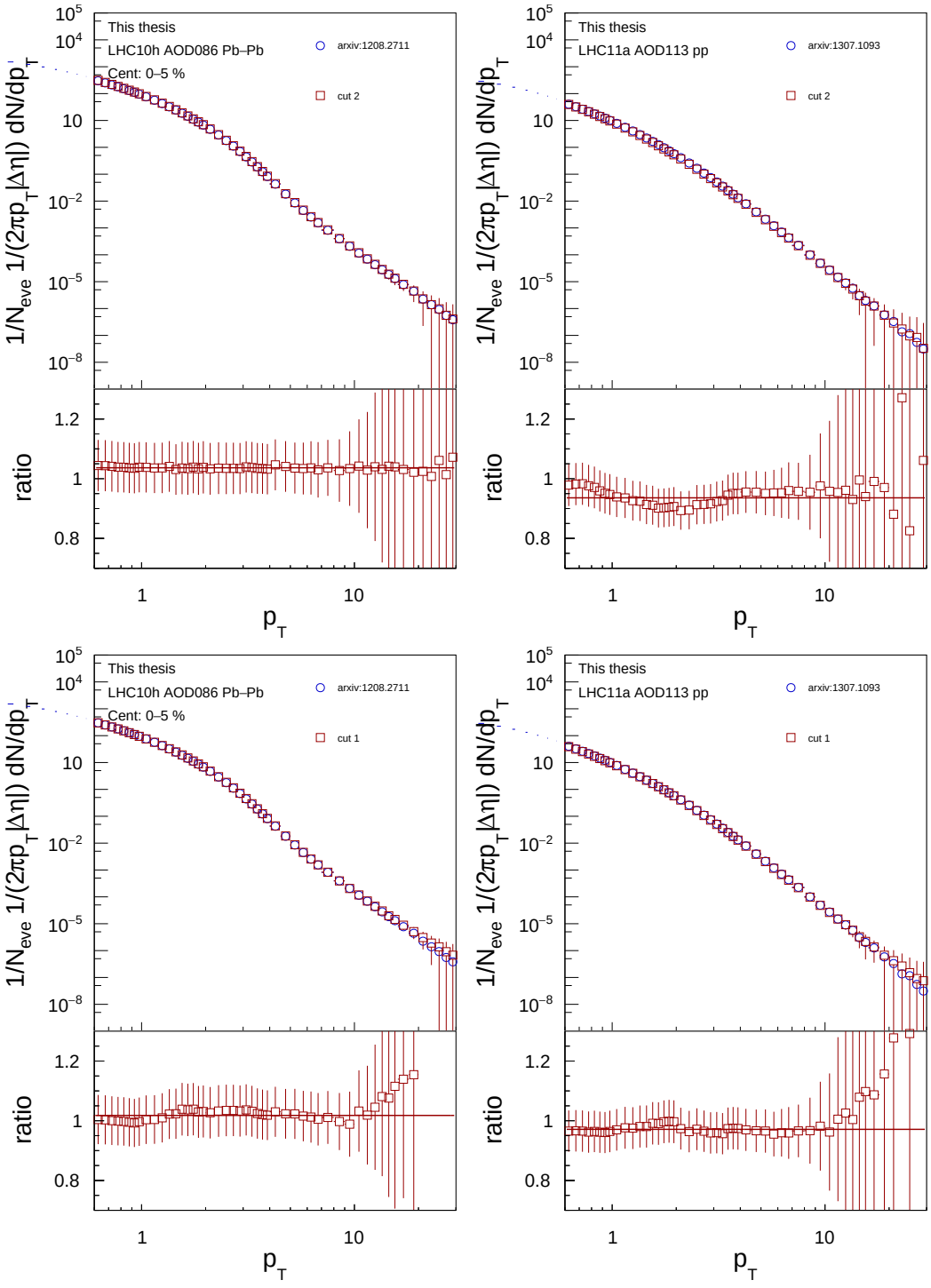

FIGURE 39 The obtained p_{T} spectra compared to the published result, bottom panel shows this analysis divided by the published result. The left figure shows the most central (0–5% centrality) Pb–Pb result, the right is pp. Top raw is with the matching cut 2, bottom shows results with the default cut 1.

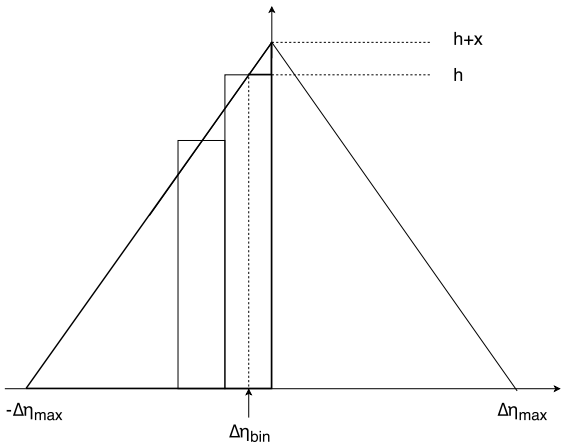

FIGURE 40 Normalization correction of the mixed event on the finite bin size.

final observable is mostly limited by the raw spectra, as was shown in Figure 37, the final error still benefits from merging the p_{Tt}>6 GeV/c and p_{Ta}>4 GeV/c bins of the mixed event. In these high-p_{T} bins it is not possible to just create more mixed event pairs, as we quickly reach the combinatorial limit of the few events available.

10.3 Track merging cut

In this subsection an estimation is given for the merged or split tracks. If two tracks are too close to each other, the detector can measure it as one track, so in this case we lose statistics. The opposite is also possible, e.g. a track hitting the boundary of two sectors at a given detector can fire a signal in both, thus resulting in two identified tracks. To correct for these effects, knowing the magnetic field, we can calculate the trajectory of the particles back to the vertex. We denote the azimuthal angle difference along this path with $\Delta\varphi^*$. Then we remove tracks if both their $\Delta\eta$ and $\Delta\varphi^*$ are smaller than 0.02 along the whole TPC volume. Although these are reconstructed tracks, e.g. by definition not merged or split, we apply this cut both in real and mixed event, thus correcting for the track pairs that were rejected. This correction was found negligible (see examples of the Pb–Pb correlation function in Figure 41), so the primary analysis does not use this correction.

10.4 Resonance cut

Resonance decays, such as e.g. $K^0 \rightarrow \pi\pi$ can distort the correlation, their decay products do not originate from the vertex, where all other particles come from.

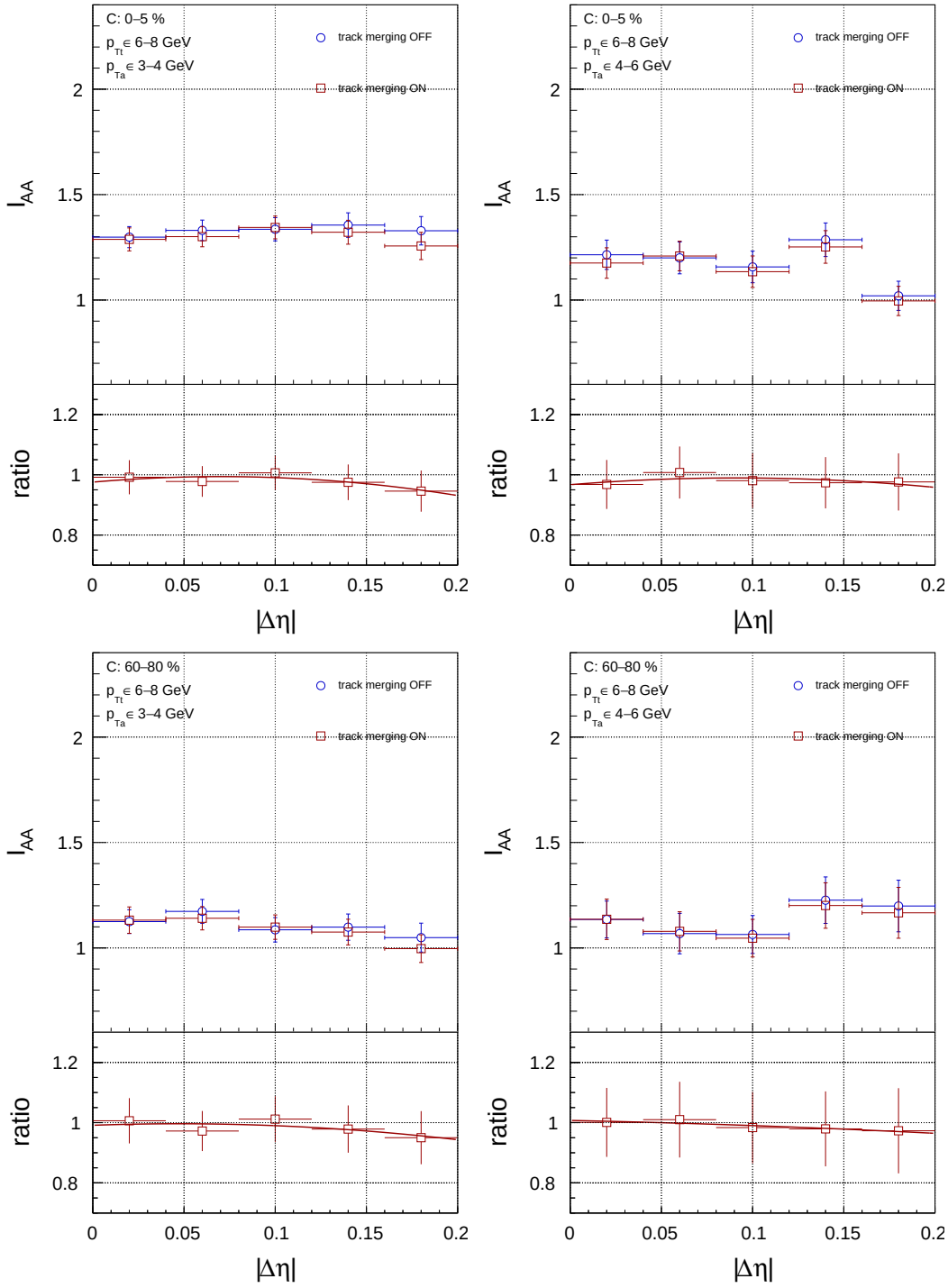

FIGURE 41 Effect of the cut on merged tracks on the per-trigger yields. The first row shows $\Delta\eta$ correlation for the central Pb–Pb (0–5%), the second shows the results for the peripheral (60–80%) centrality bin.

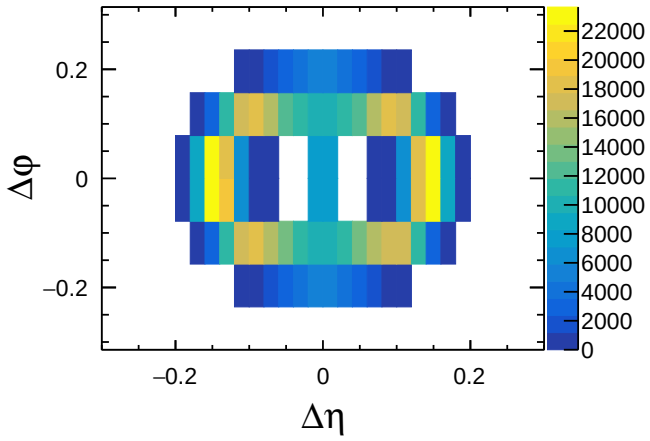

FIGURE 42 The excluded part from the correlation function by the resonance cut. A similar cut is made in the mixed event, so this correction does not distort the shape of the correlation peak (even though this cut is in the range of the peak).

Calculating azimuthal and pseudorapidity differences from these tracks thus contaminate the data sample.

During the track selection tracks that have a secondary vertex are rejected. This condition eliminates most of the tracks of resonances. Particles with a very short lifetime, however, can still contaminate the sample, so here a secondary, higher level correction is imposed. The particles are not identified, so to cut on certain particles, we have to make assumptions. Conversion electrons (defined as two tracks with opposite charge and their mass being lower than 0.04 GeV), $K^0 \rightarrow \pi\pi$ and $\Lambda^0 \rightarrow p^+\pi^-$ particles are the most abundant contaminators, so in each track-pair, we calculate the pair's invariant mass assuming the corresponding rest mass (so electrons, pions, and proton-pion). If the reconstructed mass is close, meaning closer than 0.02 GeV to the assumed particles' literature value, that track pair is rejected. These rejected tracks are collected and shown in the ($\Delta\eta$, $\Delta\varphi$)-plane in Figure 42. Similarly to the method in the track merging correction, here we also apply the same resonance cut on the mixed event. The effect of this cut on the final observable, as can be seen in Figure 43, is negligible.

10.5 Validation of the analysis using Monte Carlo closure test

The Monte Carlo closure test is a common technique in high-energy physics to validate the corrections applied to the data. During this procedure we do not analyze data but two sets of Monte Carlo productions, one which has the "true", particle-level information, and another, in which all particles are propagated through the simulated ALICE detector using the GEANT framework [170, 171, 172]. In

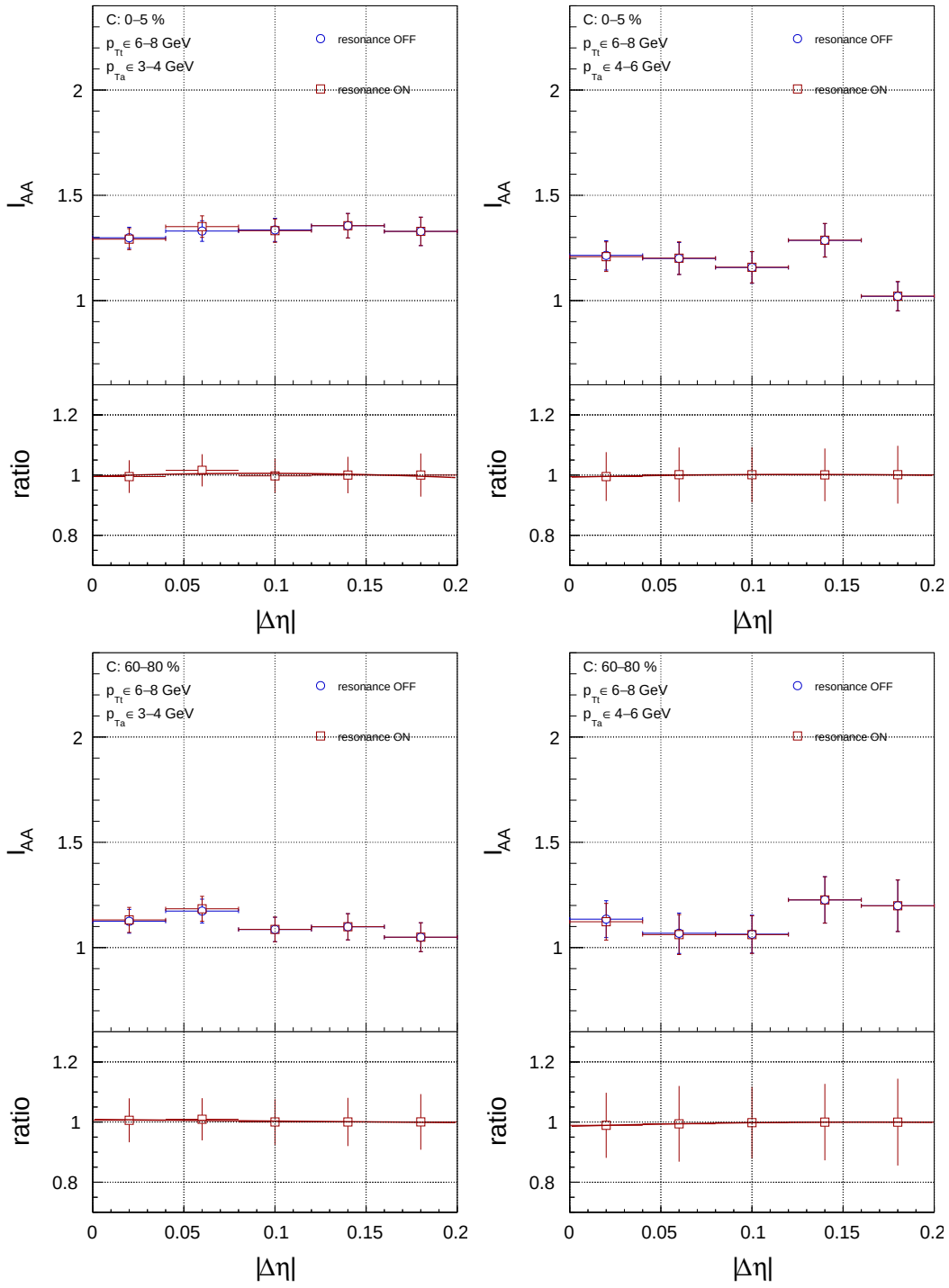

FIGURE 43 The effect of the resonance cut in the I_{AA} signal. Upper panels show the default configuration for I_{AA} with no resonance correction (blue circles) and the I_{AA} that was corrected for the effect of the long-living resonances (red squares). The lower panels show the ratios of the ON and OFF configurations. Figures in the top row show the most central results (0–5% centrality), in the bottom row the most peripheral ones (60–80% centrality) are plotted. Results are with $6<p_{\mathrm{Tt}}<8$ GeV/c, and with $3<p_{\mathrm{Ta}}<4$ GeV/c (left) and with $4<p_{\mathrm{Ta}}<6$ GeV/c (right).

this simulation the tracks are reconstructed from simulated response just as if they would be real measured detector signals, and particles can be also absorbed in the detector material. Conversion, secondaries, etc. are all simulated with this framework. One can then apply all the corrections described in chapter 10 to the detector-level simulation, and compare it to the particle-level result. The difference between the results from these two methods should naturally be as small as possible. The difference in I_{AA} between the two methods is smaller than 5%, as demonstrated in Figure 44. As most of the disagreement can be accounted for the limited statistics of these MC dataset, the corrections and the method applied in this analysis can then be considered validated.

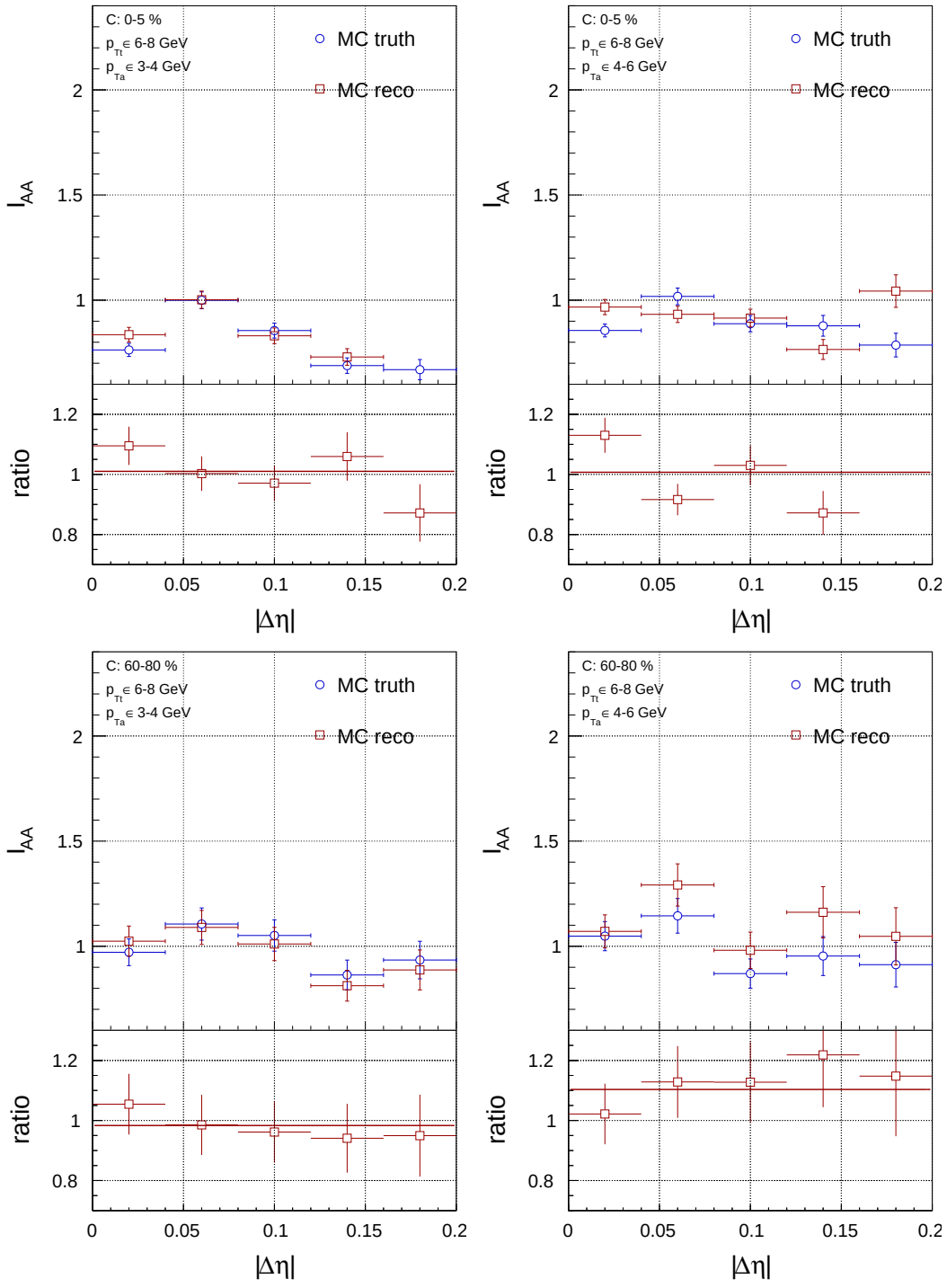

FIGURE 44 The Monte Carlo closure test. On the upper panels, the I_{AA} results from a detector-level Monte Carlo simulation (red squares) are compared to the I_{AA} from a particle-level Monte Carlo (blue circles). Lower panels show the ratios of the particle-level and the detector-level I_{AA} results. Figures in the top row show the most central results (0–5% centrality), in the bottom row the most peripheral ones (60–80% centrality) are plotted. Results are with $6<p_{\mathrm{Tt}}<8$ GeV/c, and with $3<p_{\mathrm{Ta}}<4$ GeV/c (left) and with $4<p_{\mathrm{Ta}}<6$ GeV/c (right).

11 SYSTEMATIC UNCERTAINTIES

The different sources of systematic uncertainties and their estimated values are listed in Table 3. The most dominant source of systematic error is the choice of the track cut, but numerous possible sources were examined. Each of the systematic uncertainties is detailed in a separate subsection below. The final uncertainty is obtained by summing individual components in quadrature, i.e. we assume that the uncertainties are independent. And according to [173], if the calculated systematic error is around a few percent, it is not added to the final systematic error, but will be neglected instead. The main justification for this is to not accumulate statistical errors into the systematic error. These special, neglected cases will be concluded at the end of each subsection.

We distinguish two different type of systematic errors. One, which varies point-by-point, these will be represented with boxes around each data point in the final results, and another, which scales all the data points. The latter one will be plotted with a band around unity (as I_{AA}=1 means no modification).

While determining the systematic errors, two or more data sets are compared, and the first is always with the default value used for the extraction of the final results. Then their ratio is calculated, which will be fitted with a polynomial, usually a zero-degree polynomial, but it can go up to second degree. The systematic error (even point-by-point errors) are then estimated with this fit, to avoid again including statistical fluctuations into the systematic errors.

11.1 Track cut variation

The default track cuts of this analysis (cut 1) have a uniform φ-dependence, but some fakes. The other set of cuts are not as suitable for this analysis due to holes in the φ-acceptance, but they have better momentum resolution and less fake tracks. Results presented in Figure 45 show that the shape of the final I_{AA} distribution

source	description	uncert.	type
track cut	cut 1 (default), cut 2	$< 6\%$	SC
$\Delta\varphi$ proj. range	$\lvert\Delta\varphi\rvert<0.2\pi$, 0.15π, 0.25π	$\approx 1\%$	SC
vertex cut	changing the vertex cut only for Pb–Pb: from $\lvert v_z\rvert<10$ cm to 8 cm	$\approx 1\%$	SC
fit choice	estimating the subtracted background with Generalized Gaussian or Gaussian	$< 5\%$	PbP
fit range for $\Delta\eta$	$r_{\Delta\eta}$ = (0–1.6) is default, (0–1.5), (0–1.4)	$\approx 1\%$	SC

TABLE 3 Sources of systematic errors, each will be detailed in separate subsections. We distinguish two types of errors, one is a "scaling error" (SC), which scales all points, and that will be plotted as a band around 1. The other type contains "point-by-point" (PbP) errors. These are marked in the last column of the table.

does not change significantly but cut 2 gives systematically to 4–7% higher values for the I_{AA}. This error is propagated to the final result as a scaling error.

11.2 Vertex range

The vertex distribution along the beam-axis (v_z) has a Gaussian shape, and it is not clear from first principles how much of it should be included in the analysis. The mixed event correction is performed in 2 cm vertex ranges in Pb–Pb (5 cm in pp), because the different z-vertex ranges correspond to different acceptance of the detector and hence they affect the shape of the mixed event, at least in principle. Here we compare the default Pb–Pb range of $|v_z| < 10$ cm with a tighter cut, $|v_z| < 8$ cm. The pp data was not changed, as it had 5 cm-wide binning, thus applying a tighter cut would have resulted in a significant change in the statistics, and would have disturbed the evaluation of the systematic difference. The effect of the Pb–Pb vertex cut on the I_{AA} signal is shown in Figure 46, and its effect is negligible.

11.3 The $\Delta\varphi$ projection range

The default $\Delta\varphi$ projection range is 0.2π, which is determined by the width of the jet-peak in $\Delta\varphi$. Using the whole near side (0.5π), for example, would reduce the signal over background ratio as more background would be included, and no signal. So while evaluating this systematic error source, this default value

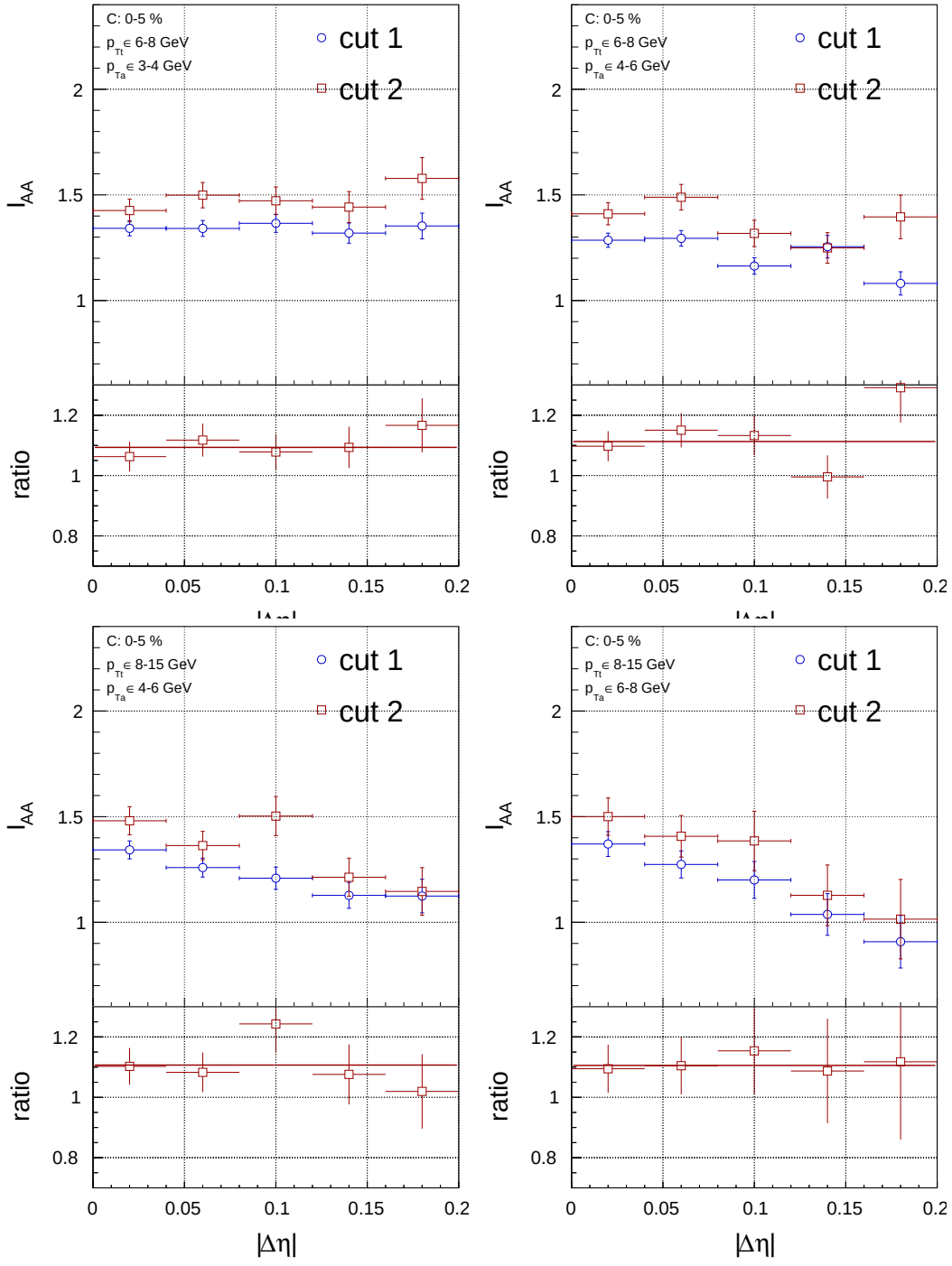

FIGURE 45 Track cut dependence of the I_{AA} signal with the most central Pb–Pb (0–5%) results.

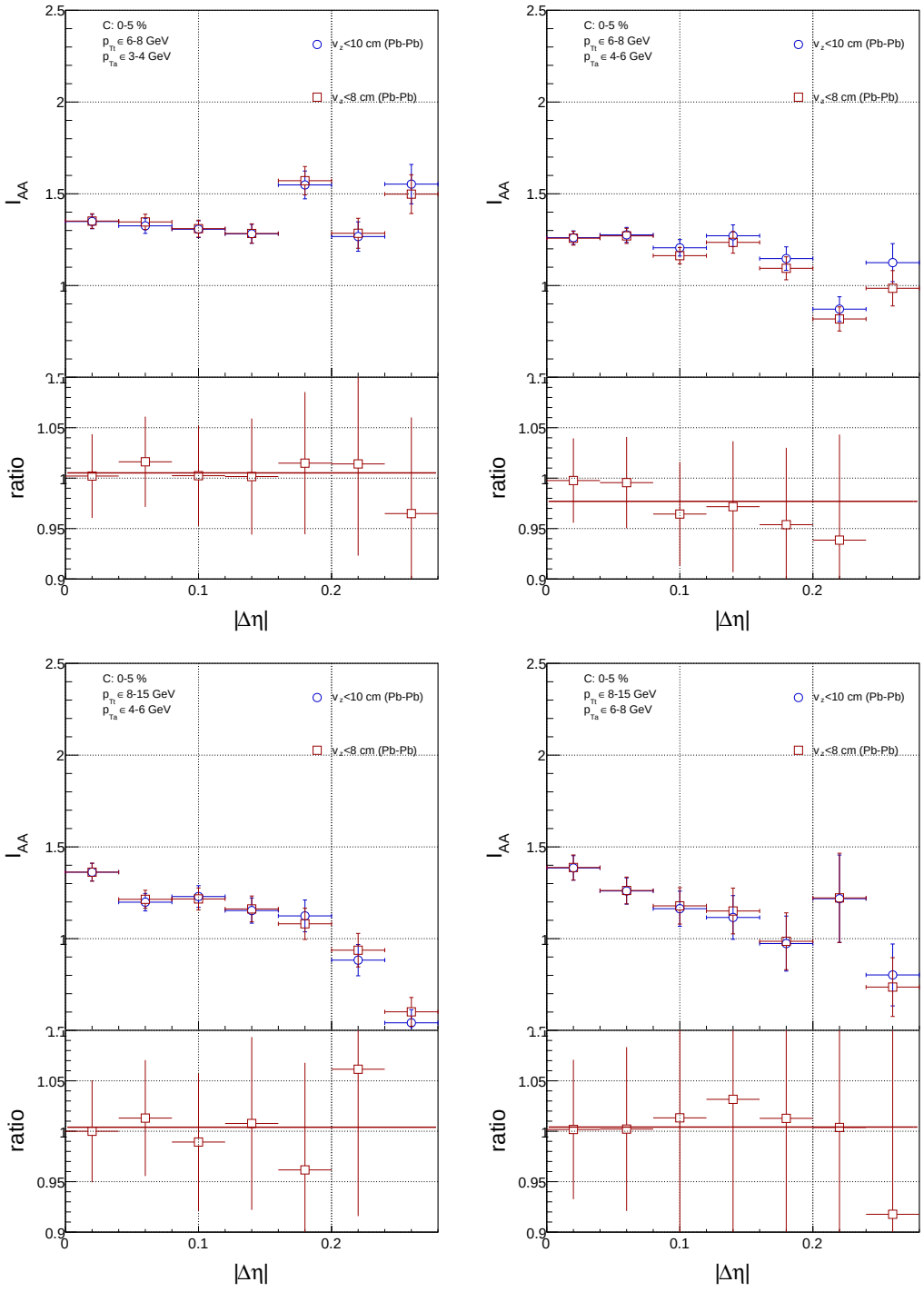

FIGURE 46 Vertex dependence of the I_{AA} signal with the most central Pb–Pb (0–5%) results. The effect is random and around (1-2)%, thus will be neglected.

was changed to 0.15π, and 0.25π. They are plotted together in Figure 47. The dependence on the $\Delta\varphi$ projection range is small (around a few percent), and does not introduce a trend, thus will be neglected.

11.4 Dependence on the fit

Both the effect of the fit choice and the fit range is investigated here. Since the fit is not used for yield extraction, only to determine the background to be subtracted, only 2 fits were tried, the Gaussian and the Generalized Gaussian distributions. The effect is quite strong for the correlation function, but most of it cancels for the final I_{AA} (Figure 48). Still, as the ratio can be described by a second-degree polynomial, a point-by-point systematic error will be assigned.

The dependence on the fit range was also examined, from the original full range in $\Delta\eta$ (0–1.6) to upper values of 1.5 and 1.4, down to 1.2, to investigate the effect of the statistical fluctuations at large $\Delta\eta$. The dependence of the range is below 1%, and will be neglected for both fit functions (the Gaussian and the Generalized Gaussian). Figure 49 shows its effect on the I_{AA}, with the default Generalized Gaussian fit.

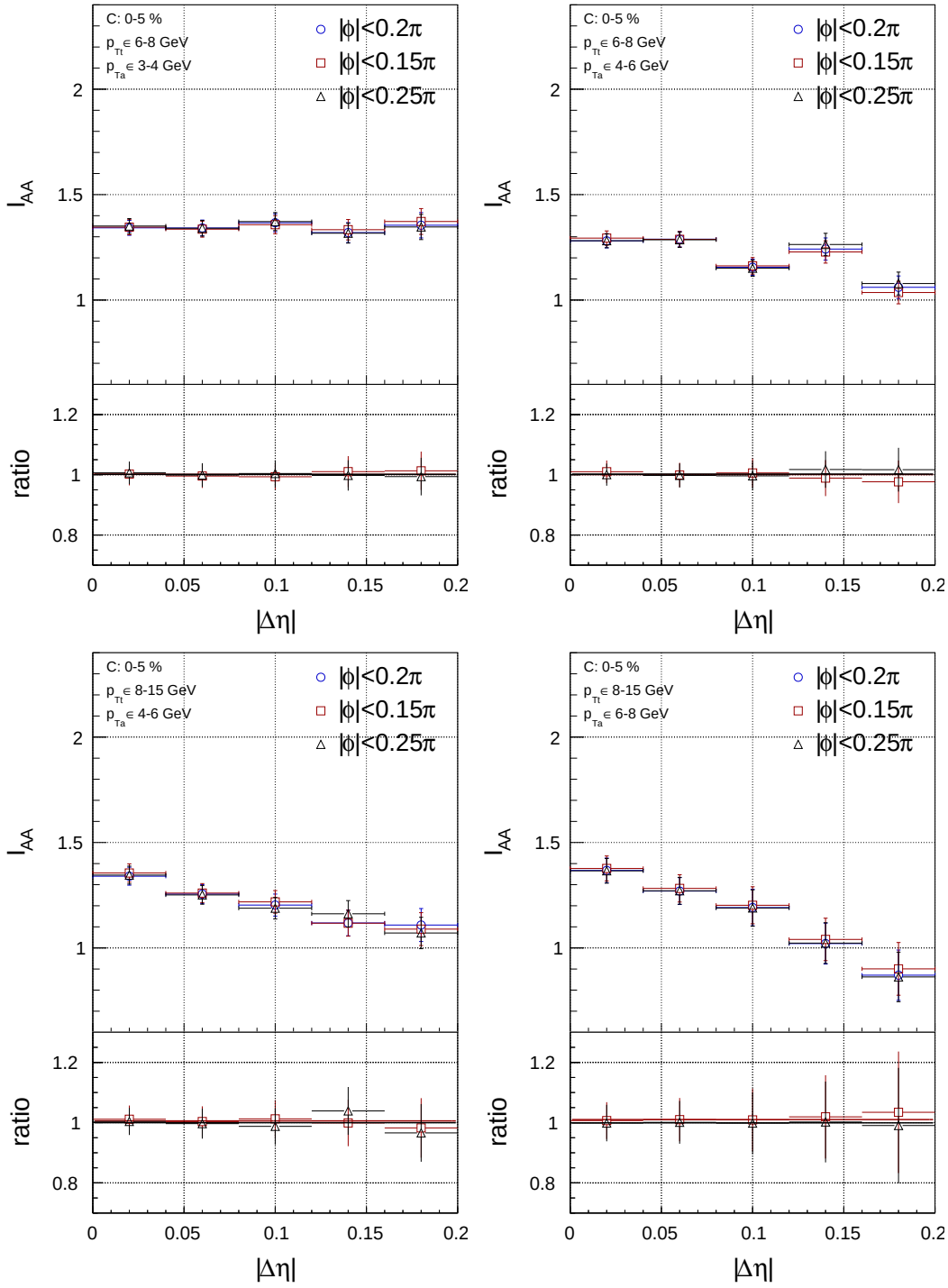

FIGURE 47 The $\Delta\varphi$ cut dependence of the I_{AA} signal with the most central Pb–Pb (0–5%) results. $\Delta\varphi/\pi$ = 0.15, 0.2 (default), and 0.25 were tried. The effect is random and around (1-2)%, thus will be neglected.

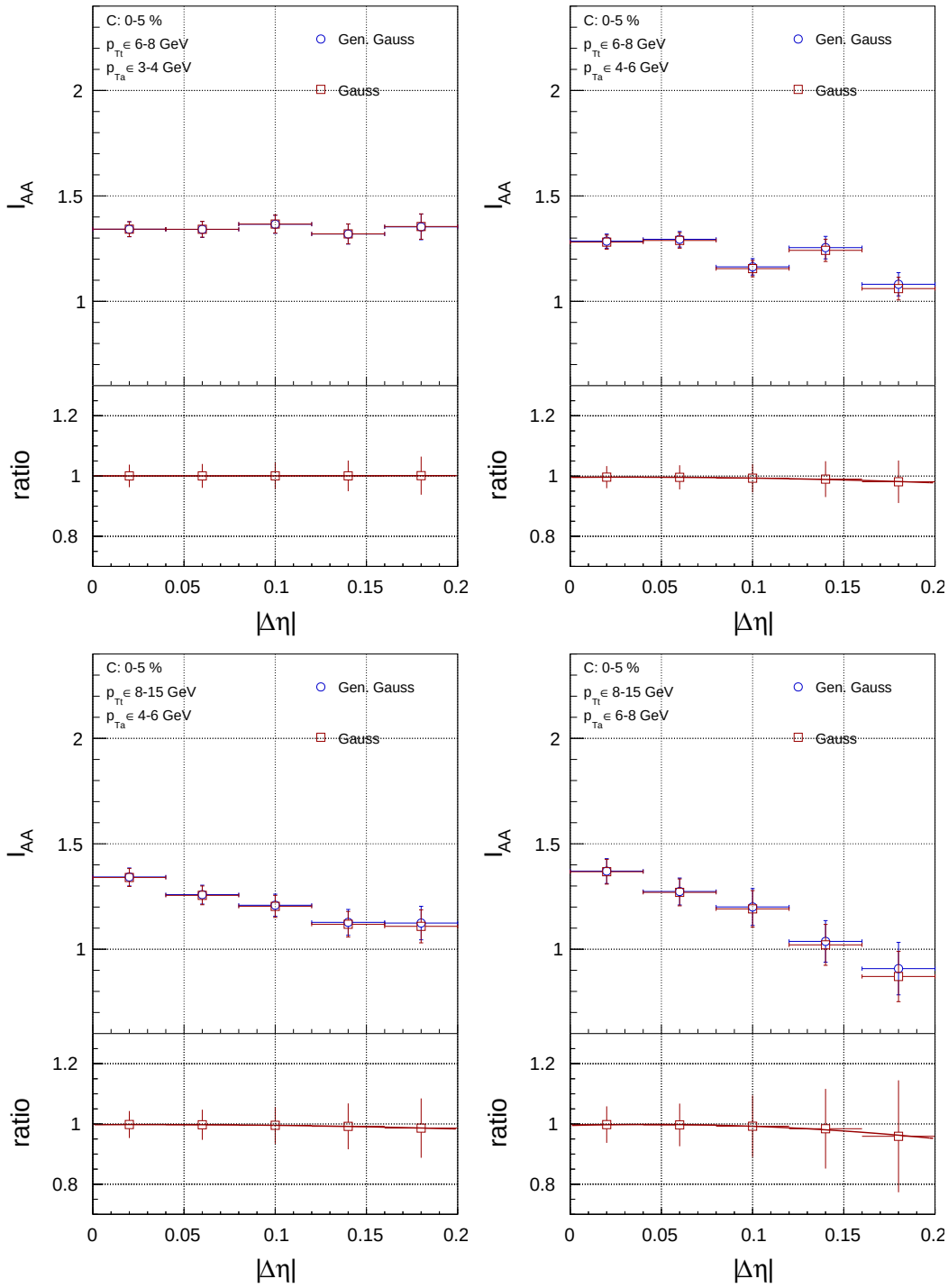

FIGURE 48 The dependence on the fit choice used for background subtraction (the default Generalized Gaussian and the Gaussian function are compared). Change with respect to the primary analysis happens within the quoted statistical error bars, but a point-by-point systematic error will be assigned from this.

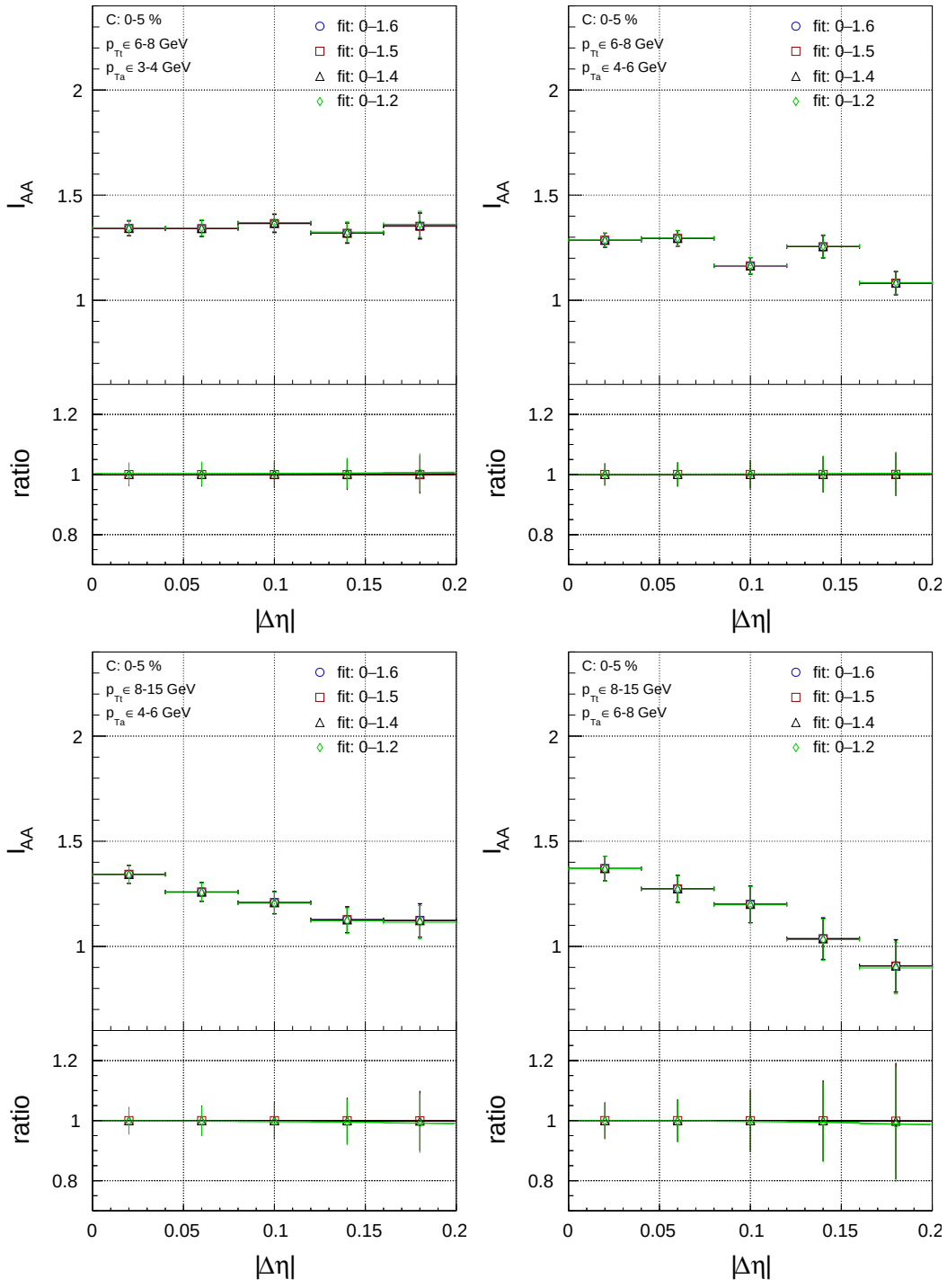

FIGURE 49 The dependence on the fit range, deviation from default (0–1.6) using ranges (0–1.5), (0–1.4) and (0–1.2) obtained with the default Generalized Gaussian fit. The results show insensitivity to the statistical fluctuations at large $\Delta\eta$. Similar results were obtained with the Gaussian fit as well.

12 RESULTS AND CONCLUSIONS

In this section the final results, the I_{AA} quantity both as a function of p_{Ta} and $|\Delta\eta|$ are presented. In Figure 50 the $I_{\mathrm{AA}}(p_{\mathrm{Ta}})$ is compared with two published ALICE results, the first ALICE publication of I_{AA} [166] (with PRL in the legend), and a more recent one, where the trigger was an identified π^0 meson [160]. Both published results are obtained from the $\Delta\varphi$ projection of the correlation function. The results match within their uncertainties.

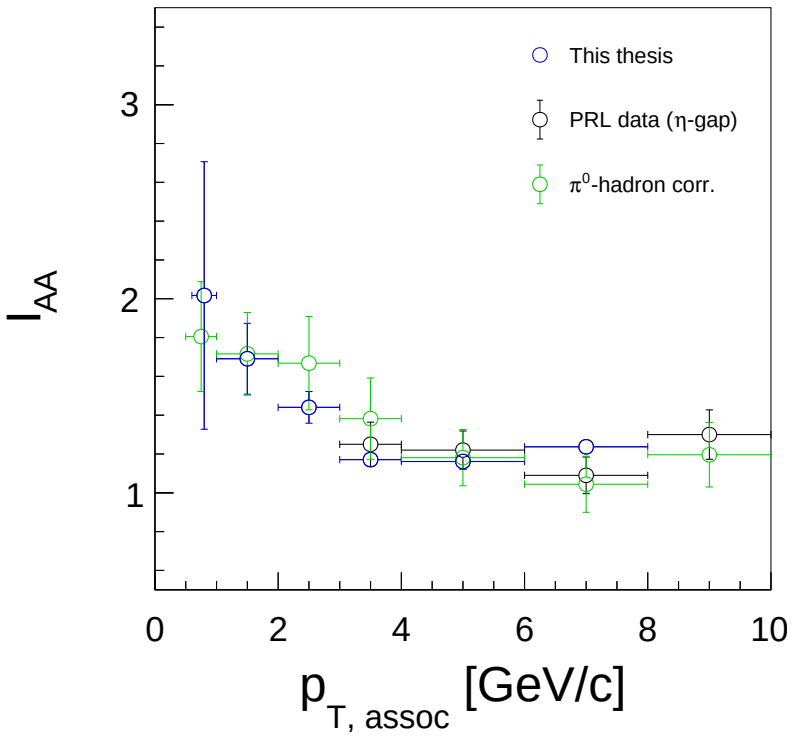

FIGURE 50 I_{AA} extracted with the Generalized Gaussian fit (defined in Equation 27), compared to both ALICE results of [166] and [160]. Note the different projection, the published one is extracted from $\Delta\varphi$ correlation while current results are from $\Delta\eta$.

The final results, the $\Delta\eta$-dependent I_{AA} measurements characterizing the jet shape modification, are presented in three centrality classes. The I_{AA} calculated with the most central (0–5%) Pb–Pb collisions is shown in Figure 51, the mid-central (20–40%) in Figure 52, and the most peripheral (60–80%) results are shown in Figure 53. In each figure, point-by-point systematic errors are drawn with boxes around the data points, while the scaling error appears as a band around one.

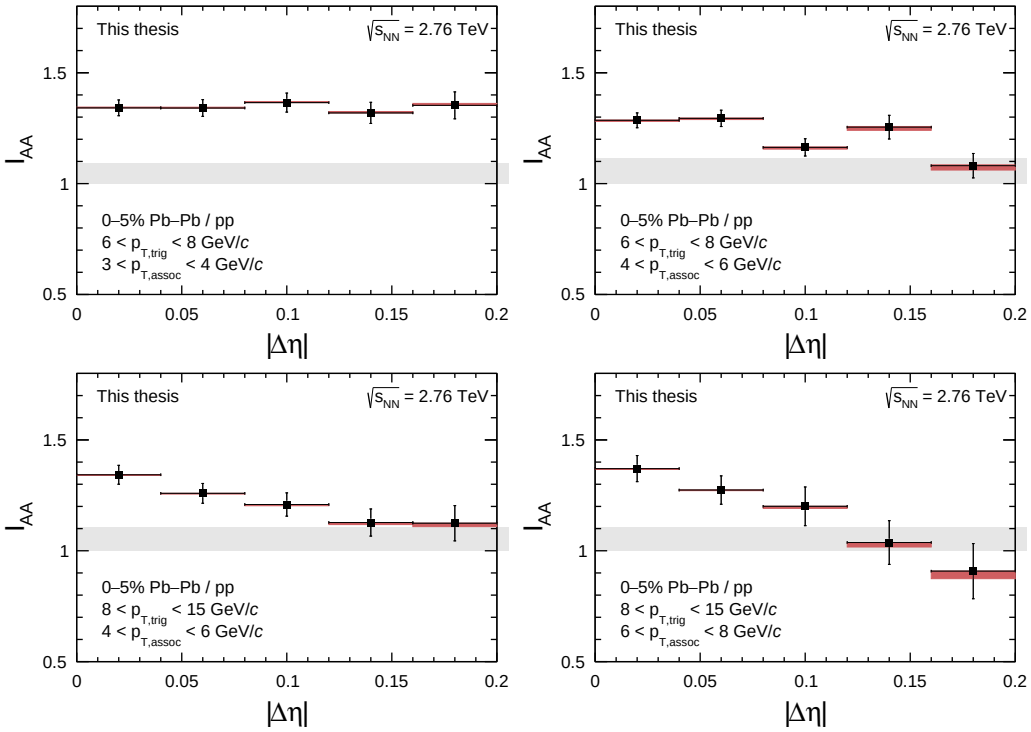

FIGURE 51 The final I_{AA} with its systematic errors (detailed in Table 3) with the most central Pb–Pb (0–5%). The band around one marks the scaling systematic error.

A clear hint of narrowing is observed in the most central Pb–Pb collisions with the $8<p_{\mathrm{Tt}}<15$ GeV/c trigger, in both associated p_{T} bins ($4<p_{\mathrm{Ta}}<6$ GeV/c and $6<p_{\mathrm{Ta}}<8$ GeV/c). In lower trigger and associated p_{T} combinations (e.g. with $6<p_{\mathrm{Tt}}<8$ GeV/c and $3<p_{\mathrm{Ta}}<4$ GeV/c and $4<p_{\mathrm{Ta}}<6$ GeV/c), we observe no effect, neither narrowing or broadening. The peripheral result (Figure 53) is expected to have no modification, and it is indeed consistent with one within the uncertainties. The mid-central result is expected to be an interpolation between the two ends, the most peripheral and most central, and in accordance with that, Figure 52 shows only a very weak hint of narrowing. Also note that no broadening is observed in any of these p_{T} windows.

The phenomena behind the narrowing could be a kinematical bias, meaning that a jet that can traverse the medium would have had high original momentum. The soft emission during the energy loss would be absorbed as a part

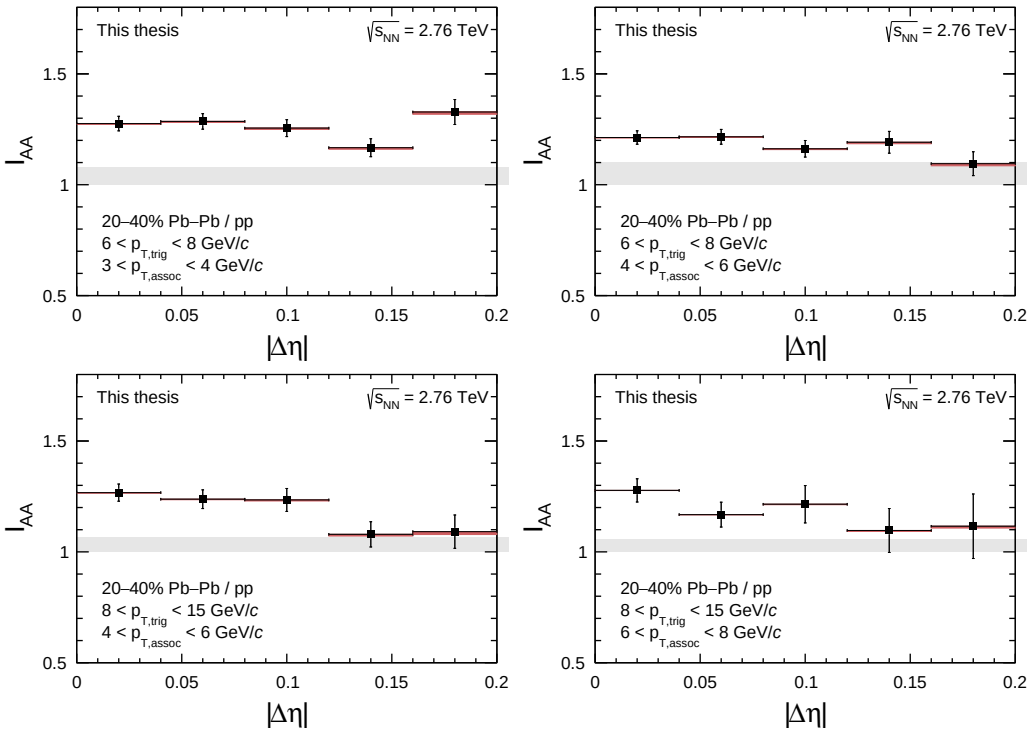

FIGURE 52 The final I_{AA} with its systematic errors (detailed in Table 3) with (20–40%) centrality Pb–Pb. The band around one marks the scaling systematic error.

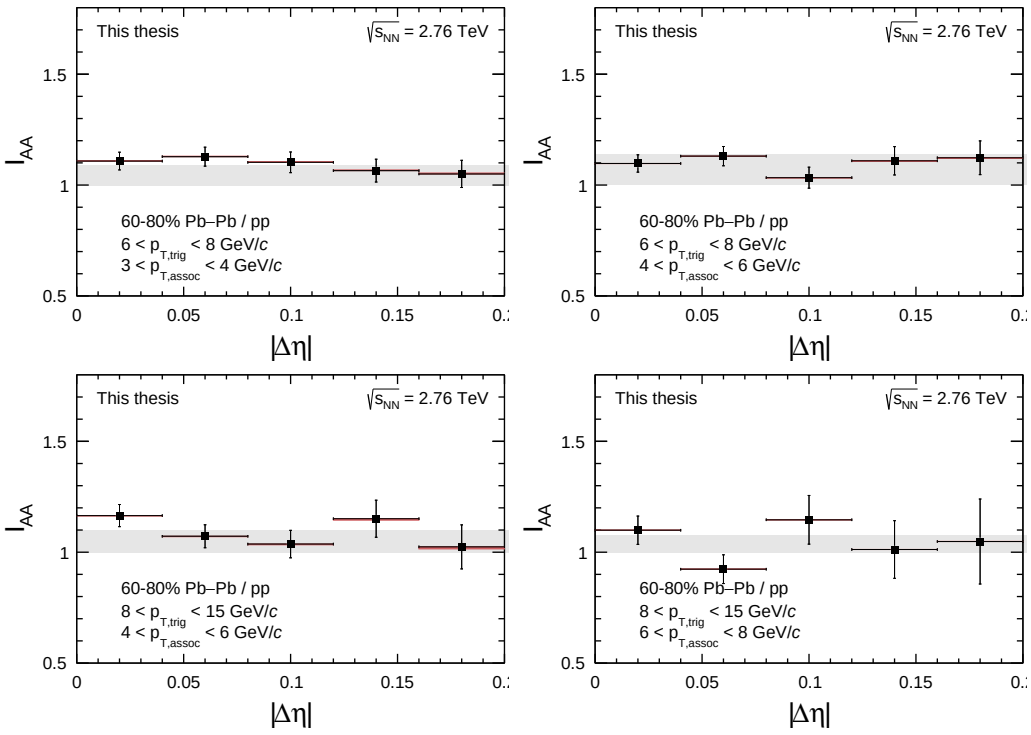

FIGURE 53 The final I_{AA} with its systematic errors (detailed in Table 3) with peripheral (60–80%) Pb–Pb. The band around one marks the scaling systematic error.

of the medium and removed together with the background. Only the hard core of the jet makes the punch trough and appears more collimated at the final state. This should be captured by the AMPT simulation, where interaction of the jets and the medium is taken into account. In order to investigate this, the Pb–Pb events simulated with AMPT [73, 74] were compared to a PYTHIA simulation (with softQCD settings) [174] of the pp data. The softQCD settings was chosen as that reproduces best the data[1]. In the AMPT case, the hadronization was set[2] to the "string melting" option [175] instead of the Lund string fragmentation model, because it takes into account the effects of flow in the overlap volume of the colliding nuclei. The resulting I_{AA} shown in Figure 54 exhibits either a flat trend or a broadening. The assumption that the narrowing is only from kinematical collimation might then be ruled out. AMPT overestimates the radiation in the peak area, but the effect of broadening in such high p_{T} is not fully understood.

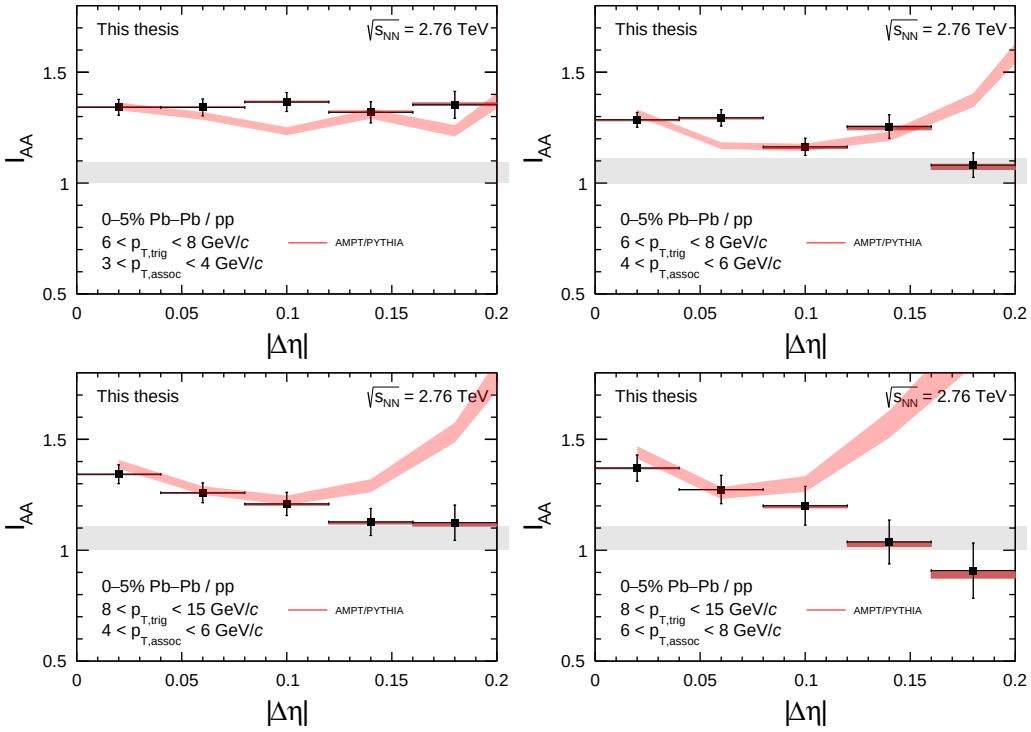

FIGURE 54 The final I_{AA} with its systematic errors (detailed in Table 3) with the most central Pb–Pb (0–5%) compared to MC simulation. Pb–Pb events were simulated with AMPT [73, 74] while the pp events were simulated with PYTHIA [174]. Their ratio is shown with a red band. The gray band around one marks the scaling systematic error like in the previous figures.

Other explanation might be related to gluon filtering: as there is a color charge dependence of the jet suppression due to the Casimir scaling, and also gluons are expected to fragment losing more momenta, one expects a smaller

[1] See http://mcplots.cern.ch for details.

[2] This setting corresponds to the ALICE MC *AMPT_LHC13f3a*.

fraction of gluon jets in the high-p_{T} regime. This abundance of quark jets (gluon filtering) in high p_{T} can then lead to the narrowing of the correlation peak, since quark jets are narrower than gluon jets (see Equation 16 and Ref. [58]). To test this idea, a custom Monte Carlo study was performed in the same kinematical region ($8<p_{\mathrm{Tt}}<15$ GeV/c and $4<p_{\mathrm{Ta}}<6$ GeV/c). PYTHIA allows for a parton-level treatment, thus one can directly select quarks and gluons, and build-up I_{AA} only from particles radiated by a quark or a gluon, separately. The medium is not simulated, we take ratios of the tagged jets in pp and the no pre-selection scenario. The results are shown in Figure 55, and show that the narrowing observed in the data is consistent with a gluon filtering scenario. A similar conclusion was reached in Ref. [176] where it was found that "the modification of the fragmentation function $D(z)$ (excluding the enhancement at low-z), may result from the different quenching of the quarks and the gluons."

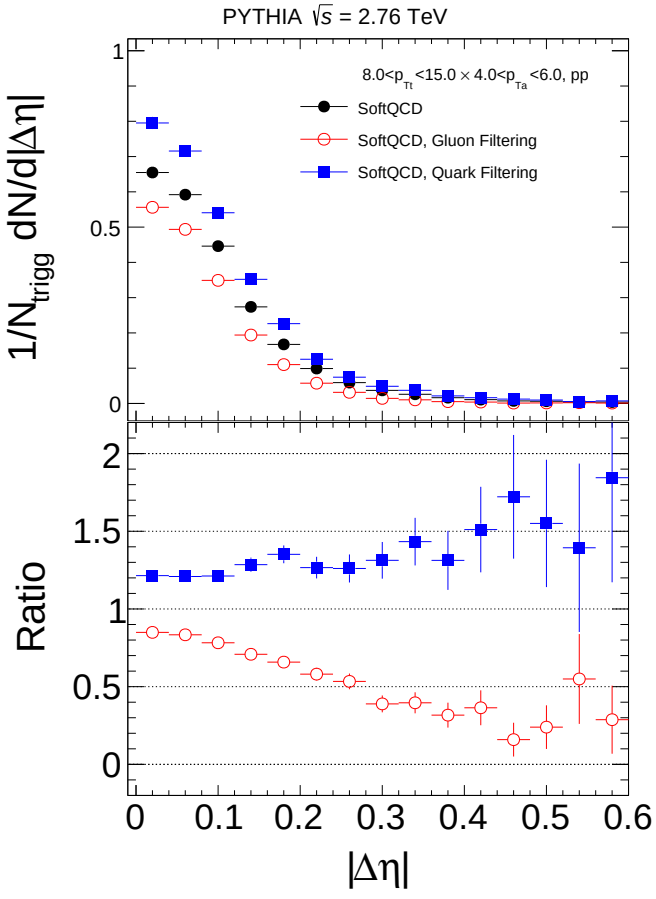

FIGURE 55 PYTHIA simulation to test the effect of a quark or gluon filtering scenario in pp collision. The lower plot shows the ration of the quark or gluon filtered events and the no filter case [177].

The narrowing result presented in this thesis is in accordance with other results. ATLAS also reported on centrality-dependent modification of the fragmen-

tation functions with $100 < p_{\mathrm{T}}^{\mathrm{jet}} < 387$ GeV/c jets at the same collision energy [153], and CMS observed a similar trend [142].

The results obtained by the two-particle correlations method, although in azimuth angle [166, 160] were already compared in Figure 50. This integrated, p_{Ta}-dependent I_{AA} result shows good agreement between the various methods. The jet reconstruction in higher p_{T} ($40 < p_{\mathrm{T}}^{\mathrm{jet}} < 60$ GeV/c), arrives at a similar result [157], where they conclude that "in-medium fragmentation is harder and more collimated than vacuum fragmentation". Their measurements of the angularity (g) of the jets and the momentum dispersion ($p_{\mathrm{T}}D$) were performed with $\sqrt{s}$ = 7 TeV pp and $\sqrt{s_{\mathrm{NN}}}$ = 2.76 TeV Pb–Pb collisions. The jet angularity showed a similar narrowing, and the $p_{\mathrm{T}}D$ indicated that the increase of the quark fraction scenario describes the data better than the kinematical collimation [157]. The result of this thesis also continues the trend shown in Ref. [159], which reported on low-p_{T} broadening below $4 < p_{\mathrm{Tt}} < 8$ GeV/c and no modification in that window. The analysis of this thesis focuses on higher p_{T} and shows that beyond that range the narrowing scenario is more consistent with the data. The measurement presented in this thesis can then be thought of as the narrowing measured at the lowest p_{T}.

SUMMARY

This thesis reports on work performed in two different domains. One is detector-related, and it has grown out from the service task, and the other is the study of the jet shape modification in Pb–Pb collisions, an analysis of the ALICE data. The detector work was described in Part II. It consisted of the Quality Assurance of the GEM foils (chapter 5, thesis point 1), and the correlation study between the hole diameters and the gain of the foils (Part II, thesis point 2). My work in the Quality Assurance was to develop the analysis software which displayed the results of the measurement with a graphical interface [1] and to analyze the data with that. For the correlation study I also developed the analysis software, and the framework in which the comparison of the gain and the optical measurement can be compared. The conclusion from the study is that one can predict the gain from solely the optical parameters of the foil (e.g. knowledge of the bottom, middle and top diameter of the holes) with 10% accuracy. This precision is enough to be able to classify the foils after their production. For the actual experiment, of course, further calibration, and test beam measurements are required. The jet shape analysis (Part III, thesis point 3) reported on narrowing of the jets with trigger momentum $8<p_{\mathrm{Tt}}<15$ GeV/c and associated momenta $4<p_{\mathrm{Ta}}<6$ GeV/c and $6<p_{\mathrm{Ta}}<8$ GeV/c, in the most central Pb–Pb collisions (0–5 %) at $\sqrt{s_{\mathrm{NN}}}$ = 2.76 TeV. The narrowing is defined as compared to a pp reference with the same center of mass energy. The analysis relied on the two-particle correlations method instead of the jet reconstruction algorithms because of the low momentum-range of the analysis, where the reconstruction algorithms are not expected to work. To understand the origin of the narrowing, two Monte Carlo studies were performed. First the I_{AA} results were compared to AMPT (Pb–Pb) and PYTHIA (pp) simulations to rule out trivial kinematical biases, like the bias stemming from the fact that the original jet had a larger p_{T} in the heavy-ion environment. As the AMPT data was consistent with either no modification or a broadening scenario (see Figure 54), the source of the narrowing should then be searched elsewhere. The other Monte Carlo simulation tests the assumption of the gluon filtering, the phenomenon that in higher momenta the narrower quark jets tend to dominate the sample, due to the color charge dependence of the jet suppression. To test whether this phenomenon could in fact cause a measurable effect, a PYTHIA study was performed in the same kinematical region. The parton level treatment allows us to select by hand the quark and gluon initiated jets. Only pp collisions were simulated and the pure samples were compared to the case of no pre-selection at all. The results (see Figure 55 show that the narrowing is consistent with the gluon filtering scenario. The results also agree with an independent measurement performed with fully reconstructed jets [157].

REFERENCES

[1] Márton Vargyas, "TPCQA," *Github repository* , https://github.com/vargyas/tpcqa.

[2] **CMS** Collaboration, V. Khachatryan *et al.*, "Observation of Long-Range Near-Side Angular Correlations in Proton-Proton Collisions at the LHC," *JHEP* **09** (2010) 091, arXiv:1009.4122 [hep-ex].

[3] J. I. Friedman and H. W. Kendall, "Deep Inelastic Electron Scattering," *Annual Review of Nuclear Science* **22** no. 1, (1972) 203–254. https://doi.org/10.1146/annurev.ns.22.120172.001223.

[4] Y. Aoki, Z. Fodor, S. D. Katz, and K. K. Szabo, "The QCD transition temperature: Results with physical masses in the continuum limit," *Phys. Lett.* **B643** (2006) 46–54, arXiv:hep-lat/0609068 [hep-lat].

[5] S. Borsanyi, G. Endrodi, Z. Fodor, A. Jakovac, S. D. Katz, S. Krieg, C. Ratti, and K. K. Szabo, "The QCD equation of state with dynamical quarks," *JHEP* **11** (2010) 077, arXiv:1007.2580 [hep-lat].

[6] A. Bazavov *et al.*, "The chiral and deconfinement aspects of the QCD transition," *Phys. Rev.* **D85** (2012) 054503, arXiv:1111.1710 [hep-lat].

[7] J. D. Björken, "Highly relativistic nucleus-nucleus collisions: The central rapidity region," *Phys. Rev. D* **27** (Jan, 1983) 140–151. https://link.aps.org/doi/10.1103/PhysRevD.27.140.

[8] **ALICE** Collaboration, J. Adam *et al.*, "Measurement of transverse energy at midrapidity in Pb-Pb collisions at $\sqrt{s_{\mathrm{NN}}} = 2.76$ TeV," *Phys. Rev.* **C94** no. 3, (2016) 034903, arXiv:1603.04775 [nucl-ex].

[9] **PHENIX** Collaboration, A. Adare *et al.*, "Scaling properties of azimuthal anisotropy in Au+Au and Cu+Cu collisions at s(NN) = 200-GeV," *Phys. Rev. Lett.* **98** (2007) 162301, arXiv:nucl-ex/0608033 [nucl-ex].

[10] C.-Y. Wong, *Introduction to high-energy heavy-ion collisions*. World Scientific, Singapore, 1994. https://cds.cern.ch/record/241251. Erratum.

[11] J. Rak and M. J. Tannenbaum, *High-pT Physics in the Heavy Ion Era*. Cambridge Monographs on Particle Physics, Nuclear Physics and Cosmology. Cambridge University Press, 2013.

[12] G. Ecker, "Quantum chromodynamics," in *High-energy physics. Proceedings, European School, Kitzbuehel, Austria, August 21-September, 2005*. 2006. arXiv:hep-ph/0604165 [hep-ph].

[13] N. Doughty, *Lagrangian Interaction: An Introduction To Relativistic Symmetry In Electrodynamics And Gravitation*. Brooks/Cole Series in Educational. Westview Press, 1990.

[14] D. J. Gross, "Asymptotic freedom and the emergence of QCD," in *The Rise of the standard model: Particle physics in the 1960s and 1970s. Proceedings, Conference, Stanford, USA, June 24-27, 1992*, pp. 199–232. 1992. arXiv:hep-ph/9210207 [hep-ph].

[15] C. Patrignani and P. D. Group, "Review of Particle Physics," *Chinese Physics C* **40** no. 10, (2016) 100001. http://stacks.iop.org/1674-1137/40/i=10/a=100001.

[16] U. W. Heinz, "The Strongly coupled quark-gluon plasma created at RHIC," *J. Phys.* **A42** (2009) 214003, arXiv:0810.5529 [nucl-th].

[17] E. V. Shuryak, "Theory of Hadronic Plasma," *Sov. Phys. JETP* **47** (1978) 212–219. [Zh. Eksp. Teor. Fiz.74,408(1978)].

[18] J. C. Collins and M. J. Perry, "Superdense Matter: Neutrons or Asymptotically Free Quarks?," *Phys. Rev. Lett.* **34** (May, 1975) 1353–1356. https://link.aps.org/doi/10.1103/PhysRevLett.34.1353.

[19] N. Cabibbo and G. Parisi, "Exponential hadronic spectrum and quark liberation," *Physics Letters B* **59** no. 1, (1975) 67 – 69. http://www.sciencedirect.com/science/article/pii/0370269375901586.

[20] B. A. Freedman and L. D. McLerran, "Fermions and gauge vector mesons at finite temperature and density. III. The ground-state energy of a relativistic quark gas," *Phys. Rev. D* **16** (Aug, 1977) 1169–1185. https://link.aps.org/doi/10.1103/PhysRevD.16.1169.

[21] Björken, J. D., "Energy Loss of Energetic Partons in Quark - Gluon Plasma: Possible Extinction of High p(t) Jets in Hadron - Hadron Collisions,".

[22] M. Gazdzicki *et al.*, "Neutral strange particle production in S-S collisions at 200 GEV/nucleon," *Nuclear Physics A* **498** (1989) 375 – 383. http://www.sciencedirect.com/science/article/pii/0375947489906131.

[23] **NA44** Collaboration, I. Bearden *et al.*, "Strange meson enhancement in Pb Pb collisions," *Phys. Lett.* **B471** (1999) 6–12, arXiv:nucl-ex/9907013 [nucl-ex].

[24] E. Andersen *et al.*, "Strangeness enhancement at mid-rapidity in Pb–Pb collisions at 158 A GeV/c," *Physics Letters B* **449** no. 3, (1999) 401 – 406. http://www.sciencedirect.com/science/article/pii/S0370269399001409.

[25] **CERES** Collaboration, B. Lenkeit *et al.*, "Recent results from Pb - Au collisions at 158-GeV/c per nucleon obtained with the CERES spectrometer," *Nucl. Phys.* **A661** (1999) 23–32, arXiv:nucl-ex/9910015 [nucl-ex].

[26] M. Abreu *et al.*, "Anomalous J/Ψ suppression in Pb-Pb interactions at 158 GeV/c per nucleon," *Physics Letters B* **410** no. 2, (1997) 337 – 343. http://www.sciencedirect.com/science/article/pii/S0370269397009155.

[27] P. L. Maiani, "New State of Matter created at CERN." https://press.cern/press-releases/2000/02/new-state-matter-created-cern, 2000.

[28] Ulrich Heinz and Maurice Jacob, "Evidence for a New State of Matter: An Assessment of the Results from the CERN Lead Beam Programme." https://newstate-matter.web.cern.ch/newstate-matter/science.html.

[29] **BRAHMS** Collaboration, I. Arsene *et al.*, "Quark gluon plasma and color glass condensate at RHIC? The Perspective from the BRAHMS experiment," *Nucl. Phys.* **A757** (2005) 1–27, arXiv:nucl-ex/0410020 [nucl-ex].

[30] **PHOBOS** Collaboration, B. B. Back *et al.*, "The PHOBOS perspective on discoveries at RHIC," *Nucl. Phys.* **A757** (2005) 28–101, arXiv:nucl-ex/0410022 [nucl-ex].

[31] **PHENIX** Collaboration, K. Adcox *et al.*, "Formation of dense partonic matter in relativistic nucleus-nucleus collisions at RHIC: Experimental evaluation by the PHENIX collaboration," *Nucl. Phys.* **A757** (2005) 184–283, arXiv:nucl-ex/0410003 [nucl-ex].

[32] **STAR** Collaboration, J. Adams *et al.*, "Experimental and theoretical challenges in the search for the quark gluon plasma: The STAR Collaboration's critical assessment of the evidence from RHIC collisions," *Nucl. Phys.* **A757** (2005) 102–183, arXiv:nucl-ex/0501009 [nucl-ex].

[33] **BRAHMS** Collaboration, I. Arsene *et al.*, "Transverse momentum spectra in Au+Au and d+Au collisions at s**(1/2) = 200-GeV and the pseudorapidity dependence of high p(T) suppression," *Phys. Rev. Lett.* **91** (2003) 072305, arXiv:nucl-ex/0307003 [nucl-ex].

[34] **PHOBOS** Collaboration, B. B. Back *et al.*, "Centrality dependence of charged hadron transverse momentum spectra in d + Au collisions at S(NN)**1/2 = 200 GeV," *Phys. Rev. Lett.* **91** (2003) 072302, arXiv:nucl-ex/0306025 [nucl-ex].

[35] **PHENIX** Collaboration, S. S. Adler *et al.*, "Absence of suppression in particle production at large transverse momentum in S(NN)**(1/2) = 200-GeV d + Au collisions," *Phys. Rev. Lett.* **91** (2003) 072303, arXiv:nucl-ex/0306021 [nucl-ex].

[36] **STAR** Collaboration, J. Adams *et al.*, "Evidence from d + Au measurements for final state suppression of high p(T) hadrons in Au+Au collisions at RHIC," *Phys. Rev. Lett.* **91** (2003) 072304, arXiv:nucl-ex/0306024 [nucl-ex].

[37] **CMS** Collaboration, S. Chatrchyan *et al.*, "Study of high-pT charged particle suppression in PbPb compared to pp collisions at $\sqrt{s_{NN}} = 2.76$ TeV," *Eur. Phys. J.* **C72** (2012) 1945, arXiv:1202.2554 [nucl-ex].

[38] N. Haque, *Some Applications of Hard Thermal Loop Perturbation Theory in Quark Gluon Plasma*. PhD thesis, Saha Inst., 2014-07. arXiv:1407.2473 [hep-ph].
https://inspirehep.net/record/1305436/files/arXiv:1407.2473.pdf.

[39] R. Snellings, "Elliptic Flow: A Brief Review," *New J. Phys.* **13** (2011) 055008, arXiv:1102.3010 [nucl-ex].

[40] **ALICE** Collaboration, K. Aamodt *et al.*, "Harmonic decomposition of two-particle angular correlations in Pb-Pb collisions at $\sqrt{s_{NN}} = 2.76$ TeV," *Phys. Lett.* **B708** (2012) 249–264, arXiv:1109.2501 [nucl-ex].

[41] C. Alt *et al.*, "Directed and elliptic flow of charged pions and protons in Pb + Pb collisions at 40A and 158AGeV," *Phys. Rev. C* **68** (Sep, 2003) 034903. https://link.aps.org/doi/10.1103/PhysRevC.68.034903.

[42] **STAR** Collaboration, L. Adamczyk *et al.*, "Beam-Energy Dependence of Directed Flow of Λ, $\bar{\Lambda}$, $K^{\pm}$, K^0_s and ϕ in Au+Au Collisions," *Phys. Rev. Lett.* **120** no. 6, (2018) 062301, arXiv:1708.07132 [hep-ex].

[43] **ALICE** Collaboration, K. Aamodt *et al.*, "Elliptic flow of charged particles in Pb-Pb collisions at 2.76 TeV," *Phys. Rev. Lett.* **105** (2010) 252302, arXiv:1011.3914 [nucl-ex].

[44] M. Luzum and P. Romatschke, "Viscous Hydrodynamic Predictions for Nuclear Collisions at the LHC," *Phys. Rev. Lett.* **103** (Dec, 2009) 262302. https://link.aps.org/doi/10.1103/PhysRevLett.103.262302.

[45] T. Hirano, P. Huovinen, and Y. Nara, "Elliptic flow in U+U collisions at $\sqrt{s_{NN}} = 200$ GeV and in Pb+Pb collisions at $\sqrt{s_{NN}} = 2.76$ TeV: Prediction from a hybrid approach," *Phys. Rev.* **C83** (2011) 021902, arXiv:1010.6222 [nucl-th].

[46] T. Hirano, U. W. Heinz, D. Kharzeev, R. Lacey, and Y. Nara, "Hadronic dissipative effects on elliptic flow in ultrarelativistic heavy-ion collisions," *Phys. Lett.* **B636** (2006) 299–304, arXiv:nucl-th/0511046 [nucl-th].

[47] H.-J. Drescher, A. Dumitru, and J.-Y. Ollitrault, "The Centrality dependence of elliptic flow at LHC," *J. Phys.* **G35** no. 5, (2008) 054001.50, arXiv:0706.1707 [nucl-th].

[48] **ALICE** Collaboration, J. Adam *et al.*, "Higher harmonic flow coefficients of identified hadrons in Pb-Pb collisions at $\sqrt{s_{\rm NN}}$ = 2.76 TeV," *JHEP* **09** (2016) 164, arXiv:1606.06057 [nucl-ex].

[49] **ALICE** Collaboration, J. Adam *et al.*, "Correlated event-by-event fluctuations of flow harmonics in Pb-Pb collisions at $\sqrt{s_{\rm NN}} = 2.76$ TeV," *Phys. Rev. Lett.* **117** (2016) 182301, arXiv:1604.07663 [nucl-ex].

[50] **ALICE** Collaboration, K. Aamodt *et al.*, "Suppression of Charged Particle Production at Large Transverse Momentum in Central Pb-Pb Collisions at $\sqrt{s_{NN}} = 2.76$ TeV," *Phys. Lett.* **B696** (2011) 30–39, arXiv:1012.1004 [nucl-ex].

[51] R. K. Ellis, W. J. Stirling, and B. R. Webber, *QCD and Collider Physics*. Cambridge Monographs on Particle Physics, Nuclear Physics and Cosmology. Cambridge University Press, 1996.

[52] J. C. Collins, D. E. Soper, and G. Sterman, "Factorization for short distance hadron-hadron scattering," *Nuclear Physics B* **261** (1985) 104 – 142. http://www.sciencedirect.com/science/article/pii/0550321385905656.

[53] **ZEUS, H1** Collaboration, F. D. Aaron *et al.*, "Combined Measurement and QCD Analysis of the Inclusive e+- p Scattering Cross Sections at HERA," *JHEP* **01** (2010) 109, arXiv:0911.0884 [hep-ex].

[54] N. Armesto, L. Cunqueiro, and C. A. Salgado, "Q-PYTHIA: A Medium-modified implementation of final state radiation," *Eur. Phys. J.* **C63** (2009) 679–690, arXiv:0907.1014 [hep-ph].

[55] Y. L. Dokshitzer, G. D. Leder, S. Moretti, and B. R. Webber, "Better jet clustering algorithms," *JHEP* **08** (1997) 001, arXiv:hep-ph/9707323 [hep-ph].

[56] S. Catani, Y. Dokshitzer, M. Seymour, and B. Webber, "Longitudinally-invariant $k_\perp$-clustering algorithms for hadron-hadron collisions," *Nuclear Physics B* **406** no. 1, (1993) 187 – 224. http://www.sciencedirect.com/science/article/pii/055032139390166M.

[57] M. Cacciari, G. P. Salam, and G. Soyez, "The Anti-k(t) jet clustering algorithm," *JHEP* **04** (2008) 063, arXiv:0802.1189 [hep-ph].

[58] J. Gallicchio and M. D. Schwartz, "Quark and Gluon Jet Substructure," *JHEP* **04** (2013) 090, arXiv:1211.7038 [hep-ph].

[59] T. Sjöstrand, "Monte Carlo Generators," in *High-energy physics. Proceedings, European School, Aronsborg, Sweden, June 18-July 1, 2006*, pp. 51–74. 2006. arXiv:hep-ph/0611247 [hep-ph]. http://weblib.cern.ch/abstract?CERN-LCGAPP-2006-06.

[60] M. H. Seymour and M. Marx, "Monte Carlo Event Generators," in *Proceedings, 69th Scottish Universities Summer School in Physics : LHC Phenomenology (SUSSP69): St.Andrews, Scotland, August 19-September 1, 2012*, pp. 287–319. 2013. arXiv:1304.6677 [hep-ph].

[61] A. Buckley *et al.*, "General-purpose event generators for LHC physics," *Phys. Rept.* **504** (2011) 145–233, arXiv:1101.2599 [hep-ph].

[62] T. Sjöstrand, S. Mrenna, and P. Z. Skands, "PYTHIA 6.4 Physics and Manual," *JHEP* **05** (2006) 026, arXiv:hep-ph/0603175 [hep-ph].

[63] T. Sjöstrand, "The Lund Monte Carlo for jet fragmentation," *Computer Physics Communications* **27** no. 3, (1982) 243 – 284. http://www.sciencedirect.com/science/article/pii/0010465582901758.

[64] T. Sjöstrand and P. Z. Skands, "Transverse-momentum-ordered showers and interleaved multiple interactions," *Eur. Phys. J.* **C39** (2005) 129–154, arXiv:hep-ph/0408302 [hep-ph].

[65] T. Sjöstrand, "A model for initial state parton showers," *Physics Letters B* **157** no. 4, (1985) 321 – 325. http://www.sciencedirect.com/science/article/pii/0370269385906744.

[66] V. N. Gribov and L. N. Lipatov, "Deep inelastic e p scattering in perturbation theory," *Sov. J. Nucl. Phys.* **15** (1972) 438–450. [Yad. Fiz.15,781(1972)].

[67] G. Altarelli and G. Parisi, "Asymptotic Freedom in Parton Language," *Nucl. Phys.* **B126** (1977) 298–318.

[68] Y. L. Dokshitzer, "Calculation of the Structure Functions for Deep Inelastic Scattering and e+ e- Annihilation by Perturbation Theory in Quantum Chromodynamics.," *Sov. Phys. JETP* **46** (1977) 641–653. [Zh. Eksp. Teor. Fiz.73,1216(1977)].

[69] Y. I. Azimov, Y. L. Dokshitzer, V. A. Khoze, and S. I. Trovan, "Similarity of parton and hadron spectra in QCD jets," *Zeitschrift für Physik C Particles and Fields* **27** no. 1, (Mar, 1985) 65–72. https://doi.org/10.1007/BF01642482.

[70] B. Andersson, G. Gustafson, G. Ingelman, and T. Sjöstrand, "Parton Fragmentation and String Dynamics," *Phys. Rept.* **97** (1983) 31–145.

[71] P. Z. Skands, "Tuning Monte Carlo Generators: The Perugia Tunes," *Phys. Rev.* **D82** (2010) 074018, arXiv:1005.3457 [hep-ph].

[72] X.-N. Wang and M. Gyulassy, "HIJING: A Monte Carlo model for multiple jet production in pp, pA, and AA collisions," *Phys. Rev. D* **44** (Dec, 1991) 3501–3516. https://link.aps.org/doi/10.1103/PhysRevD.44.3501.

[73] Z.-W. Lin, C. M. Ko, B.-A. Li, B. Zhang, and S. Pal, "A Multi-phase transport model for relativistic heavy ion collisions," *Phys. Rev.* **C72** (2005) 064901, arXiv:nucl-th/0411110 [nucl-th].

[74] J. Xu and C. M. Ko, "Pb-Pb collisions at $\sqrt{s_{NN}} = 2.76$ TeV in a multiphase transport model," *Phys. Rev.* **C83** (2011) 034904, arXiv:1101.2231 [nucl-th].

[75] B. Zhang, "ZPC 1.0.1: A Parton cascade for ultrarelativistic heavy ion collisions," *Comput. Phys. Commun.* **109** (1998) 193–206, arXiv:nucl-th/9709009 [nucl-th].

[76] B.-A. Li and C. M. Ko, "Formation of superdense hadronic matter in high-energy heavy ion collisions," *Phys. Rev.* **C52** (1995) 2037–2063, arXiv:nucl-th/9505016 [nucl-th].

[77] E. A. Mobs, "The CERN accelerator complex, OPEN-PHO-ACCEL-2016-013," 2016. http://cds.cern.ch/record/2225847.

[78] G. Fidecaro, *The Discoveries of Rare Pion Decays at the CERN Synchrocyclotron*, pp. 397–414. WORLD SCIENTIFIC, 2015.

[79] T. Massam, T. Muller, B. Righini, M. Schneegans, and A. Zichichi, "Experimental observation of antideuteron production," *Il Nuovo Cimento A* **63** no. 1, (Sep, 1965) 10–14. https://doi.org/10.1007/BF02898804.

[80] G. Charpak, R. Bouclier, T. Bressani, J. Favier, and C. Zupancic, "The use of multiwire proportional counters to select and localize charged particles," *Nuclear Instruments and Methods* **62** no. 3, (1968) 262 – 268. http://www.sciencedirect.com/science/article/pii/0029554X68903716.

[81] **UA1** Collaboration, G. Arnison *et al.*, "Experimental Observation of Lepton Pairs of Invariant Mass Around 95-GeV/c**2 at the CERN SPS Collider," *Phys. Lett.* **126B** (1983) 398–410.

[82] **UA2** Collaboration, P. Bagnaia *et al.*, "Evidence for Z0 –> e+ e- at the CERN anti-p p Collider," *Phys. Lett.* **129B** (1983) 130–140.

[83] **UA2** Collaboration, M. Banner *et al.*, "Observation of Single Isolated Electrons of High Transverse Momentum in Events with Missing Transverse Energy at the CERN anti-p p Collider," *Phys. Lett.* **122B** (1983) 476–485.

[84] **UA1** Collaboration, G. Arnison *et al.*, "Experimental Observation of Isolated Large Transverse Energy Electrons with Associated Missing Energy at s**(1/2) = 540-GeV," *Phys. Lett.* **122B** (1983) 103–116. [,611(1983)].

[85] V. Fanti *et al.*, "A new measurement of direct CP violation in two pion decays of the neutral kaon," *Physics Letters B* **465** no. 1, (1999) 335 – 348. http://www.sciencedirect.com/science/article/pii/S0370269399010308.

[86] G. Blanford, D. C. Christian, K. Gollwitzer, M. Mandelkern, C. T. Munger, J. Schultz, and G. Zioulas, "Observation of Atomic Antihydrogen," *Phys. Rev. Lett.* **80** (Apr, 1998) 3037–3040. https://link.aps.org/doi/10.1103/PhysRevLett.80.3037.

[87] **ALPHA** Collaboration, G. B. Andresen *et al.*, "Confinement of antihydrogen for 1000 seconds," *Nature Phys.* **7** (2011) 558–564, arXiv:1104.4982 [physics.atom-ph].

[88] S. Chatrchyan *et al.*, "Observation of a new boson at a mass of 125 GeV with the CMS experiment at the LHC," *Physics Letters B* **716** no. 1, (2012) 30 – 61. http://www.sciencedirect.com/science/article/pii/S0370269312008581.

[89] G. Aad *et al.*, "Observation of a new particle in the search for the Standard Model Higgs boson with the ATLAS detector at the LHC," *Physics Letters B* **716** no. 1, (2012) 1 – 29. http://www.sciencedirect.com/science/article/pii/S037026931200857X.

[90] **LHCb** Collaboration, R. Aaij *et al.*, "Observation of $J/\psi p$ Resonances Consistent with Pentaquark States in $\Lambda_b^0 \to J/\psi K^- p$ Decays," *Phys. Rev. Lett.* **115** (Aug, 2015) 072001. https://link.aps.org/doi/10.1103/PhysRevLett.115.072001.

[91] **AWAKE** Collaboration, R. Assmann *et al.*, "Proton-driven plasma wakefield acceleration: a path to the future of high-energy particle physics," *Plasma Phys. Control. Fusion* **56** no. 8, (2014) 084013, arXiv:1401.4823 [physics.acc-ph].

[92] L. Evans and P. Bryant, "LHC Machine," *JINST* **3** (2008) S08001.

[93] J. P. Blewett, "200-GeV Intersecting Storage Accelerators," *eConf* **C710920** (1971) 501.

[94] V. Duvivier, "Cross section of LHC dipole, LHC-PHO-2001-187," 2001. https://cds.cern.ch/record/843195.

[95] J.-L. Caron, "Computed magnetic flux in the LHC dipole, LHC-PHO-1998-320," 1998. http://cds.cern.ch/record/841503/files/.

[96] E. Todesco and J. Wenninger, "Large Hadron Collider momentum calibration and accuracy," *Phys. Rev. Accel. Beams* **20** no. 8, (2017) 081003.

[97] L. Arnaudon *et al.*, "Effects of terrestrial tides on the LEP beam energy," *Nucl. Instrum. Meth.* **A357** (1995) 249–252.

[98] **LHCf** Collaboration, O. Adriani *et al.*, "The LHCf detector at the CERN Large Hadron Collider," *JINST* **3** (2008) S08006.

[99] **TOTEM** Collaboration, G. Anelli *et al.*, "The TOTEM experiment at the CERN Large Hadron Collider," *JINST* **3** (2008) S08007.

[100] **MoEDAL** Collaboration, B. Acharya *et al.*, "Search for magnetic monopoles with the MoEDAL prototype trapping detector in 8 TeV proton-proton collisions at the LHC," *JHEP* **08** (2016) 067, arXiv:1604.06645 [hep-ex].

[101] **ATLAS** Collaboration, G. Aad *et al.*, "The ATLAS Experiment at the CERN Large Hadron Collider," *JINST* **3** (2008) S08003.

[102] **ALICE** Collaboration, K. Aamodt *et al.*, "The ALICE experiment at the CERN LHC," *JINST* **3** (2008) S08002.

[103] **CMS** Collaboration, S. Chatrchyan *et al.*, "The CMS Experiment at the CERN LHC," *JINST* **3** (2008) S08004.

[104] **LHCb** Collaboration, A. A. Alves, Jr. *et al.*, "The LHCb Detector at the LHC," *JINST* **3** (2008) S08005.

[105] T. Plehn, M. Spannowsky, M. Takeuchi, and D. Zerwas, "Stop Reconstruction with Tagged Tops," *JHEP* **10** (2010) 078, arXiv:1006.2833 [hep-ph].

[106] S. P. Martin, "A Supersymmetry primer," arXiv:hep-ph/9709356 [hep-ph]. [Adv. Ser. Direct. High Energy Phys.18,1(1998)].

[107] **ATLAS** Collaboration, G. Aad *et al.*, "Summary of the ATLAS experiment's sensitivity to supersymmetry after LHC Run 1 — interpreted in the phenomenological MSSM," *JHEP* **10** (2015) 134, arXiv:1508.06608 [hep-ex].

[108] **ATLAS** Collaboration, M. Aaboud *et al.*, "Search for electroweak production of supersymmetric states in scenarios with compressed mass spectra at $\sqrt{s} = 13$ TeV with the ATLAS detector," *Phys. Rev.* **D97** no. 5, (2018) 052010, arXiv:1712.08119 [hep-ex].

[109] **ATLAS** Collaboration, M. Aaboud *et al.*, "Search for chargino-neutralino production using recursive jigsaw reconstruction in final states with two or three charged leptons in proton-proton collisions at $\sqrt{s} = 13$ TeV with the ATLAS detector," arXiv:1806.02293 [hep-ex].

[110] **Pierre Auger** Collaboration, "The Pierre Auger Project Design Report,".

[111] H. Tokuno *et al.*, "New air fluorescence detectors employed in the Telescope Array experiment," *Nucl. Instrum. Meth.* **A676** (2012) 54–65, arXiv:1201.0002 [astro-ph.IM].

[112] **TOTEM** Collaboration, V. Berardi *et al.*, "TOTEM: Technical design report. Total cross section, elastic scattering and diffraction dissociation at the Large Hadron Collider at CERN,".

[113] A. Tauro, "ALICE Schematics, ALICE-PHO-SKE-2017-001," 2017. http://cds.cern.ch/record/2263642.

[114] **ALICE** Collaboration, N. Antoniou *et al.*, "Letter of Intent for A Large Ion Collider Experiment,".

[115] F. Follin and D. Jacquet, "Implementation and experience with luminosity levelling with offset beam," in *Proceedings, ICFA Mini-Workshop on Beam-Beam Effects in Hadron Colliders (BB2013): CERN, Geneva, Switzerland, March 18-22 2013*, pp. 183–187. 2014. arXiv:1410.3667 [physics.acc-ph].

[116] **ALICE** Collaboration, S. Beole *et al.*, "ALICE technical design report: Detector for high momentum PID,".

[117] **Particle Data Group** Collaboration, K. Nakamura *et al.*, "Review of particle physics," *J. Phys.* **G37** (2010) 075021.

[118] W. Blum, W. Riegler, and L. Rolandi, *Particle Detection with Drift Chambers*. Springer, 2008. https://www.springer.com/gp/book/9783540766834.

[119] **ALICE** Collaboration, M. Ivanov, "Identified charged hadron production measured with ALICE at the LHC," *Nucl. Phys.* **A904-905** (2013) 162c–169c.

[120] **ALICE** Collaboration, J. Allen *et al.*, "ALICE DCal: An Addendum to the EMCal Technical Design Report Di-Jet and Hadron-Jet correlation measurements in ALICE," Tech. Rep. CERN-LHCC-2010-011. ALICE-TDR-14-add-1, Jun, 2010. https://cds.cern.ch/record/1272952.

[121] A. Weber, Steffen Georg; Andronic, "ALICE event display of a Pb-Pb collision at 2.76A TeV, ALICE-PHO-GEN-2015-004," 2015. https://cds.cern.ch/record/2032743.

[122] **ALICE** Collaboration, B. Abelev *et al.*, "Upgrade of the ALICE Experiment: Letter Of Intent," *J. Phys.* **G41** (2014) 087001.

[123] I. Bejar Alonso and L. Rossi, "HiLumi LHC Technical Design Report: Deliverable: D1.10," Tech. Rep. CERN-ACC-2015-0140, Nov, 2015. http://cds.cern.ch/record/2069130.

[124] **ALICE** Collaboration, C. Lippmann, "Upgrade of the ALICE Time Projection Chamber,".

[125] **ALICE** Collaboration, J. Adam *et al.*, "Addendum to the Technical Design Report for the Upgrade of the ALICE Time Projection Chamber,".

[126] A. Maire, "ALICE TPC sectors and pad rows, ALICE-PHO-SKE-2011-007," 2011. https://cds.cern.ch/record/2030274.

[127] **ALICE** Collaboration, K. Aadmodt *et al.*, "Alignment of the ALICE Inner Tracking System with cosmic-ray tracks," *Journal of Instrumentation* **5** no. 03, (2010) P03003. http://stacks.iop.org/1748-0221/5/i=03/a=P03003.

[128] J. Alme *et al.*, "The ALICE TPC, a large 3-dimensional tracking device with fast readout for ultra-high multiplicity events," *Nucl. Instrum. Meth.* **A622** (2010) 316–367, `arXiv:1001.1950 [physics.ins-det]`.

[129] F. Sauli, "GEM: A new concept for electron amplification in gas detectors," *Nuclear Instruments and Methods in Physics Research Section A: Accelerators, Spectrometers, Detectors and Associated Equipment* **386** no. 2, (1997) 531 – 534. http://www.sciencedirect.com/science/article/pii/S0168900296011722.

[130] F. Sauli, "The gas electron multiplier (GEM): Operating principles and applications," *Nuclear Instruments and Methods in Physics Research Section A: Accelerators, Spectrometers, Detectors and Associated Equipment* **805** (2016) 2 – 24.
http://www.sciencedirect.com/science/article/pii/S0168900215008980.
Special Issue in memory of Glenn F. Knoll.

[131] A. Colaleo, A. Safonov, A. Sharma, and M. Tytgat, "CMS Technical Design Report for the Muon Endcap GEM Upgrade," Tech. Rep. CERN-LHCC-2015-012. CMS-TDR-013, Jun, 2015. https://cds.cern.ch/record/2021453.

[132] F. Sauli, L. Ropelewski, and P. Everaerts, "Ion feedback suppression in time projection chambers," *Nucl. Instrum. Meth.* **A560** (2006) 269–277.

[133] M. Ball, K. Eckstein, and T. Gunji, "Ion backflow studies for the ALICE TPC upgrade with GEMs," *Journal of Instrumentation* **9** no. 04, (2014) C04025. http://stacks.iop.org/1748-0221/9/i=04/a=C04025.

[134] S. Bachmann, A. Bressan, M. Capeáns, M. Deutel, S. Kappler, B. Ketzer, A. Polouektov, L. Ropelewski, F. Sauli, E. Schulte, L. Shekhtman, and A. Sokolov, "Discharge studies and prevention in the gas electron multiplier (GEM)," *Nuclear Instruments and Methods in Physics Research Section A: Accelerators, Spectrometers, Detectors and Associated Equipment* **479** no. 2, (2002) 294 – 308.
http://www.sciencedirect.com/science/article/pii/S0168900201009317.

[135] A. Utrobicic, M. Kovacic, F. Erhardt, N. Poljak, and M. Planinic, "A floating multi-channel picoammeter for micropattern gaseous detector current monitoring," *Nuclear Instruments and Methods in Physics Research Section A: Accelerators, Spectrometers, Detectors and Associated Equipment* **801** (2015) 21 – 26.
http://www.sciencedirect.com/science/article/pii/S0168900215009559.

[136] T. Hildén, E. Brücken, J. Heino, M. Kalliokoski, A. Karadzhinova, R. Lauhakangas, E. Tuominen, and R. Turpeinen, "Optical quality assurance of GEM foils," *Nucl. Instrum. Meth.* **A770** (2015) 113–122, arXiv:1704.06691 [physics.ins-det].

[137] M. Kalliokoski, T. Hilden, F. Garcia, J. Heino, R. Lauhakangas, E. Tuominen, and R. Turpeinen, "Optical scanning system for quality control of GEM-foils," *Nuclear Instruments and Methods in Physics Research Section A: Accelerators, Spectrometers, Detectors and Associated Equipment* **664** no. 1, (2012) 223 – 230. http://www.sciencedirect.com/science/article/pii/S0168900211020109.

[138] M. Kalliokoski, T. Hilden, F. Garcia, J. Heino, R. Lauhakangas, E. Tuominen, and R. Turpeinen, "Analyzing GEM-foil properties with an optical scanning system," *Journal of Instrumentation* **7** no. 02, (2012) C02059. http://stacks.iop.org/1748-0221/7/i=02/a=C02059.

[139] **CERN RD-51** Collaboration, P. M. M. Correia, C. A. B. Oliveira, C. D. R. Azevedo, A. L. M. Silva, R. Veenhof, M. Varun Nemallapudi, and J. F. C. A. Veloso, "A dynamic method for charging-up calculations: the case of GEM," *JINST* **9** (2014) P07025, arXiv:1401.4009 [physics.ins-det].

[140] **ALICE** Collaboration, S. Das, "Study of gain variation as a function of physical parameters of GEM foil," *Nucl. Instrum. Meth.* **A824** (2016) 518–520, arXiv:1506.06520 [physics.ins-det].

[141] H. A. Andrews *et al.*, "Novel tools and observables for jet physics in heavy-ion collisions," arXiv:1808.03689 [hep-ph].

[142] **CMS** Collaboration, S. Chatrchyan *et al.*, "Measurement of jet fragmentation in PbPb and pp collisions at $\sqrt{s_{NN}} = 2.76$ TeV," *Phys. Rev.* **C90** no. 2, (2014) 024908, arXiv:1406.0932 [nucl-ex].

[143] W.-t. Deng and X.-N. Wang, "Multiple Parton Scattering in Nuclei: Modified DGLAP Evolution for Fragmentation Functions," *Phys. Rev.* **C81** (2010) 024902, arXiv:0910.3403 [hep-ph].

[144] T. Renk, "A Comparison study of medium-modified QCD shower evolution scenarios," *Phys. Rev.* **C79** (2009) 054906, arXiv:0901.2818 [hep-ph].

[145] T. Renk, "Parton shower evolution in a 3-d hydrodynamical medium," *Phys. Rev.* **C78** (2008) 034908, arXiv:0806.0305 [hep-ph].

[146] X.-N. Wang and X.-f. Guo, "Multiple parton scattering in nuclei: Parton energy loss," *Nucl. Phys.* **A696** (2001) 788–832, arXiv:hep-ph/0102230 [hep-ph].

[147] **ALICE** Collaboration, B. Abelev *et al.*, "Measurement of the inclusive differential jet cross section in pp collisions at $\sqrt{s} = 2.76$ TeV," *Phys. Lett.* **B722** (2013) 262–272, arXiv:1301.3475 [nucl-ex].

[148] **CMS** Collaboration, S. Chatrchyan *et al.*, "Measurement of the ratio of inclusive jet cross sections using the anti-k_T algorithm with radius parameters R=0.5 and 0.7 in pp collisions at $\sqrt{s} = 7$TeV," *Phys. Rev.* **D90** no. 7, (2014) 072006, arXiv:1406.0324 [hep-ex].

[149] M. Dasgupta, F. A. Dreyer, G. P. Salam, and G. Soyez, "Inclusive jet spectrum for small-radius jets," *JHEP* **06** (2016) 057, arXiv:1602.01110 [hep-ph].

[150] **ATLAS** Collaboration, G. Aad *et al.*, "Measurement of the jet radius and transverse momentum dependence of inclusive jet suppression in lead-lead collisions at $\sqrt{s_{NN}}$= 2.76 TeV with the ATLAS detector," *Phys. Lett.* **B719** (2013) 220–241, arXiv:1208.1967 [hep-ex].

[151] **ALICE** Collaboration, B. Abelev *et al.*, "Measurement of charged jet suppression in Pb-Pb collisions at $\sqrt{s_{NN}}$ = 2.76 TeV," *JHEP* **03** (2014) 013, arXiv:1311.0633 [nucl-ex]. Journal club discussion.

[152] **ALICE** Collaboration, J. Adam *et al.*, "Measurement of jet quenching with semi-inclusive hadron-jet distributions in central Pb-Pb collisions at $\sqrt{s_{\mathrm{NN}}} = 2.76$ TeV," *JHEP* **09** (2015) 170, arXiv:1506.03984 [nucl-ex].

[153] **ATLAS** Collaboration, M. Aaboud *et al.*, "Measurement of jet fragmentation in Pb+Pb and pp collisions at $\sqrt{s_{\mathrm{NN}}} = 2.76$ TeV with the ATLAS detector at the LHC," *Eur. Phys. J.* **C77** no. 6, (2017) 379, arXiv:1702.00674 [hep-ex].

[154] M. Gyulassy and M. Plumer, "Jet Quenching in Dense Matter," *Phys. Lett.* **B243** (1990) 432–438.

[155] **CMS** Collaboration, S. Chatrchyan *et al.*, "Observation and studies of jet quenching in PbPb collisions at nucleon-nucleon center-of-mass energy = 2.76 TeV," *Phys. Rev.* **C84** (2011) 024906, arXiv:1102.1957 [nucl-ex].

[156] J. Casalderrey-Solana, Y. Mehtar-Tani, C. A. Salgado, and K. Tywoniuk, "New picture of jet quenching dictated by color coherence," *Phys. Lett.* **B725** (2013) 357–360, arXiv:1210.7765 [hep-ph].

[157] **ALICE** Collaboration, S. Acharya *et al.*, "Medium modification of the shape of small-radius jets in central Pb-Pb collisions at $\sqrt{s_{\mathrm{NN}}} = 2.76$ TeV," *Submitted to: JHEP* (2018) , arXiv:1807.06854 [nucl-ex].

[158] **STAR** Collaboration, G. Agakishiev *et al.*, "System size and energy dependence of near-side di-hadron correlations," *Phys. Rev.* **C85** (2012) 014903, arXiv:1110.5800 [nucl-ex].

[159] **ALICE** Collaboration, J. Adam *et al.*, "Anomalous evolution of the near-side jet peak shape in Pb-Pb collisions at $\sqrt{s_{\mathrm{NN}}}$ = 2.76 TeV," *Phys. Rev. Lett.* **119** no. 10, (2017) 102301, arXiv:1609.06643 [nucl-ex].

[160] **ALICE** Collaboration, J. Adam *et al.*, "Jet-like correlations with neutral pion triggers in pp and central Pb–Pb collisions at 2.76 TeV," *Phys. Lett.* **B763** (2016) 238–250, arXiv:1608.07201 [nucl-ex].

[161] **CMS** Collaboration, V. Khachatryan *et al.*, "Decomposing transverse momentum balance contributions for quenched jets in PbPb collisions at $\sqrt{s_{\mathrm{N\,N}}} = 2.76$ TeV," *JHEP* **11** (2016) 055, arXiv:1609.02466 [nucl-ex].

[162] **ALICE** Collaboration, B. Abelev *et al.*, "Centrality Dependence of Charged Particle Production at Large Transverse Momentum in Pb–Pb Collisions at $\sqrt{s_{\mathrm{NN}}} = 2.76$ TeV," *Phys. Lett.* **B720** (2013) 52–62, arXiv:1208.2711 [hep-ex].

[163] **ALICE** Collaboration, E. Abbas *et al.*, "Performance of the ALICE VZERO system," *JINST* **8** (2013) P10016, arXiv:1306.3130 [nucl-ex].

[164] A. Maire, *Production des baryons multi-étranges au LHC dans les collisions proton-proton avec l'expérience ALICE*. PhD thesis, Strasbourg, IPHC, 2011. http://inspirehep.net/record/1231256/files/CERN-THESIS-2011-263.pdf.

[165] A. Maire, "Track reconstruction principle in ALICE for LHC run I and run II, ALICE-PHO-SKE-2011-001," 2011. https://cds.cern.ch/record/1984041.

[166] **ALICE** Collaboration, K. Aamodt *et al.*, "Particle-yield modification in jet-like azimuthal di-hadron correlations in Pb-Pb collisions at $\sqrt{s_{NN}} = 2.76$ TeV," *Phys. Rev. Lett.* **108** (2012) 092301, arXiv:1110.0121 [nucl-ex].

[167] **STAR** Collaboration, L. Adamczyk *et al.*, "Di-hadron correlations with identified leading hadrons in 200 GeV Au + Au and d + Au collisions at STAR," *Phys. Lett.* **B751** (2015) 233–240, arXiv:1410.3524 [nucl-ex].

[168] **ALICE** Collaboration, F. Krizek, "Analysis of near side $I_{\mathrm{AA}}(\Delta\eta)$ from Pb-Pb collisions at $\sqrt{s_{\mathrm{NN}}}$= 2.76 TeV and pp collisions at $\sqrt{s}$ = 2.76 TeV," https://aliceinfo.cern.ch/Notes/node/65.

[169] S. Ravan, P. Pujahari, S. Prasad, and C. A. Pruneau, "Correcting correlation function measurements," *Phys. Rev. C* **89** (Feb, 2014) 024906. https://link.aps.org/doi/10.1103/PhysRevC.89.024906.

[170] S. Agostinelli *et al.*, "Geant4 — a simulation toolkit," *Nuclear Instruments and Methods in Physics Research Section A: Accelerators, Spectrometers, Detectors and Associated Equipment* **506** no. 3, (2003) 250 – 303. http://www.sciencedirect.com/science/article/pii/S0168900203013688.

[171] J. Allison *et al.*, "Geant4 developments and applications," *IEEE Transactions on Nuclear Science* **53** no. 1, (Feb, 2006) 270–278.

[172] J. Allison *et al.*, "Recent developments in Geant4," *Nuclear Instruments and Methods in Physics Research Section A: Accelerators, Spectrometers, Detectors and Associated Equipment* **835** (2016) 186 – 225. http://www.sciencedirect.com/science/article/pii/S0168900216306957.

[173] R. Barlow, "Systematic errors: Facts and fictions," in *Advanced Statistical Techniques in Particle Physics. Proceedings, Conference, Durham, UK, March 18-22, 2002*, pp. 134–144. 2002. arXiv:hep-ex/0207026 [hep-ex]. http://www.ippp.dur.ac.uk/Workshops/02/statistics/proceedings/ /barlow.pdf.

[174] T. Sjöstrand, S. Mrenna, and P. Z. Skands, "A Brief Introduction to PYTHIA 8.1," *Comput. Phys. Commun.* **178** (2008) 852–867, arXiv:0710.3820 [hep-ph].

[175] Z.-w. Lin and C. M. Ko, "Partonic effects on the elliptic flow at RHIC," *Phys. Rev.* **C65** (2002) 034904, arXiv:nucl-th/0108039 [nucl-th].

[176] M. Spousta and B. Cole, "Interpreting single jet measurements in Pb + Pb collisions at the LHC," *Eur. Phys. J.* **C76** no. 2, (2016) 50, arXiv:1504.05169 [hep-ph].

[177] H. J. Kim, "Private communication.".

[178] V. Duvivier, "CERN Accelerator Complex (operating and approved projets), LHC-PHO-2001-190.," 2001. https://cds.cern.ch/record/843346.

APPENDIX 1 CERN ACCELERATOR COMPLEX TO SCALE

In Figure 8 the CERN accelerator complex was not to scale, and it is interesting to see the proportions. In Figure 56 one can see how the LHC dwarfs all other accelerator rings (PS and SPS) dominating the view with its 27 km circumference ring.

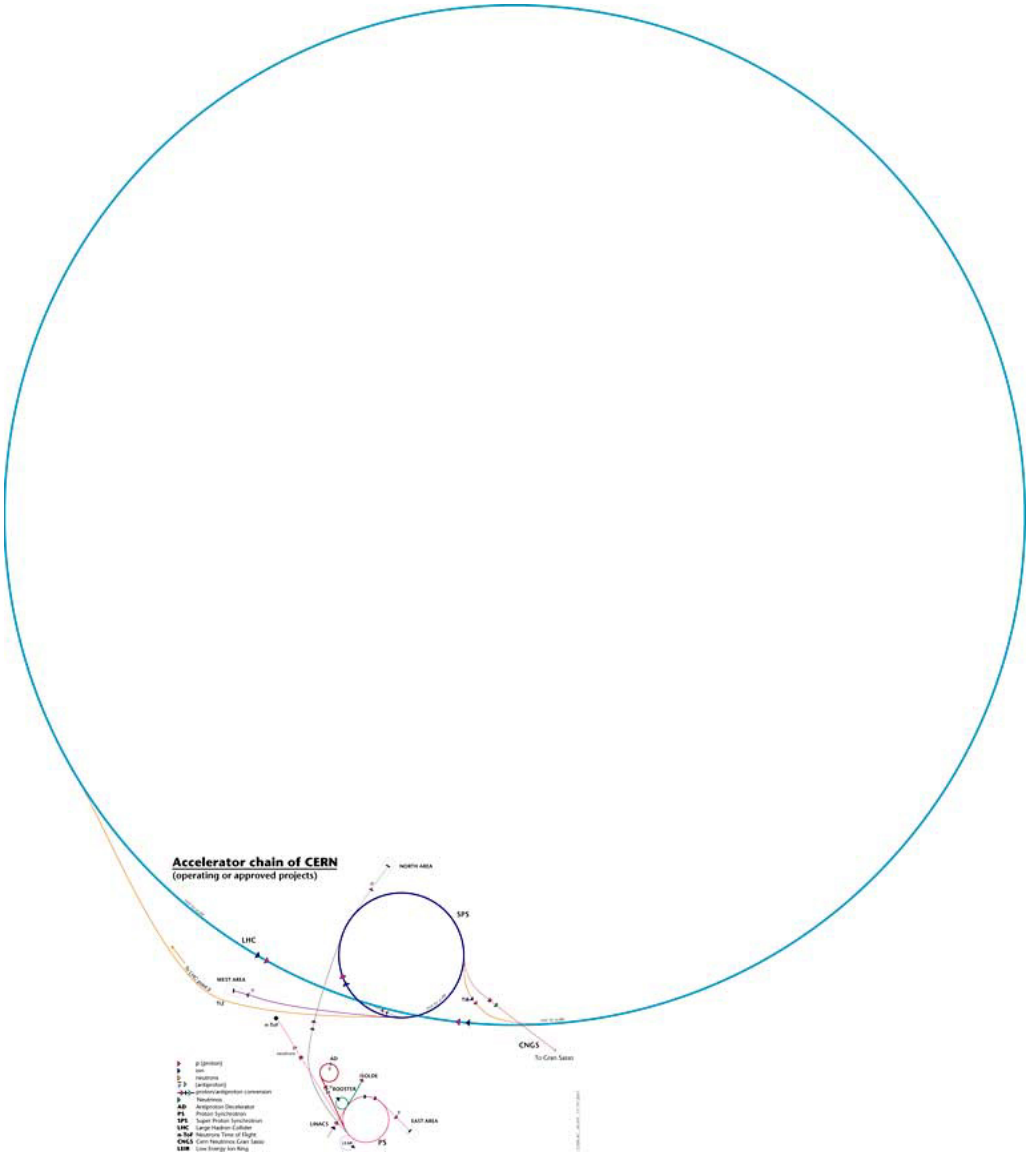

FIGURE 56 The true scale cartoon of the CERN accelerator complex. LHC dominates the view with its 27 km circumference [178].